TECHNISCHE UNIVERSITÄT WIEN

Diplomarbeit

Advanced Characterization of Bitumen using Chromatography and FTIR Spectroscopy

Ausgeführt am

Institut für Materialchemie

der Technischen Universität Wien

unter der Anleitung von

Univ.Prof. Dipl.-Chem. Dr.rer.nat. Hinrich Grothe und

Dipl. Ing. Johannes Mirwald

durch

Stefan Werkovits

Mat.Nr.: 01425933

Wien, am

Datum

Unterschrift

Affidavit

I declare that I have authored this thesis independently, that I have not used other than the declared sources/resources, and that I have explicitly indicated all material which has been quoted either literally or by content from the sources used. The text document uploaded to TU Wien University Library (https://www.ub.tuwien.ac.at/eng/) is identical to the present master's thesis.

Date	Signature

Acknowledgements

First of all I would like to express my gratitude to my supervisor Hinrich Grothe for giving me the opportunity to conduct my diploma thesis under his supervision. Additionally I would like to thank Solutions 4 Science for providing the Perkin Elmer Spectrum Two and for the financial support that made this work possible.

Furthermore, I want to thank Johannes Mirwald for awakening my interest on bitumen research and for his advices in the laboratory, during preparations for talks and for the hours of discussion on FTIR spectra interpretation. Also many thanks to Ingrid Camargo, who organized the required materials and started the implementation for Fast SARA analysis in our laboratories. Another big thank you to Thomas Riedmayer, who conducted the DSR experiments for this thesis.

I also want to thank the rest of the working group, who provided such an entertaining and interesting time during my 6 months of working besides them.

Last but not least I want to thank my family, friends and my girlfriend for supporting me in any possible way and always being there for me.

Abstract

Bitumen is a product derived from the crude oil refinement process. It is commonly used as a binder material in asphalt pavement or as a sealing and waterproofing material in roofing. Due to different origins of the crude oil source, the characteristics of bitumen with the same mechanical classification can vary in terms of chemical composition, long-term performance and ageing susceptibility. The goal of this thesis was a thorough physical-chemical investigation of three different bitumen binders with the same mechanical classification by combining chromatographic separation and spectroscopic analysis. Each of those binders was investigated at various ageing states. Furthermore, a set of selected samples were studied using different preparation and storage parameters. This involved a comprehensive time dependent study of bitumen at room temperature and varying exposure to light. These bitumen samples were than measured with the two analytical tools used in this work: Fourier Transform Infrared (FTIR) spectroscopy and Dynamic Shear Rheometry (DSR). As a result, one can claim that storage conditions have great influence on resulting infrared spectra as the samples stored in light show significant changes compared to the samples stored in the dark.

The main task of this thesis involved the combination of a novel separation technique, namely the Fast SARA technique [1], and FTIR spectroscopy. While the Fast SARA chromatography separates bitumen into four different polarity-based fractions; the saturates, aromatics, resins and asphaltenes, FTIR spectroscopy captures the characteristic vibrations of different functional groups present in bitumen. By separating binders of different ageing states and subsequent measurement with FTIR spectroscopy, one can obtain valuable information on the ageing processes that occur during the different ageing procedures, such as oxidation processes, polarity shifts etc. The main findings obtained for all binders in the gravimetric analysis show a general increase in polarity towards the more polar fractions. This results in a polarity decrease in the aromatic fraction and an increase in the more polar fractions, the resins and asphaltenes. By comparing the FTIR spectra of the fractions in its different ageing states, an overall extension of information depth can be obtained by separating them via chromatography. This is observable by various new IR bands that are found in the fractions that generally cannot be deconvoluted in the base binder spectra. Especially the monitoring of ageing with FTIR spectroscopy in the generic fractions are of great interest to help to fully understand and track the ageing processes in bitumen. Therefore, they are going to be discussed thoroughly, which finally leads to band assignments in the fractions considering all the knowledge and information gained in the various experiments implemented in this work.

Kurzfassung

Bitumen ist ein wichtiges industrielles Produkt, das bei der Erdölaufarbeitung gewonnen wird. Hauptanwendungsgebiete sind der Einsatz als Bindemittel im Straßenbau aber auch als abdichtendes und wasserabweisendes Material beim Dach- und Dichtungsbahnbau. Wegen der unterschiedlichen Herkunft des Rohöls können Bitumensorten, die mechanisch gleichklassifiziert werden, im chemischen Aufbau, der Langzeitperformance und in der Alterungsanfälligkeit stark voneinander abweichen. Ziel dieser Arbeit ist es, die physikalisch-chemischen Unterschiede von 3 mechanisch gleichklassifizierten Bitumensorten durch die Kombination von chromatographischen und spektroskopischen Methoden zu untersuchen. Dazu wurde jede Bitumensorte bei unterschiedlichen Alterungszuständen untersucht. Ein weiterer Schwerpunkt dieser Arbeit war die Untersuchung der Auswirkung von Präparation und Lagerung auf die Messergebnisse. Das involvierte die Studie an Bitumen, welches bei Raumtemperatur und bei unterschiedlichen Lichteinflüssen gelagert wurde. Um die Zeitabhängigkeit der Veränderung an der Oberfläche aber auch im Bulkmaterial analytisch zu verfolgen wurde Fourier-Transformation Infrarotspektroskopie (FTIR) und ein Dynamisches Scherrheometer (DSR) eingesetzt. Ein wichtiges Ergebnis dieser Studien ist der große Einfluss der gewählten Lichtbedingungen auf die Infrarotspektren, welcher in den DSR-Daten wesentlich kleiner ausfiel.

Der Hauptteil dieser Arbeit war die Kombination einer neuartigen Trenntechnik, die als Fast SARA [1] bezeichnet wird, und FTIR-Spektroskopie. Dabei ist es mit Fast SARA möglich Bitumen in einzelne Fraktionen mit unterschiedlichen Polaritäten aufzutrennen. Diese werden als Saturates, Aromatics, Resine und Asphaltene bezeichnet. Die anschließende spektroskopische Untersuchung mit FTIR bringt dann charakteristische Schwingungen von unterschiedlichsten funktionellen Gruppen, die in den einzelnen Fraktionen vorhanden sind, zum Vorschein. Somit kann durch die Auftrennung von unterschiedlich gealterten Bitumensorten und der anschließenden spektroskopischen Untersuchung wertvolle Information, wie z.B. Alterungsprozesse, Oxidationsverläufe und Änderungen der Mengenanteil der einzelnen Fraktionen erhalten und analysiert werden. Ein wichtiges Ergebnis der gravimetrischen Untersuchungen war ein genereller Anstieg der Polarität mit der Alterung der in allen untersuchten Bitumensorten bestimmt werden konnte. Dabei nahm der Gehalt an Aromatics und Saturates ab, wohingegen der Resin- und Asphaltengehalt mit der Alterung zunahm. Beim Vergleich der resultierenden FTIR-Spektren der unterschiedlich gealterten Fraktionen kann Informationstiefe gewonnen werden, durch die Separation mittels Chromatographie. Dies ist an neuen Banden in den FTIR-Spektren der Fraktionen zu erkennen, die in den Bitumenspektren durch die Überlappungen mehrerer Banden nicht einzeln auftreten. Besonders der spektroskopisch verfolgte Alterungsprozess der SARA Fraktionen kann somit das Verständnis der Bitumenalterung erweitern. Mögliche Alterungsprozesse werden daher gründlich untersucht und unter Einbezug aller experimentellen Befunde und geeigneter literarischer Quellen Bandenzuordnungen und somit die Bestimmung vorhandener funktioneller Gruppen im Bitumen durchgeführt.

Table of Contents

1. Research Objective

1.1. Introduction

Bitumen is a highly viscous black liquid that is derived mostly as a product of the crude oil refining process. This process is carried out in distillation plants where crude oil is separated into various fuels such as kerosene, diesel, gasoline, heating oil, industrial gases and the residue of the vacuum distillation: bitumen. Figure 1 depicts such a distillation plant where the common steps are highlighted thoroughly.

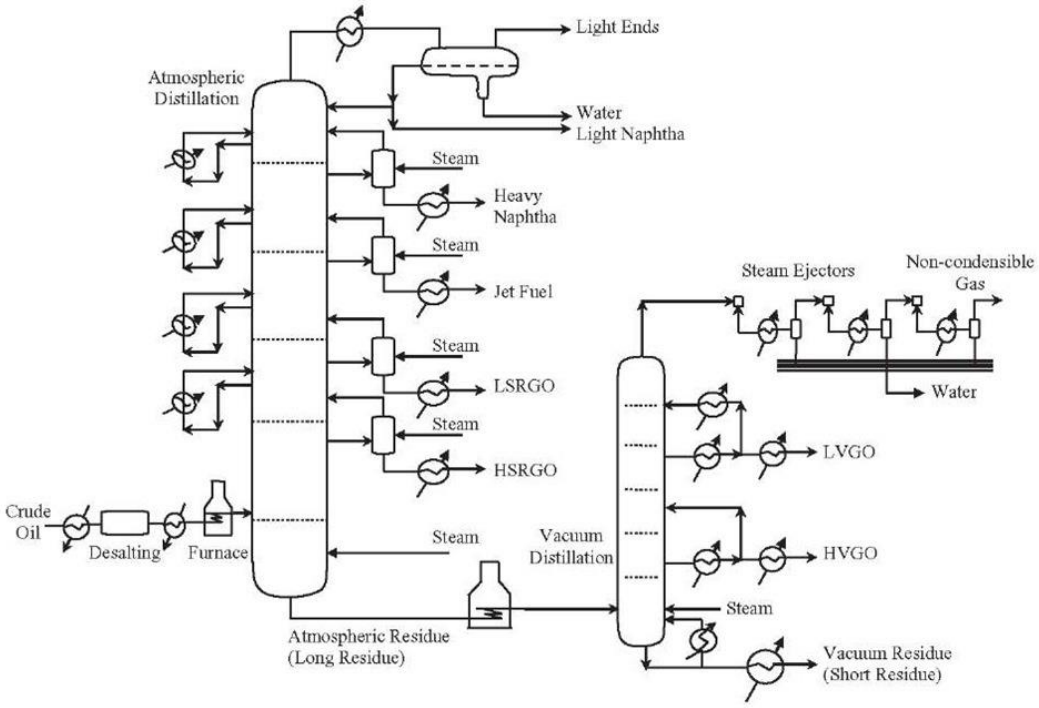

Figure 1: Scheme of a crude oil distillation plant [2]

Its main industrial applications are road pavements and rooftops, with the road sector covering up to 80 % of the bitumen market. [3] In asphalt, bitumen is mixed with aggregates like sand, gravel and stones. The bitumen content ranges from 5-8 %, depending on the mix design and purpose of the resulting asphalt. [3] A first distinction for asphalt is generally made between roller-compacted and mastic asphalt. Roller-compacted asphalt reaches its necessary grade of compaction only after the usage of road rollers whereas mastic asphalt can be processed in its molten form and do not need further compaction.

Another important parameter to differentiate asphalt is the mixing temperature during the production process and the commonly used terms are hot-mix asphalt (HMA) and warm-mix asphalt (WMA). During the hot-mixing process bitumen is heated up at first. This is mainly done to decrease the viscosity and to remove any moisture inherent in most of the common bitumina in use. After that, the mixing process with the chosen aggregates takes place at roughly 160 °C, depending on the desired asphalt (e.g. virgin-, polymer-modified-bitumen). The next two important steps, paving and compaction, have to be implemented while the asphalt is still hot (>100 °C [4]). In contrast to HMA, WMA is produced while using significantly lower mixing temperatures (depending on the specific WMA technology[1]). This is achievable by adding waxes, zeolites or asphalt emulsions to the bitumen

[1] According to [5] a temperature reduction (compared to HMA) of at least 12,2°C in 50.5 % of all produced WMA

to lower its overall viscosity. With that, lower mixing and paving temperatures are needed, which leads as a consequence to lower carbon dioxide and aerosol exhaust during the production. The market for WMA grows rapidly as a survey of asphalt producers in the US outlines. 38.9% of the total asphalt market was made up by WMA in 2017. [5]

The shortly mentioned branch of polymer-modified bitumen (PmB) is going to be topic of this paragraph. The reason for modification of bitumen is its susceptibility to changes in harsh environments, which includes very high or low temperatures as well as high traffic volume. Neither very hot places, where bitumen softens readily and is more susceptible to ageing, nor cold environments, which can lead to embrittlement, are preferable places for the usage of unmodified bitumen. To toughen bitumen in such environments a common method is to blend it with polymers, such as the block copolymer SBS (styrene butadiene styrene). The main objective of such modifications remains to provide a longer service-life to roads and pavements in use by improving the resistance to thermal cracking and decreasing important performance parameters such as fatigue damages, stripping and temperature susceptibility. [6, 7]

Finally, a topic of great concern in all important industries is recycling. There are major changes in bitumen structure and chemistry that are happening during its service life. These changes lead mainly to a deterioration of mechanical properties which will be discussed thoroughly in the theory chapter of this work. With that said, reuse and recycle of already used bitumen/asphalt is most properly connected to a worse quality of the obtained building material. To understand this, one has to look at the common processes of bitumen/asphalt recycling. Asphalt recycling can be categorized into two major categories: in-place and in-plant recycling. The differentiation that is drawn is by considering the place where the material is reconditioned. On the one hand, in-place recycling is done directly on the spot where a wide variety of different hot-temperature recycling processes, such as reshaping, repaving or remixing can be used. The asphalt is heated up at first, tore up, spread, then new material might be added and finally the whole place is consolidated. On the other hand, during the recycling in plant the obtained recycling asphalt, which is already crushed into small pieces, is either mixed with new bitumen or with so-called rejuvenators. The mixing with additives is necessary to obtain mechanical stability and durability comparable to new bitumen. An advantage of this recycle process is that less fresh bitumen is needed compared to building completely new roads, but in contrast the ageing susceptibility can never be as good as for entirely new bitumen, since a rather high rate of the whole material is already chemically aged, which cannot be turned back. [5, 8]

In conclusion, different production ways of bitumen result into different asphalt materials which have been developed for different purposes in road works, building and construction. It is described that especially the binder material (bitumen) of the complex asphalt mixture is prone to chemical aging and mechanical deterioration with time. To monitor such changes in the materials in use non-destructive spectroscopic techniques are preferable. The interaction with reactive oxygen species and light, the relation between mechanical and chemical changes, and the region where the binder alteration appears are the main topics of this thesis, which will be outlined in greater detail in chapter 1.2.

1.2. Statement of the Problem and Need for Study

As mentioned above, a general problem of bitumen is its alteration with time. Figure 2 shows an outcome of bitumen/asphalt used for a long period of time.

Figure 2: Possible cracks in asphalt during its service life on the roads [9]

The main reasons for such cracks are chemo-mechanical changes in the binder material. Hence, an exact description of the ageing processes based on chemical modifications in the material as well as a connection to the appearing mechanical changes is a topic of great concern. Furthermore, profound gain of knowledge in these segments can lead to possible predictions of material failure of products in use. Besides, a differentiation of binders from various sources or produced via different production processes in regard of their quality and/or susceptibility to ageing can be made. To achieve such goals (e.g. profound understanding of crack formation) the problem is often reduced to its parts. This means, that throughout the investigations in this thesis the binder component of asphalt, bitumen, was the main research object. To simplify the still complex bitumen matrix even further it was separated into four different fractions using the different polarity properties of molecules within the binder.

Thus, the main goal of this work was to investigate the ageing behavior of bitumen and its polarity fractions. Therefore, common laboratory ageing methods (RTFOT, PAV) [10, 11], a novel laboratory ageing method (Viennese Binder Ageing: VBA) [12] as well as field ageing and light induced short term ageing were applied on samples from three different sources. The bitumen samples were analyzed by using a polarity-based separation method and FTIR spectroscopy to observe changes of chemical compounds in the binder as well as in the obtained polarity fractions. The other important research tasks of this work were time-dependency studies at ambient conditions, where short term changes in chemical composition and mechanical behavior were monitored using FTIR and DSR. Further information on the theoretical concepts of the ageing procedures, separation techniques, infrared spectroscopy and DSR are presented in chapter 2, whereas the experimental implementations and realizations of these concepts are given in chapter 3.

2. Theoretical Paradigm

The theoretical part is going to cover bitumen structure, inherent components as well as common and novel separation methods. The ageing processes and commonly used ageing simulation methods are going to be the follow up. Finally, the analytical approach is the last point in this chapter, where theoretical principles of chromatographic separation, herein called Fast SARA[2] and FTIR as well as their instrumentation principles are topics that will be outlined.

2.1. Bitumen Structure

The formation of an enormous amount of different molecular structures in crude oil over a time period of millions of years can be traced back to natural and biological origins. Hence, the variety of elements that are appearing in crude oil/bitumen are similar to their origins and can be summarized by a list of the following elements abundant in every biological species: C, H, N, O, S. However, with time and environmental influence the composition of these elements changes in bitumen due to processes such as: loss (evaporation/formation) of volatile compounds, precipitation of compounds, salt formation and many more. Especially evaporation of water leads to decreasing hydrogen contents in bitumen.

The elemental analysis of bitumen shows that carbons are the most abundant elements (typically from 80 to 88 wt. %) followed by hydrogen with a mass content of 8-12 wt. %. Besides those elements, hetero atoms such as sulfur (0-9 wt. %), nitrogen (0-2 wt. %) and oxygen (0-2 wt. %) but also traces of metals like nickel, vanadium and manganese can be found in bitumen. [6] These elements are bonded together by means of covalent bonds to create a variety of different molecular species, ranging from low polar linear alkanes to highly polar porphyrins and heteroaromatic structures. However, most of them can be classified as hydrocarbons (>90 wt. %). [6] The most abundant functional groups in unaged and aged bitumen are presented in Figure 3.

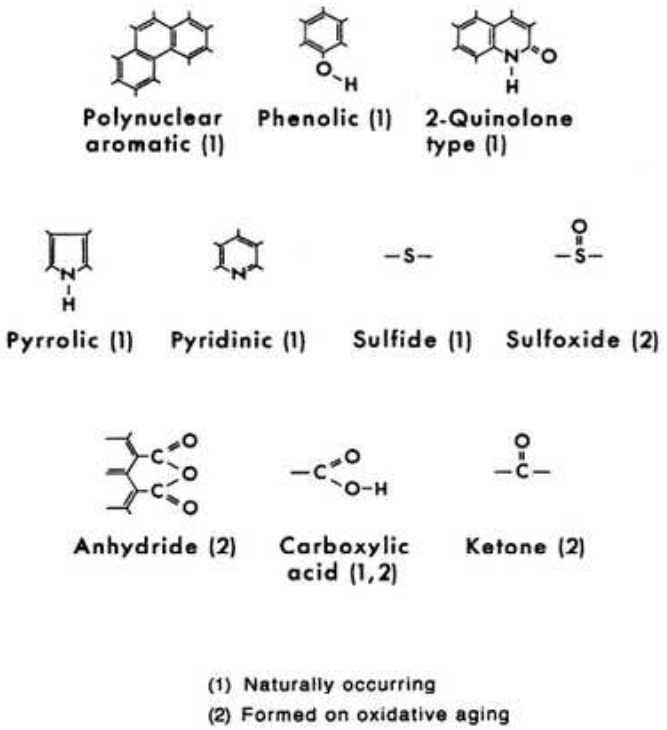

Figure 3: Common functionalities in unaged and aged bitumen samples [13]

[2] SARA = Saturates, Aromatics, Resins, Asphaltenes. Detailed description in subchapter 2.1.1

Figure 3 shows the presence of various aromatic and polyaromatic compounds in bitumen. Oxygen is present in functional groups such as alcohols, esters, ketones, carboxylic acids and anhydrides whereas sulfur is found in sulfides, sulfoxides as well as in thiols and thiophenes. Nitrogen is found in pyrrolic and pyridinic structures but also in 2-quinolones. [13] Beside molecule formation due to covalent bonding other physical-chemical interactions (inter and intra-molecular) occur in bitumen and have an important impact on physical and chemical properties of the binder. Especially hydrogen bonding, dipole-dipole interactions [14] and π-stacking between molecules lead to the reversible formation of agglomerates, which leads to specific microstructures.

The view of bitumen structure has changed several times in the past century. A commonly used description of bitumen structure describes it as a colloid, where core-shell particles are merged into a low-polar matrix. In this model, smaller micelle-like structures agglomerate to form core-shell particles (a structured core surrounded by a broad continuous mantle) with diameters between 0.1-100 µm [15, 16]. Figure 4 depicts a simplified two-dimensional model, where high polar asphaltenes (described later in detail) are the main building blocks of the inner, solid core shell particles. The shell is built of aromatics and resins and the liquid-like matrix is mainly formed by low polar molecules from the aromatics and saturates fraction. [16] A qualitative scheme of the distribution of SARA fractions, within the mentioned regions is shown in Figure 5. Experimental evidence for this micelle-like structures and core-shell superstructures are the tendency of asphaltenes to agglomerate in crude oil and various solvents [16], in the mechanical behaviour of bitumen, which behaves like a viscoelastic substance, experiments by small angle neutron scattering (SANS) and small angel x-ray scattering (SAXS), thermal analysis and various diffusions experiments. [6]

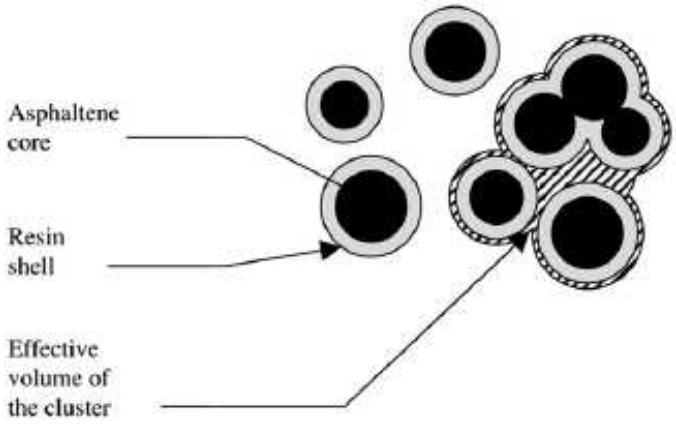

Figure 4: A simplified view of the colloidal structure of bitumen [6]

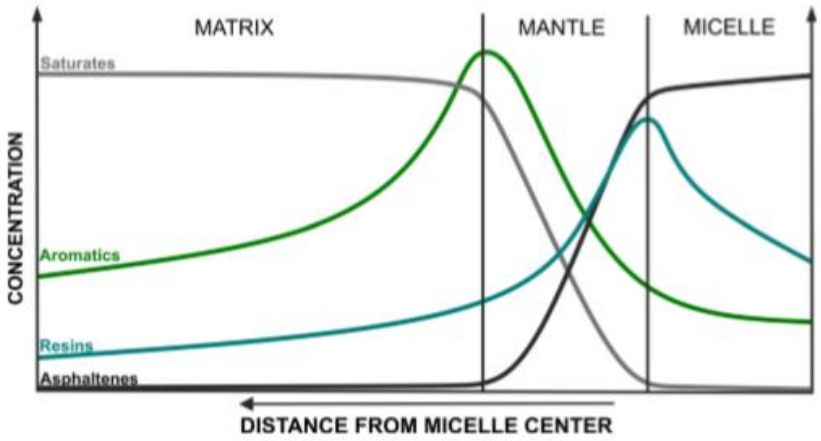

Figure 5: Distribution of the SARA fractions as a function of the distance from the Micelle center [16]

Furthermore, observations with high resolution microscopy techniques such as atomic force microscopy (AFM) and scanning electron microscopy (SEM) showed that self-assembly takes place as the structured core-shell particles form microstructures on the surface. The core of these features is structured and consists of alternating maxima and minima. The alternating pale and dark lines (observable in AFM) are reminiscent of bees, which is the reason why they are often referred to as 'bee-like' structures. However, the mentioned techniques just give evidence on structures present on the surface and do not provide clear evidence on the existence of such structures in the bulk *[17, 18]*. Another popular description of bitumen microstructure formation is that wax crystallization of linear alkanes is the main contributor of the emergence of such features *[6]*. But the consequences of the crystallization process on the microstructure of bitumen is not yet clear. Also, the contributions of those processes and an unambiguous differentiation between structures formed by both processes remains a topic of research.

2.1.1. SARA Fractions

The term SARA is an acronym and stands for "**S**aturates, **A**romatics, **R**esins and **A**sphaltenes". These are the fractions obtained after a polarity-based separation. Hence, the names just represent the classification of the polarity fractions and should not be confused with the presence of just one chemical class of compounds (e.g. solely saturated hydrocarbons in the saturates fraction) in the corresponding fraction. Corbett developed a method for obtaining those fractions via filtration and chromatography [19]. The reference method nowadays is a slightly adapted version of Corbett's approach. In a first step a weighed amount of a bitumen sample is dissolved in n-heptane and stirred for 1 h at temperatures of about 98 °C. This step leads to a mixture of dissolved and non-dissolved structures. To separate those, a dead-end filtration is applied. The dissolved compounds in the brown filtrate are called maltenes whereas the brownish-black solid precipitates are referred to as asphaltenes. [20]

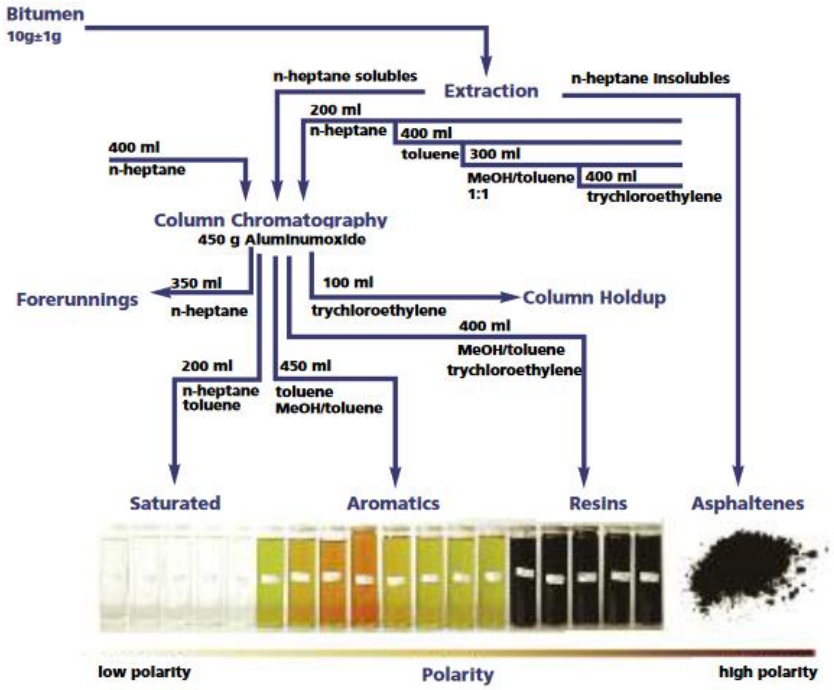

Figure 6: Classical separation pathway of bitumen [20]

Subsequently, the maltenes (dissolved in n-heptane) are put on a chromatographic column with CG-20 chromatographic grade alumina as a stationary phase. The first fraction, the saturates, appear to be transparent to slightly yellow in colour and make up for 5-15 wt. % of bitumen. [19] When this fraction is gathered completely the polarity of the mobile phase is enhanced by using toluene, followed up by a mixture of methanol and toluene as eluents, which leads to the elution of the aromatics fraction. The colour of this fraction is orange to brown and the mass content in unaged bitumen can reach 45 wt. %. [19] With a final increase in polarity, by using trichloroethylene as eluent, the remaining structures are obtained from the chromatographic column. This fraction is called the resins. It is brown to black in colour has higher viscosity than the previous obtained fractions and referring to [19] mass contents between 30-45 wt. %. The whole procedure is depicted in Figure 6 and can be summarized as a combination of dead-end filtration and liquid-solid chromatography with an applied polarity gradient.

Problem of this method are the huge columns needed for proper separation of the fractions and the long retention time leading to a long separation procedure. To solve these two negative aspects Sakib, et al. [1] developed an adapted separation technique called *Fast SARA*. In this technique the big glass columns (100-200 cm) are replaced by small solid phase extraction columns (15 cm), the solvents are optimized and a standardization and condensation of significant processes are implemented. This rather analytically based approach gives better reproducibility and a faster separation. Further insights in this technique are given in the corresponding chapter 2.3. and the experimental implementation is given in chapter 3.1.

2.2. Binder Ageing

Binder ageing is often referred to as deterioration of mechanical properties (e.g. rheological behaviour of bitumen) with time. One accessible mechanical property to monitor changes in the material is viscosity. Figure 7 depicts the increase of ageing index, which is derived as ratio of viscosity at a certain time to viscosity at the start, with time. According to Figure 7, binder ageing can be separated into two different parts often referred to as short and long-term ageing. The viscosity increases linear in each of the two phases but with different slopes. [14, 21]

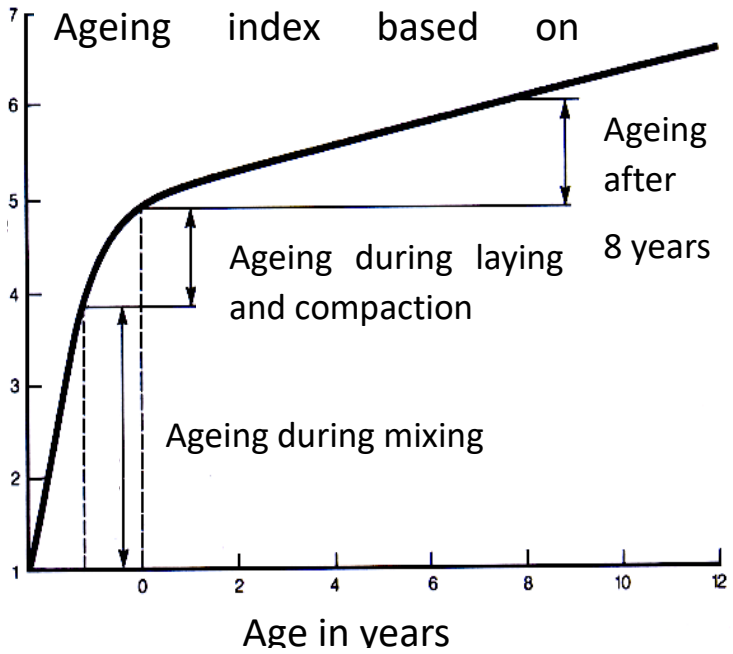

Figure 7: Viscosity based ageing index plotted against time in years [21]

The first process, the short-term ageing is a fast process which happens within 24 hours during the mixing and paving of asphalt at higher temperatures. The second process occurs during the service-life of bitumen where the influence of radiation, heat, atmospheric gases and mechanical load affects the chemo-mechanical behaviour of bitumen. The two phases of binder ageing are described chemically by Petersen as a dual sequential mechanism. [21] For chemical investigations one has to take into consideration that the main reason for ageing is oxidation. With that said, the first process, the so-called spurt, is depicted in Figure 8. Petersen explains mechanistic occurrences by using 9,10 dihydroanthracene as a model compound which has a comparable relative reaction rate to bitumen overall [21, 22]. These aromatic compounds are not entirely aromatized, are thus prone to react with oxygen to form different peroxides (hydrogen peroxide or perhydroaromatic hydroperoxides). These instable intermediates either decay in a radiation and/or heat induced process or interact/react with sulfides. The cleavage of peroxides (depicted in the third reaction of Figure 8) leads to free and very reactive radicals whereas the reaction between peroxides and sulfides generates sulfoxides, water molecules and anthracene. Therefore, a rise of sulfoxides and aromaticity during the first oxidation step is a direct consequence of this possible mechanistic route. The emerging radicals are seen as contributors in ongoing oxidation processes containing benzylic carbons, which are promoting the formation of ketones. By conducting the spurt at different temperatures, the experiments of Peterson suggested that especially ketone formation is dependent on the temperature. At higher temperatures more ketones emerged which was linked to the fact that the formation of radicals from peroxides is temperature sensitive. To sum this up: the higher the

temperature during the spurt the higher the formation rate of free radicals from peroxides which finally leads to higher amounts of ketones. [21]

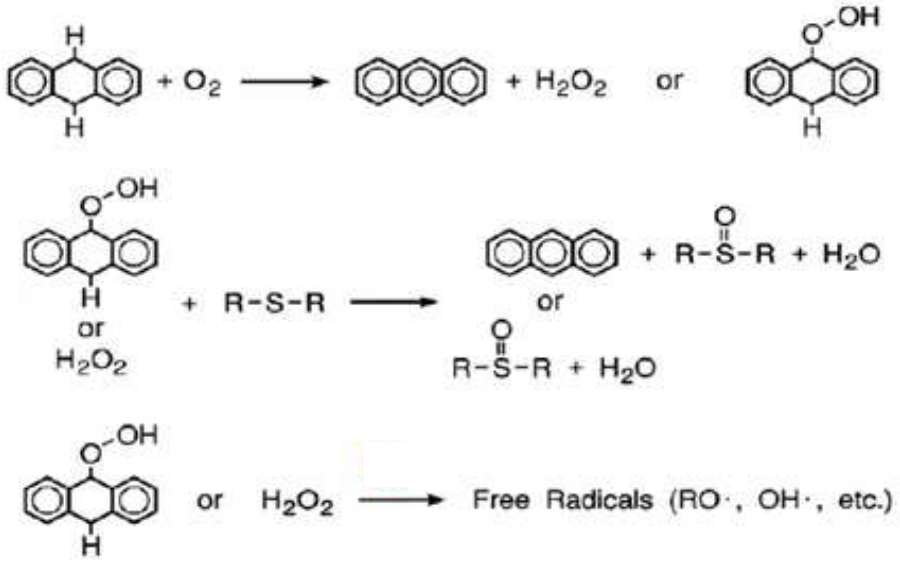

Figure 8: Formation of Free radicals, sulfoxides and anthracene from the model compound 9,10 dihydroanthracene [21]

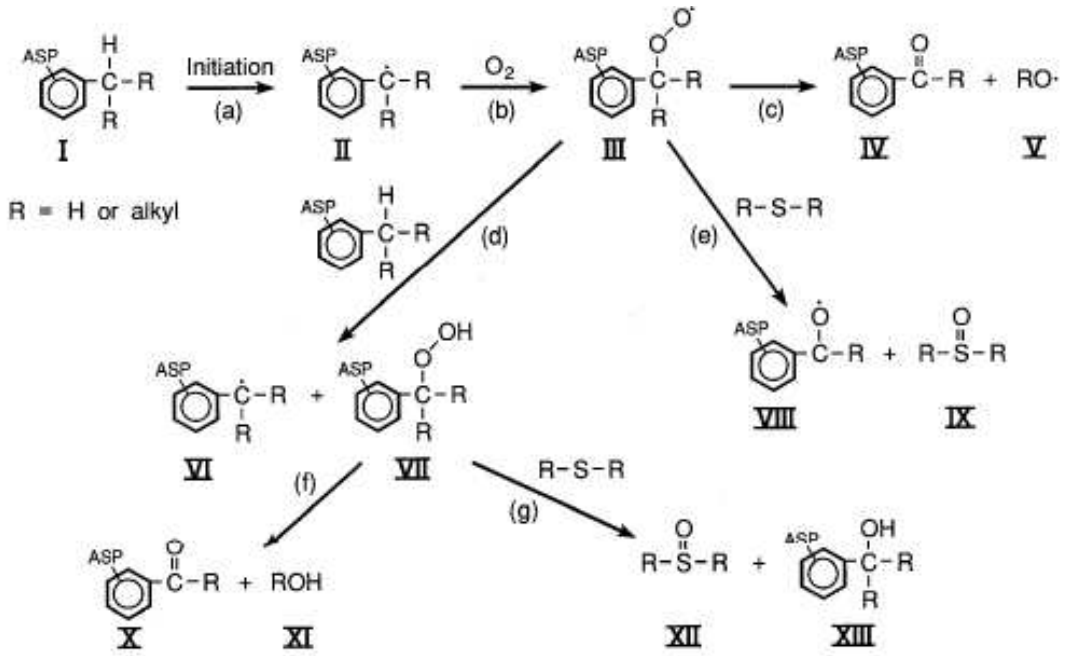

Figure 9: A reaction scheme of possible oxidation pathways [21]

Different further reaction pathways are possible and are shown in Figure 9, where the formation of ketones, sulfoxides and further radicals are explained. The educts, intermediates and products of each pathway are classified with roman numerals from I to XIII. The main reactive class of compounds for these processes are carbons with one to three benzylic groups attached. The initiation reaction (due to free radicals, radiation or heat) leads to radical intermediates which are stabilized by the surrounding benzylic groups (mesomeric effect[3]). After that, oxygen (or reactive

[3]The electron density (probability density) of π-electrons in conjugated systems (e.g. aromats) extends over several atoms. The electrons are delocalized. Their mobility can influence the stability of specific transition states (ionic or radical) in such a way that e.g. lone electrons of emerging radicals delocalize in conjugated

oxygen species) can react with the first radical intermediate to form a slightly more stable peroxyradical (III). For this second intermediate Petersen proclaimed three further pathways. The first one is a rearrangement reaction, where a ketone (IV) and an alkoxy radical emerges. In the second pathway the intermediate (III) reacts with educt structure (I) by taking the weakly bonded hydrogen. This leads to the formation of intermediate (VI), which is chemically similar to intermediate (II), and a peroxide (VII). This peroxide can rearrange itself (related to the process of III to IV) and form ketones (X) and alcohol. On the other hand, peroxide (VII) can interact with sulfides to form sulfoxides and further alcoholic groups. This is similar to a third pathway from intermediate (III), where the peroxyradical (III) reacts with sulphides to form sulfoxides. [21]

However, the mechanisms shown and described above do just consider atmospheric oxygen as main initiator and oxygen source. However, by taking a closer look into the composition of atmospheric air other partially abundant substances should be included especially for initiating processes. As main contributors from the air reactive oxygen species (ROS) such as nitrogen oxides (NO_x), tropospheric ozone (O_3) and hydroxyl radicals ($OH\cdot$) are far more reactive than molecular oxygen, and thus have to be considered as first external initiators. Therefore, these next points are going to focus on the occurrence and abundance of such reactive oxygen species.

Nitrogen monoxide (NO) and nitrogen dioxide (NO_2) are generally summarized as nitrogen oxides (NO_x). Due to their stability, they are the most abundant nitrogen species followed by less stable species such as NO_3, N_2O, N_2O_3 and N_2O_4, which are also found in traces in the atmosphere [23]. The main sources for NO_x are anthropogenic exhaust fumes, which arise from the combustion of fossil fuels in the transportation - (cars and ships) [24] and the energy industry [25]. But natural processes such as thunderbolts can also lead to the production of nitrogen oxides. [26] The amount of nitrogen oxide is variable. It is higher in urban regions with high traffic and lower in average in natural areas. The share of nitrogen dioxide in the atmosphere on annual average is 5-50 parts per trillion (ppt) in Austria [27]. Ozone (O_3) is present in the stratosphere and in the troposphere of earth atmosphere. For oxidation processes on the ground only the tropospheric ozone has to be taken into consideration. This species emerges by the combined reaction of sunlight with gaseous hydrocarbons and nitrogen oxides. The amount of ozone present in the atmosphere is variable, depending on the time (day or night), place (above natural areas or cities with high traffic) and the height (which atmospheric layer) [27]. The annual average amount in Austria 2018 was 60 ppt (on average over all measuring stations) [27]. Finally, the hydroxyl radicals are very reactive intermediates of the ozone and nitrogen oxide cycles. They are the rarest of the three discussed ROS and have an average lifetime of less than one second in the atmosphere [28]. However, it is also the most widespread ROS in the troposphere; hence one of the major contributors to surface and hydrocarbon related oxidation processes. [28]

To simulate the processes explained in this chapter several laboratory ageing methods have been developed, which will be the topic of chapters 2.2.1, 2.2.2 and 2.2.3.

2.2.1. Common Laboratory Ageing

2.2.1.1. RTFOT

The spurt reaction appears at high temperatures typically slightly above 160 °C. This temperature is reached when the bitumen is mixed with different aggregates to form asphalt and during the paving process. A common method to simulate spurt-reaction ageing is RTFOT which stands for **R**olling **T**hin

systems, leading to a reduced local electron density and lower reactivity of such radical atoms in comparison to molecular systems without π-electron conjugation.

Film **O**ven **T**est [10]. In this procedure 1.25 mm thick films of bitumen are prepared in vessels, on which a rotating motion is applied. This happens in an oven at a temperature of 163 °C and for a duration of 75 min. [10]

2.2.1.2. PAV

The simulation of long-term ageing is generally implemented in **P**ressure **A**ging **V**essels (PAV). The long-term ageing occurs during the service-life of bitumen as an ingredient in roads, pavements and rooftops. The ageing in that areas of application is dependent on the position of the bitumen inside the material/pavement the general thickness and the porosity. Beside these material dependencies, long-term ageing is also strongly dependent on traffic and the climate of the area where it is used. [11, 6]

The problem of this ageing method is that it does not deal with realistic conditions and therefore does not simulate the long-term ageing process very well for most cases. One has to consider that neither dark environment, nor pressures up to 20 bar and temperatures above 90 °C depict conditions of the daily life of bitumen. Therefore, another ageing set-up, developed by Mirwald et al. [12] is included in the studies and briefly described in chapter 2.2.3.

2.2.2. Field Ageing

Test fields (the sum of all asphalt slabs) are created in general to investigate the changes occurring to bitumen under climatic/atmospheric conditions, hence, more realistic conditions. Asphalt slabs of magnitudes of 50 x 26 x 10 cm were produced with base bitumen, limestone used as a filler and porphyritic aggregates. The content of bitumen was 5.4 % by mass and the mixing temperature was 160 °C. After 5 years the slabs were excavated and the bitumen was extracted according to the laboratory standard EN12697-3 (solvent: tetracholoroethene). [29]

2.2.3. Viennese Binder Ageing

Another method to simulate ageing was implemented by Mirwald et al. [12]. For more realistic simulation of binder ageing in the laboratory the atmosphere is altered with reactive oxygen species (ROS). Atmospheric oxygen, traces of ozone and nitrogen oxides (NO_x) are added by leading compressed air through an ozone generator. The processes that appear are shown in the following equations:

$$O_2 + E(498kJ\ mol^{-1}) \rightarrow 2O\cdot \quad (1)$$

$$O\cdot + O_2 + M \rightarrow O_3 + M \quad (2)$$

$$N_2 + 2O\cdot + M \rightarrow 2NO\cdot + M\cdot \quad (3)$$

Eventually, the emerging nitrogen monoxides [30] will get further oxidized by ozone to form nitrogen dioxide *(4)*.

$$NO\cdot + O_3 \rightarrow NO_2\cdot + O_2 \quad (4)$$

The oxidation of NO_2 to the photo-instable NO_3 compound is a further consequence of the given settings. Due to the absence of UV light the ageing processes that appear in this set-up in bitumen can be compared to night-time reactions occurring in the darkened atmosphere [23]. With that said, the ageing atmosphere used in this set-up provides the reactive oxygen species, O_3 and NO_x, in combination with enhanced temperatures to simulate binder ageing. The main difference to realistic atmosphere is the absence of OH-radicals and the missing UV-A alteration necessary to produce them. In particular, simulated daylight experiments will be a topic of great importance in the future. Figure 10 depicts the whole setup implemented for this ageing method.

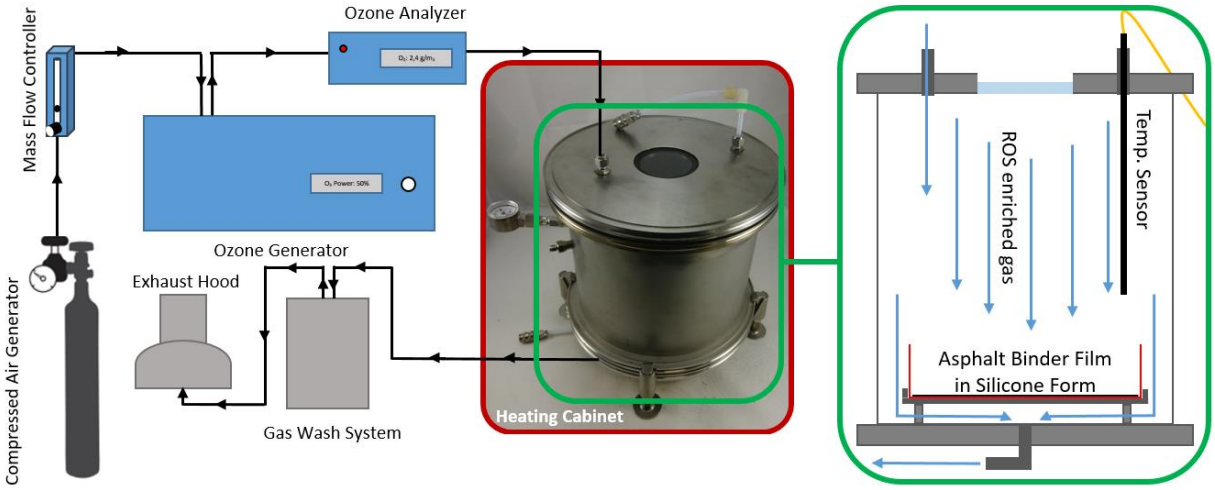

Figure 10: Scheme of the VBA ageing setup [12]

Compressed air is led through a mass flow controller and an ozone generator (Anseros ozone generator COM-AD-1) at a defined flow rate. A thin bitumen film of 0.5 mm is exposed to this ROS enriched atmosphere. The gaseous stream is measured with an ozone analyzer (Anseros Ozone analyzer GM-OEM). For the studies in this thesis two different concentrations of ozone content were chosen with 2.4 and 12 g O_3 m^{-3}. The temperature was set at 80 °C for all experiments and the ageing duration was three days for all three binders each and an additional 12 day-run for binder B287. The preparation of the unaged bitumen samples was implemented by heating them up for a short period of time (< 5 min) followed by a transfer into a metal container with a diameter of 160 mm. After that, they were pre-aged in an oven at 163 °C for 75 min to simulate conventional short-term ageing. The 0.5 mm thin samples were finally put into the VBA aging cell were the gas flow and temperature were adjusted and the ageing process was implemented. [12]

2.3. Fast SARA

Following the separation principle of SARA chromatography, outlined in chapter 2.1, this adapted application, developed by Sakib, et al. [1] will be described in detail in this chapter. The first step of the procedure is the separation of the n-heptane solubles from the insolubles. Therefore, the bitumen sample is mixed with n-heptane and stirred at room temperature for 24 h. This is followed by a vacuum filtration in syringes with syringe top filters. The filtrate, containing the maltenes fraction (n-heptane insolubles), is further separated using a chromatographic system. In the fast SARA setup, the huge chromatographic columns are replaced by small solid phase extractions columns (SPE), where the stationary phase is industrially pre-packed in syringes. The chromatographic separation in the SPE columns is further implemented with varying mobile phases. Starting with a low polar solvent and increasing the polarity stepwise for each fraction from saturates (lowest polarity) to resins (highest polarity). With that said, discrete steps in polarity are applied to obtain the fractions one by one. Exact data for the implementation of the whole separation are given in chapter 3.1. [1]

The implemented system for the Fast SARA procedure can be labelled as normal-phase chromatography. In such a technique the molecules can be separated due to their affinity to a polar stationary phase. Figure 11 depicts such a system with a polar stationary phase and an increasing polarity of the mobile phase from left to right (indicated with the arrow on the bottom). [31]

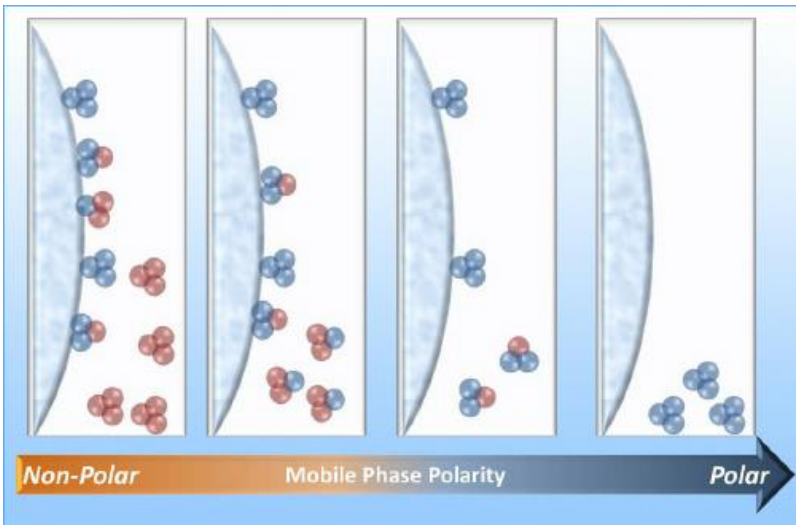

Figure 11: Illustration of the principle of normal-phase chromatography [32]

In the beginning of this procedure maltenes were dissolved in a low polar mobile phase (n-heptane) and added to an extraction column. There, the polar stationary phase interacts more with the polar compounds leading to a physical adsorption of these molecules whereas the compounds with lower polarity remain in the mobile phase and are washed through the column. By choosing a low polar mobile phase at first, just the least polar molecules go through the column, whereas the other fractions stick to the stationary phase. After that, the polarity of the eluent is increased and fraction by fraction can be gathered. [31]

To go a little bit further into the theory one has to understand the meaning of polarity in molecules and how this property effects various interactions. In chemistry, polarity is defined as the vector sum of all electric dipole moments in a molecule which emerge due to separation of electric charges within the molecule. This separation of charges can be permanent or induced from an external electric field. If separated charges do not counteract each other the vector sum of all dipole moments (between singular atoms) in the molecule lead to a net dipole moment with a defined direction and length, which defines the polarity of molecules. The higher this net dipole moment is the higher is the polarity of the molecules. As an empirical approximation the following Latin line is known since the middle ages: “Similia similibus solvuntur”. This means that similar substances will dissolve similar substances. The same tendencies are appearing in the extraction column, where polar molecules are stronger linked to a polar stationary phase than apolar molecules. The general behaviour can be described by Nernst’s distribution law: [31]

$$K_{d,i} = \frac{c_i^{stat}}{c_i^{mob}} \tag{5}$$

c_i^{stat} ... Concentration of compound i in the stationary phase (mol*l^{-1})

c_i^{mob} ... Concentration of compound i in the mobile phase (mol*l^{-1})

$K_{d,i}$ ... Distribution coefficient of compound i between stationary and mobile phase (-)

This means for a very polar molecule that increasing polarity of the mobile phase leads to a higher concentration in said phase and a lesser concentration in the stationary phase. [31]

2.4. Fourier Transform Infrared Spectroscopy

2.4.1. Interaction between Light and Matter

Infrared spectroscopy is a common tool for qualitative and quantitative analysis of substances in every state of matter. The main principle is the interaction between infrared radiation and molecules and condensed molecular systems (liquid, crystalline, semi-crystalline and amorphous). Infrared light is an electromagnetic wave in the wavelength region of 780 nm to 1 mm (12.800 cm^{-1} to 10 cm^{-1}). The energy of infrared light is suited to excite the quantum states for rotation and vibration of molecular compounds. But just a specific energy and with that a specific wavelength corresponds to a specific excitation mode. This resonance condition is mathematically described in equation *(6)*:

$$E_n - E_m = \Delta E = h * \nu = h * \frac{c}{\lambda} \tag{6}$$

E_i …… Energy of the vibrational eigenstate i (J)

h ……Planck's constant ($6.626*10^{-34}$ J*s)

ν …… Frequency of the electromagnetic wave (s^{-1})

c …… Speed of light (in vacuum $2.99792*10^{8}$ $m*s^{-1}$)

λ …… Wavelength (m)

The specificity in excitation is caused by the fact that vibrational eigenstates cannot obey any energy, but rather have certain energy levels. These energy levels are obtainable by solving the Schrödinger equation for a harmonic oscillator which leads to equation *(7)*.

$$E_i = h * \nu * \left(v_i + \frac{1}{2}\right) \tag{7}$$

v_i …… Vibrational quantum number (0, 1 ,2, 3, …)

The frequency ν of the vibration is a function of the force constant and the masses of the oscillating atoms.

$$\nu = \frac{1}{2\pi} * \sqrt{\frac{k}{\mu}} \tag{8}$$

k …… Force constant (kg/s^2)

μ …… Reduced mass (kg)

Equation *(7)* shows that the energy levels of a harmonic molecular oscillator are discrete and that a zero-point energy, unequal to zero, is inherent in such systems. A further consequence is that the energy states are equidistant. The dependency of potential energy on the internuclear distance of vibrating atoms can be described by the harmonic potential. In this concept there is one energetically preferred distance between two molecules. Decreasing and increasing the internuclear distance lead to increasing potential energies but the atoms can draw infinitely close to each other and there is no dissociation of molecules in this model. This does not fit well to the physical reality; hence, the concept of the anharmonic potential has to be applied, which leads to better mathematical modelling of reality. The necessity to expand the model gets more understandable by looking and measuring the behaviour of real molecules. Because they do have measurable dissociation energies (as e.g. molecules can break up) and the potential energy during the compression of a bond by a

definite distance increases rapidly faster in reality (as deploying repulsion forces between the nuclei get more significant the smaller the distance gets). [33, 34]

Anharmonic potentials can be represented by approximation functions, such as the Morse potential given in equation *(9)*. A comparison between the harmonic and the anharmonic potential as functions of the internuclear distance are shown in Figure 12. [33, 34]

$$V(r) = D_e * (1 - e^{\sqrt{\frac{k_e}{2*D_e}}*(r-r_e)})^2 \quad (9)$$

V(r) ……Anharmonic potential as a function of r (J)

D_e …… Dissociation energy (J)

k_e …… Force constant near the minimum of the potential (J/m²)

r …… Distance between the masses (m)

r_e …… Equilibrium bond distance (m)

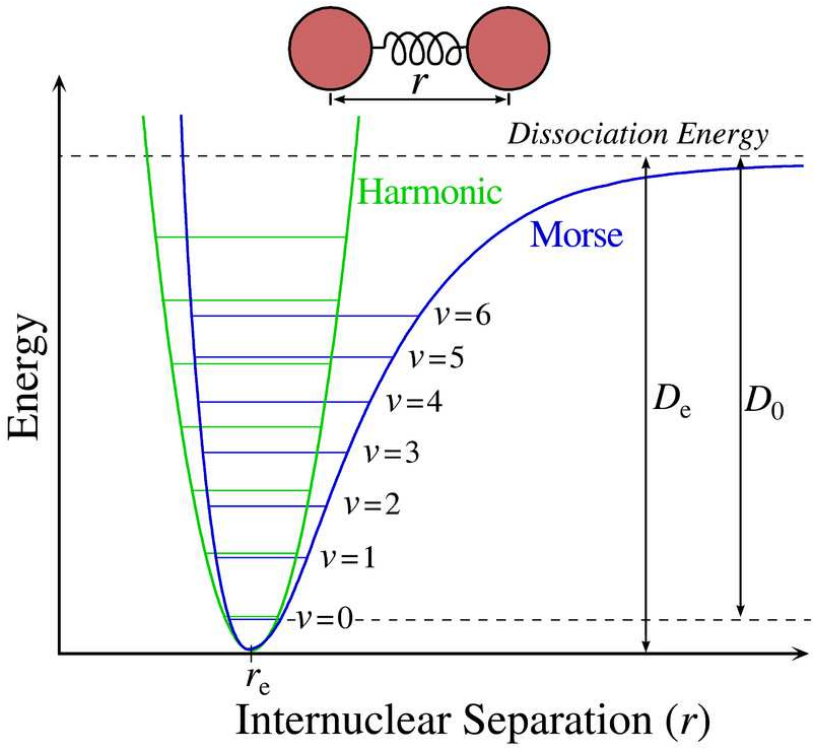

Figure 12: Comparison of the harmonic and the anharmonic (Morse) potential energy curve as a function of the internuclear seperation (r) [35]

Using that potential to solve the Schrödinger equation the solution for the energy eigenstates changes to the following definition [33, 34]:

$$E = hv * \left(v + \frac{1}{2}\right) - hv * x_e * (v + \frac{1}{2})^2 \quad (10)$$

x_e …… Anharmonicity

A further consequence of anharmonicity is a decreasing energy gap between vibrational eigenstates with increasing potential energies. However, the decrease is constant, which implements that there are finite numbers of energy states until the dissociation energy is reached. Due to this decrease, the selection rules for an anharmonic oscillator have to be modified and can be described as follows: [33, 34]

$$\Delta v = \pm 1, \pm 2, \pm 3 \ldots \quad (11)$$

The transitions greater ±1 are called overtones of a particular vibration mode and are measurable in the near-infrared region.

Degrees of Freedom

To determine vibrations of molecules one can calculate all internal degrees of freedom of this molecule. As every atom in a molecule with N atoms can move in all three spatial directions, 3N possible motions are conceivable. For vibrational motion one has to exclude 3 translational motions and 2 (linear molecule) or 3 (non-linear molecule) rotational motions which is given in equation *(12)* and *(13)*:

$$F(linear\ molecule) = 3N - 5 \quad (12)$$

$$F(non - linear\ molecule) = 3N - 6 \quad (13)$$

However, the degrees of freedom do not represent the actual bands observable in the infrared spectrum. The condition for infrared active vibrations is that the dipole moment has to change as a function of the direction of the vibration. This can be specified mathematically by the following equation:

$$\frac{\partial \mu}{\partial x_i} \neq 0 \quad (14)$$

μ_i .....Electrical dipole moment of the molecule (D=Debye; or A*m*s [SI])

x_i ..... Vibration in the direction x_i (m)

Example

As an example for these last theoretical definitions the ethane molecule (representing hydrocarbons in general) will be discussed shortly.

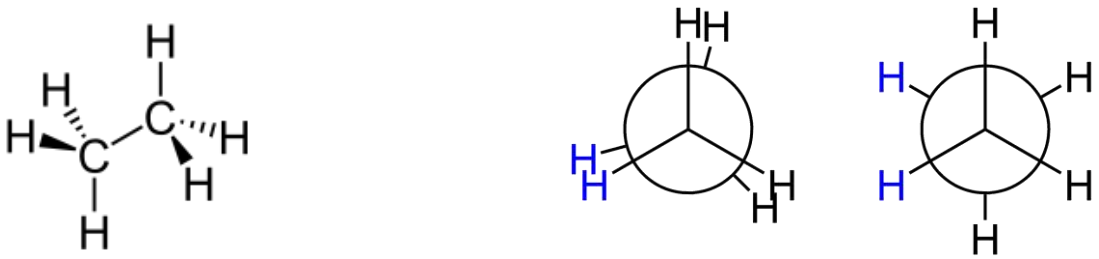

Figure 13: The structural formula of an ethane molecule (left) and the newman projection of the staggered and the eclipsed conformer (right)

Figure 13 depicts the structure and two conformers of an ethane molecule. With that, the degrees of freedom for this non-linear molecule are 3*8-6=18. As there is a point of inversion (in the more stable eclipsed conformer) the exclusion principle (the vibrations are either IR- or Raman-active) is valid. A symmetric stretching vibration between the two carbon atoms do result in a dipole moment change as a function of stretching or bending. Hence, an IR signal can be measured. This would not be the case if the molecule has a mirror plan perpendicular to the C-C bond (in the staggered conformer). In that case the symmetric stretching vibration results in a net dipole moment change of zero, hence, an IR-inactive vibration. Furthermore, the C-H vibrations can be separated into

stretching and different kinds of bending vibrations. (Figure 14) To differentiate different vibration modes they are categorized by using common nomenclature, summarized in Table 1.

Table 1: Nomenclature of different vibration modes

Symbol	Vibration mode
ν_s	Symmetric stretching vibration
ν_{as}	Asymmetric stretching vibration
δ	Deformation vibrations
s, τ, ρ, w	Scissoring, twisting, rocking and wagging as more exact definitions of specific deformation vibrations

Those symbols will be used in this work excessively; hence, a visualization to connect those symbols with actual vibrations is given in Figure 14:

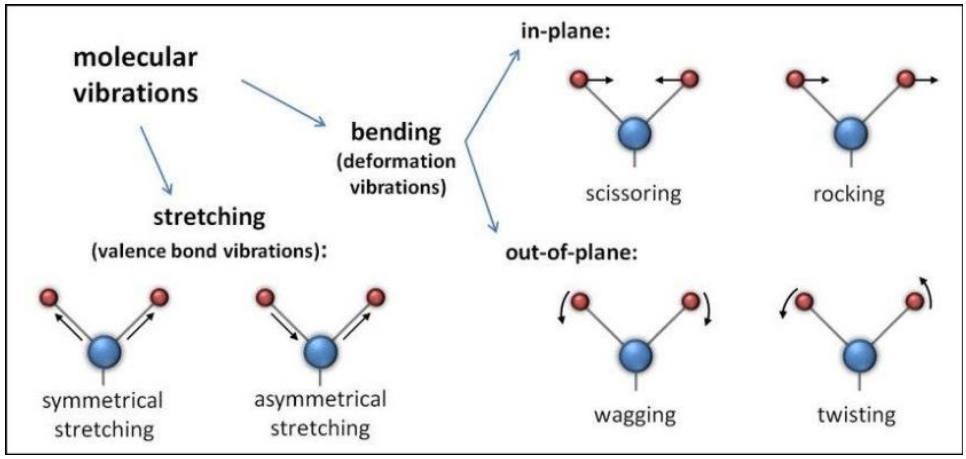

Figure 14: Vibration modes of an alkyl group [36]

Coming back to the given ethane example by comparing the C-C and C-H-stretching vibrations one can qualitatively deduce from equation *(8)* that the C-H bonds oscillate at higher frequencies, due to the lower reduced masses and a higher force constant. Especially symmetry considerations define which vibrations are infrared or Raman active. The application of symmetry concepts in vibrational systems and vibrational spectroscopy is generalized in the group theory of molecules. In this theory character tables of groups with finite elements (e.g. a specific symmetry class) can be derived and contain information on properties of molecules within this group. With such tools every possible IR-vibration of a molecule is derivable. [34]

Furthermore, considering that ethane is a gas at room temperature a measured spectrum does not just comprise the vibrational bands but also rotational-vibrational band splitting. The number of bands increases significantly and the spectrum gets more complicated. The bands and band gaps of such rotational-vibrational spectra are derivable using quantum mechanical methods such as ab initio Hartree-Fock, configuration interaction (CI), multi-configuration self-consistent field (MC-SCF) methods or ab initio density functional theory methods (DFT). [34] However, the substances objected in this thesis are complex mixtures of molecules and are highly condensed; hence, a priori calculations of infrared spectra are beyond the scope of this thesis and will not be discussed any further in this work.

2.4.2. Instrumentation of FTIR

2.4.2.1. Radiation Source

Infrared light can be produced and used in a variety of ways. Depending on the analytical purpose sources are often differentiated by the spectral range in which they emit radiation. Infrared radiation is categorized in literature into near-, middle- and far-infrared light, where each category needs different sources. The source needed in the range of near infrared spectroscopy should emit radiation between 780 and 2500 nm. The sources that are most commonly used are incandescent lamps such as tungsten-band lamps, quartz halogene light bulbs and light emitting diods (LED's). [37]

Opposed to that the main sources for middle infrared light are the Nernst lamp and the Globar. The Globar is made of silicon carbid (SiC) which is heated up to temperatures of 1200 °C. The glowing rod used in a Nernst lamp is a ceramic composed of zirconia oxide (ZrO_2) and yttrium oxide (Y_2O_3), which is heated up to temperatures between 900 and 1700 °C. The physical principle of light emission in these sources is that they are behaving like blackbodies. Radiation emitted by the idealistic system of black bodies following Planck's law of radiation given in equation *(15)* and the resulting curve is shown in for five different temperatures. [37, 34]

$$B(\nu,T) = \frac{2 * h * \nu^3}{c^2} * \frac{1}{e^{\frac{h\nu}{k_b T}} - 1} \tag{15}$$

B(v,T) ..... Spectral radiance of a body ($W \cdot sr^{-1} \cdot m^{-2} \cdot Hz^{-1}$)

k_b ..... Boltzmann constant ($J*K^{-1}$)

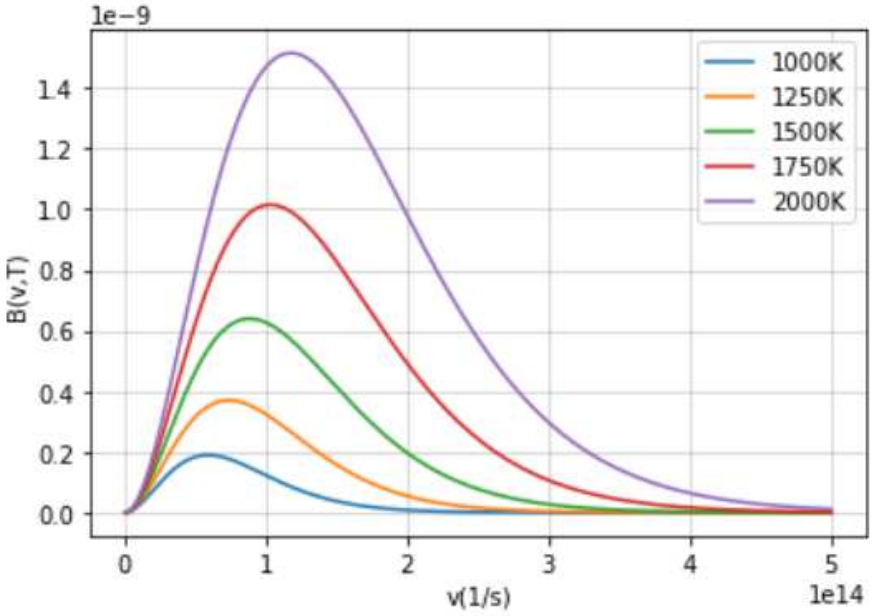

Figure 15: Planck curves at five different temperatures

By varying the temperature of the black body source one can shift the maximum spectral radiance to the wavenumber region of choice. Thus a broad spectrum with a maximum intensity in the region of infrared light can be used as an IR source for infrared spectroscopy.(see Figure 15) The light itself is produced by a process called spontaneous emission. In this process the transition of excited electrons (higher rate of excitation, due to energy/temperature input) to lower energy states (a statistical process driven by thermodynamics) leads to emission of energy (difference of both states) "disguised" as heat (radiation-free transition) or radiation. [37, 34]

The sources used for Far-Infrared spectroscopy are high-pressure mercury-vapour lamps. A mercury plasma source is formed by electrical excitation of the system. This leads to emission of continuous radiation up to wavenumbers of far-infrared light. [37, 34]

2.4.2.2. Attenuated Total Reflection Mode

The produced IR beam is directed toward the sample. Depending on the physical state and the diffraction index of the sample various modes of interaction can be chosen, ranging from transmission, diffuse reflection to total reflection spectroscopy. For all of these different approaches Lambert-Beer's law describes the intensity loss in the light beam due to the interaction of radiation with matter:

$$dI = -I_0 * \alpha * c * dx \tag{16}$$

dI ..... Intensity change though an infinitely small distance (W/m^2)

I_0 ..... Intensity of the beam before the interaction (W/m^2)

α ..... Absorption coefficient

c ..... Concentration of the infrared active compound in the sample ($mol*l^{-1}$)

dx ..... Infinitely small distance through the sample (m)

As we are dealing with a highly viscous black substance, the measurements were implemented in attenuated total reflection (ATR) mode. Transmission spectroscopy of bitumen is nearly impossible due to the high absorbance of this substance, and dissolution in a suitable solvent is also not desirable because the information about the microstructure is lost. In ATR mode, the sample is applied on a crystal with a high optical density, such as a diamond. The light is directed into the crystal where the light beam is refracted towards the normal following Snell's law at first. After that, the beam propagates to the interface crystal-sample. The propagation of the beam from the material with higher optical density (crystal) to the air/sample with lower optical density lead to the refraction from the normal. At a certain angle between beam and surface, called the angle of total reflection, the beam is refracted parallel to the interface. Any lower angle lead to the physical phenomenon that the beam is reflected entirely into the material with higher density which is referred to as total reflection and is widely used in applications such as transport of information in fibreglass. [37, 34]

Despite total reflection, the beam loses some energy during an interaction with the sample. This is not explainable by only considering the classical theorems of optics but can only be described using quantum mechanics. In the quantum theory there is a certain probability, unequal to zero, for the existence of a wave beyond the boundaries of total reflection, derived from the fact that electric and magnetic fields cannot be discontinuous at the boundary. This wave is called an evanescent wave and it decays exponentially into the material. From this exponential decay the penetration depth d_e of the beam is derivable as a function of the wavelength λ, the angle of incidence θ and the refractive indices n_{21}: [37, 34]

$$d_e = \frac{\lambda}{2\pi\sqrt{sin(\theta)^2 - n_{21}^2}} \tag{17}$$

Therefore, the penetration depth for infrared measurements is around 1 µm but changes over the whole spectrum. [37]

2.4.2.3. Interferometer

The modern approach in infrared spectroscopy is via Fourier transformation of an interferogram that summarizes the light of all wavelengths. Hence, all wavelengths of IR radiation can be measured simultaneously. The three main advantages of this technique are the Jacquinot-, Fellgett- and Connes

advantage. [37] Jacquinot advantage refers to the higher throughput of light and with that higher intensities. The Fellgett advantage is also called multiplex advantage and describes improvements in signal-to-noise ratio. Finally, the Connes advantage arises due to the very accurately known frequency scale, which leads to controllable calibration of the wavelength domain and with that to the possibility of mirror-movement averaging. [37] The interferometer used most is the one conceptualised by Michelson. Figure 16 shows a model of this interferometer type [33]:

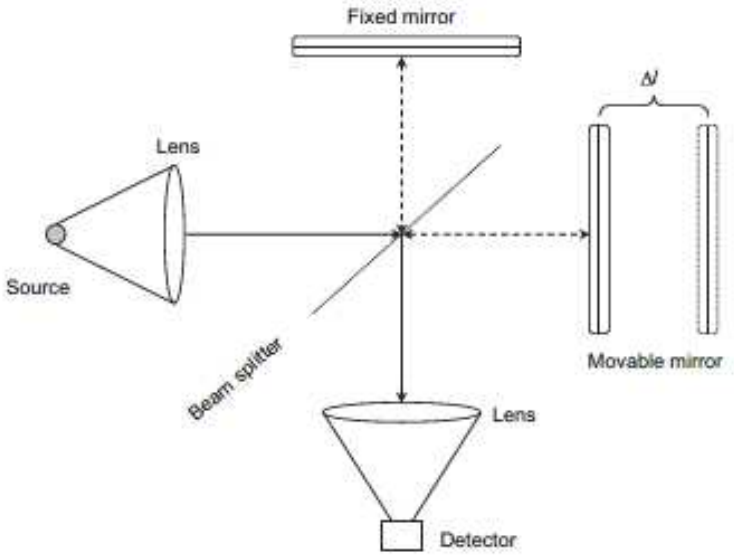

Figure 16: Michelson Interferometer [33]

The infrared light is split into two separate beams at a beam splitter. 50% of the light is transmitted to a moveable mirror and 50% is reflected in an 45° angle to a fixed mirror (only true for ideal beam splitter). These mirrors reflect 100% of the light, hence both light beams are reflected back to the beam splitter, where again one half is transmitted and the other half is reflected. If the electromagnetic wave is coherent another property of light comes into play that is called interference. If the reuniting light waves are in phase constructive interference occur, which leads to higher amplitudes. If both waves are out of phase, destructive interference appears and the light beam is completely extinct. In-phase imply that the added or shortened way of the light on the mutable road (movable mirror) has to be equal or an integer multiple of the wavelength λ. [33, 37, 34]

$$2\Delta L = n * \lambda \tag{18}$$

ΔL …… Difference in way length of the fixed-mirror-reflected- and the movable-mirror-reflected beam (m)

n …… Positive integer

The correlation between intensity (measured with the detector) and the spectral energy density at a specific frequency is given by the following equation.

$$I(x) = \int_{-\infty}^{+\infty} B(v) * cos(2\pi v x) * dv \tag{19}$$

I(x) ..... Intensity measured as a function of the way x (W/m²)

B(v) ..... Spectral energy density at a specific frequency v (W/m²)

These intensities (as a function of the way length difference) are measured with the detector and produce an interferogram. By using the other part of the cosines Fourier transformation pairing

(Equation *(20)*) one can convert these values into the spectral energy density at specific frequencies, hence, a spectrogram.

$$B(v) = \int_{-\infty}^{+\infty} I(x) * cos(2\pi vx) * dx \tag{20}$$

However, the Fourier transformation applied from minus to plus infinity would need an infinite mirror translation for maximum resolution. This is not possible in practice. The applied finite pathway of the mirror leads to the presence of sidelobes. To reduce such features an additional mathematical function, an apodization function (e.g. Happ-Genzel or Blackman-Harris) is added [37]. An exemplary interferogram and its corresponding spectrum are illustrated in Figure 17.

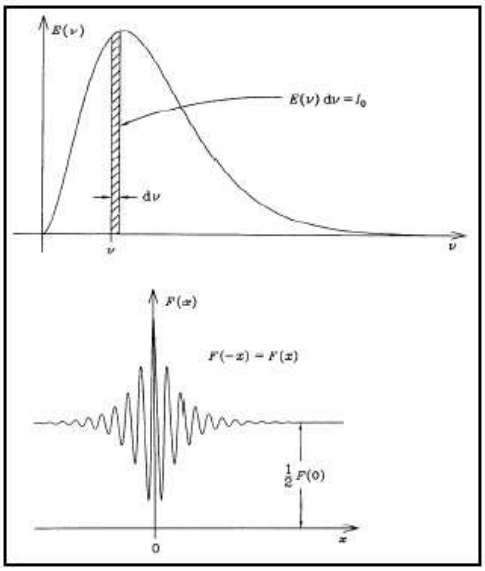

Figure 17: Interferogram of broad band radiation [38]

In this thesis a Perkin Elmer Spectrum Two- and a Bruker Vertex 80v spectrometer were used. Therefore, the implemented interferometers of both systems are going to be addressed briefly. In the Perkin Elmer device a rotating interferometer design is used. In such systems the pathway difference is obtained by adding a scan pair of mirrors in one pathway. These mirrors are parallel to each other and rotate synchronized back and forth. Hence, the pathway of the light in this arm is a function of the rotation angle. The complete interferometer system of modern Perkin Elmer devices is illustrated in Figure 18.

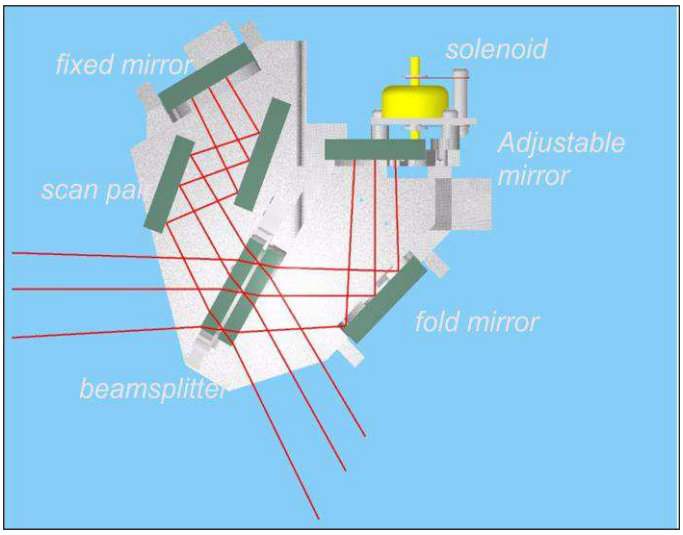

Figure 18: Dynascan interferometer of modern Perkin Elmer devices [39]

The Bruker Vertex v80 uses an UltraScan™ interferometer. The beam from the source is directed in an angle of 60° towards the beam splitter. The reflected beam is directed to the fixed mirror whereas the transmitted beam is further reflected at an TrueAlignment™ folding mirror and will finally head towards the moveable mirror. The whole beam pathway of a Bruker Vertex v80 device is shown in Figure 19.

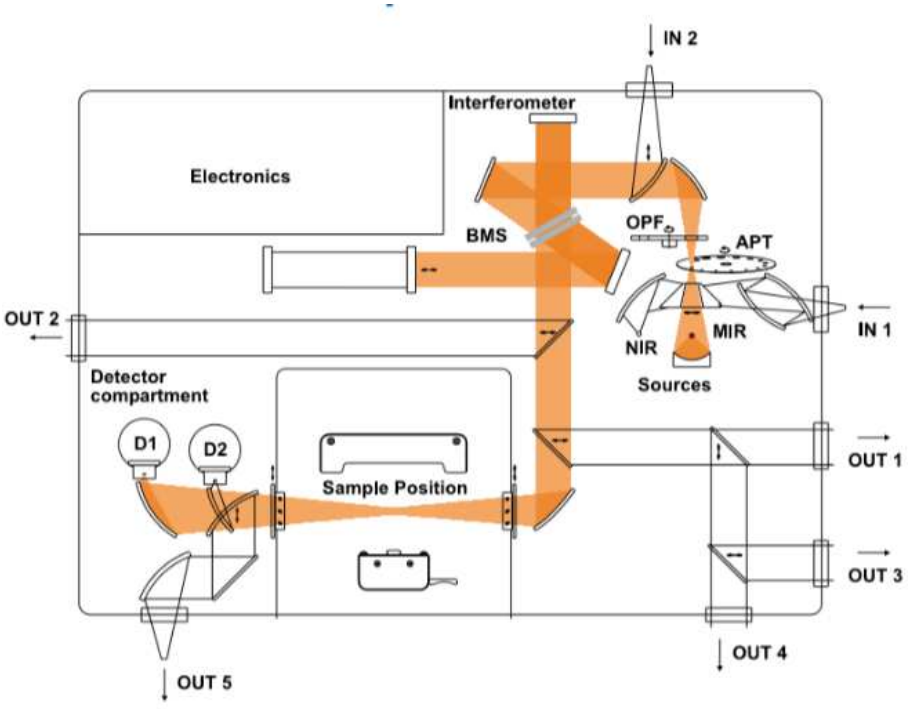

Figure 19: Beam path of a Vertex V80 [40]

2.4.2.4. Detector

The detection of infrared light is mostly implemented by two sorts of detectors: thermal and photo detectors. The Bruker Vertex v80 device used in this work uses a mercury-cadmium-tellurid (MCT) detector which corresponds to the category of photo detectors. The materials used in this kind of detectors are semiconductors, which (per definition) possess a small energy gap between valence and conducting band. An incoming photon beam with sufficient energy can excite electrons from the valence band to the conduction band of the semiconductor. An external readout integrated circuit

collects the electrons; hence, a transformation into an electric signal can be achieved. The response time and sensitivity of those detectors is very high, much higher than the best thermal conductors, but cooling is necessary in general to cut down thermal noises. [37]

The detector installed in the Perkin-Elmer Spectrum Two device was a deuterated triglycine sulphate (DTGS) detector which is a thermal detector. These detectors are based on the pyroelectric effect. Ferro electric crystals with asymmetric composition have an electric dipole moment and a permanent polarisation. Infrared radiation causes an increase in temperature in such crystals which leads to changes in interatomic distances and with that, changes in dipole moment and polarisation. Emerging charges on the surface can be measured as an electric signal which is proportional to the change in temperature. Cooling is not necessary for those types of detectors which lead to availability at room temperatures and with that, many different areas of application. [37]

2.5. Dynamic Shear Rheometer (DSR)

Mechanical testing has been the most important analytical approach for the classification of bitumen. There is a great range of different methods conceptualized in the last century to describe various mechanical properties of bitumen. Such conventional test methods are the needle penetration test and the softening point developed by Fraass. Opposed to them, performance-oriented methods like dynamic shear rheometer (DSR) and bending beam rheometer (BBR) have been developed, which can give detailed insights on certain properties by varying different parameters. In DSR two plates are used, where the upper plate is oscillating periodically with a certain frequency (the rotor) and the plate at the bottom stands still (the stator). Between those plates the bitumen sample is applied and the resulting shear strain is measured. By varying the temperature during these test runs the thermo-viscous properties of bitumen can be obtained. As the temperature goes down the material gets more viscous. This leads to an increase of torque that has to be applied to obtain a least amount of measurable deformation. The temperature ranges used commonly for DSR are 4-40 °C or 46-82 °C. With that said, information on the phase angle, the complex modulus and the master curve are obtainable with this method. [41] The specific practical implementation and the results of the experiments are given in chapters 3.3.2 and 4.1.2.

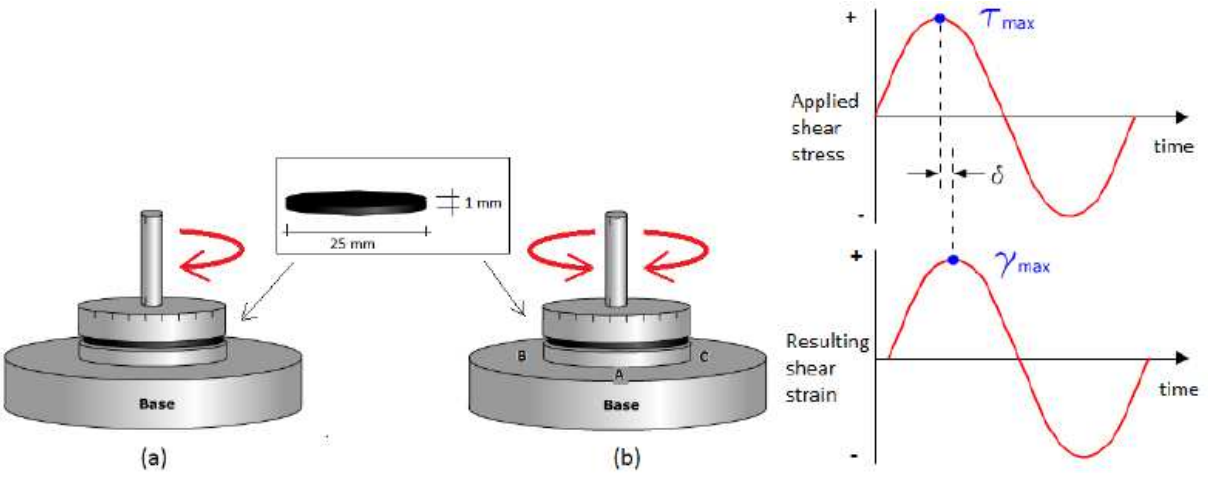

Figure 20: Theoretical background of DSR [42]

3. Materials and Methods

For this diploma thesis three bitumen samples from different sources were chosen. All of them have similar mechanical classifications according to European standardisation (penetration grade 70/100) but differ significantly in their chemistry and in ageing behaviour. Furthermore, the ageing procedures were described thoroughly in chapter 2.2, therefore, they will not be reiterated here. Hence, chapter 3.1 will cover the experimental set-up for the separation procedure as well as the implementation of the infrared spectroscopic analysis.

3.1. Fast SARA

Before describing the implemented procedure of Fast SARA step-by-step, Table 2 is presenting the number of conducted separations for each binder (B287, B504 and B637) in there different ageing states.

Table 2: Overview of the implemented SARA separations of each binder

Binder	Ageing grade (short)	Ageing grade	Trials
B287	A	Unaged	4
	B_LRTFOT	short-term laboratory ageing	4
	C_LPAV	long-term laboratory ageing	4
	C_VBA1	long-term laboratory ageing	2
	C_VBA2	long-term laboratory ageing	4
	C_Field aged sample	field ageing	2
B504	A	Unaged	4
	C_LPAV	long-term laboratory ageing	2
	C_VBA	long-term laboratory ageing	2
B637	A	Unaged	4
	B_LRTFOT	short-term laboratory ageing	4
	C_LPAV	long-term laboratory ageing	4
	C_VBA	long-term laboratory ageing	4

For each Fast-SARA separation 400 ± 40 mg of the binder was weighed in a 250 ml jar. Afterwards, 40 ml of HPLC-graded n-heptane and a magnetic stirring bar were added and the jar was closed. This mixture was stirred for 24 h ± 2 h at 200 rounds per minute. After that, 4x10 ml of the mixture were filtered by four syringe filters (Thermo Scientific™ Titan3™ PTFE (Hydrophobic) Syringe Filters, 25 mm diameter, 0.2 µm pore size) and washed with 5 ml n-heptane. The asphaltenes, the n-heptane insoluble fraction, remains in the filter, whereas the maltenes are in the filtrate. The maltenes are collected in four 40 ml vials and two of the four vials were dried on a heating plate at a temperature of 120 °C, while being flushed with a gaseous nitrogen stream. The main reason for flushing the solution with a nitrogen stream was to provide an inert gas atmosphere during evaporation of the solvent, while minimizing the oxidation of the respective binder fraction. Furthermore, this prevents boiling delays of the solution and accelerate the evaporation process.

The next step was to weigh the dried maltene fraction whereby the maltene content could be calculated by the following equation

$$m_{Maltenes}\% = \frac{\overline{m}_{maltenes,dried}}{4 * m_{bitumen}} * 100 \quad (21)$$

$\overline{m}_{maltenes,dried}$ ..... mean mass value of the dried maltene fractions (g)

$m_{bitumen}$ ..... mass of the bitumen (g)

The remaining maltene fractions were mixed with x ml of n-heptane to get a maltene concentration of 3.33 mg/ml. Equation *(22)* shows the formula to calculate the required n-heptane volume x:

$$x == \frac{m_{maltenes}}{3.33\,\frac{g}{ml}} - V_{Malteneфraction} \tag{22}$$

Figure 21: Fast SARA set-up

Figure 21 shows the SPE cartridges (Thermo Scientific™ HyperSep™ Silica Cartridges, 25 ml volume, 40 – 60 µm particle size) that were mounted onto the vacuum manifold and prewashed and saturated with 20 ml n-heptane. After that, the cartridges were moved to the next position on the manifold and 15 ml of the prepared maltene solution was added to each SPE cartridge and a flow of 3 drops per second was adjusted. After the addition of 10 ml n-heptane the cartridges were moved to a third position on the manifold. In this position the mobile phase was changed and 25 ml of a mixture of toluene and n-heptane (80:20) were added. At last, the cartridges were moved to the fourth position, where 40 ml of a mixture of dichloromethane and methanol (90:10) were added. The fractions, obtained dissolved in different solvents, were again dried on a heating plate (with N_2 flushing) until the solvents were evaporated and constant masses were achieved.

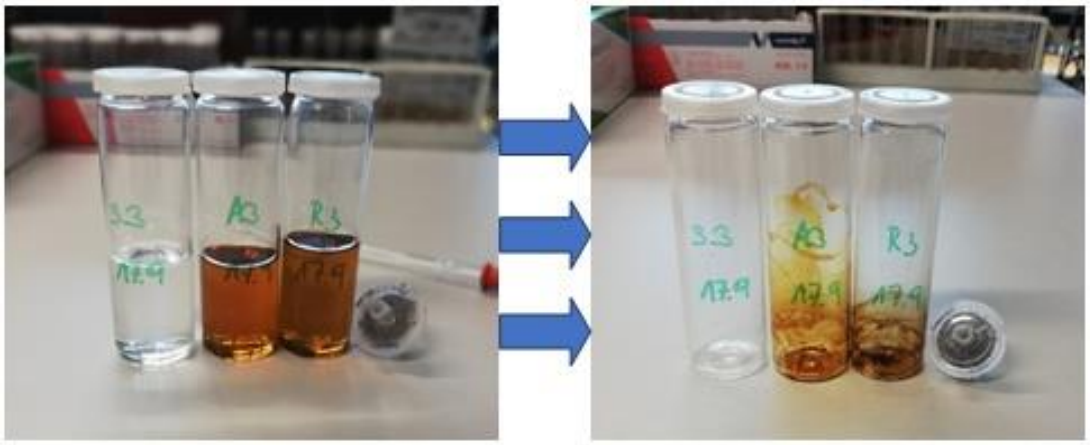

Figure 22: Obtained SARA fractions before (left) and after (right) drying

The asphaltene fractions, gathered in the syringe filters, were dissolved in DCM and rinsed into vials for the infrared measurements.

3.2. Infrared Spectroscopy

The chemical analysis was implemented with two different FTIR spectrometers. A Bruker Vertex 80v spectrometer and a Perkin-Elmer Spectrum Two spectrometer. Both were equipped with a Globar as infrared source. Hence, the optical parts (mirrors, beam splitter) to direct and split the beam were similar for both spectrometers. Moreover, in both devices ATR units with diamonds as crystals were used. The major differences between the two spectrometers are the detector (details in chapter 2.4.2.4), the interferometer (chapter 2.4.2.3) and the vacuum system. The Bruker Vertex 80v spectrometer uses an MCT detector; hence, had to be cooled down to 77 K (-196 °C) with liquid nitrogen to minimize the thermal noise and optimize the signal-to-noise ratio. Furthermore, the Bruker system is applied in vacuum, which reduces the water and carbon dioxide signals, produced by common molecules in the air and therefore optimizes the quality of the spectrum. In this system the whole beam pathway (also the whole ATR unit) is put under vacuum and the sample compartment above the ATR window is flushed with nitrogen gas. In comparison to that, the measurements with the Perkin Elmer spectrometer are at atmospheric pressure and the mentioned interfering signals are removed mathematically from the spectrum. The parameters were set equal to a spectral range from 680 – 4000 cm^1 and a spectral resolution of 2 cm^{-1} for both devices. But the number of scans varied as 48 scans were adjusted for the Bruker device and 4 scans for the Perkin-Elmer device. The reason for the chosen number of scans in the latter was that the quality of the Perkin-Elmer spectra has not changed significantly with more scans, but the time of measurement would have had. Comparing both devices, the 4 scan measurements on the Perkin-Elmer device took as long as the 48 scan measurements on the Bruker device. Additionally, a spectrum of the empty ATR crystal was recorded before every measurement as background. The obtained spectra were normalized at 2920 cm^{-1} and specific regions were integrated. The applied integration limits were as follows:

- Carbonyls (I_{CO}): 1800-1660 cm^{-1}
- Sulfoxides (I_{SO}): 1079-984 cm^{-1}
- Reference aliphatic band (I_{CH3}): 1525-1350 cm^{-1}
- Fingerprint Shift Area (I_{FPS}) : 1600-1100 cm^{-1}

The given name (e.g. Carbonyls) represents the predominant functional group in those regions and I_{CO}, I_{SO}, I_{CH3}, I_{FPS} are referring to the evaluated area between the curve and the baseline within the integration limits. Statistical evaluation of changes in those regions were carried out for the time-dependent studies using the following equations:

$$CO - Index\ (CO) = \frac{I_{CO}}{I_{CH3}} \qquad \text{Equation 23}$$

$$SO - Index\ (SO) = \frac{I_{SO}}{I_{CH3}} \qquad \text{Equation 24}$$

For the analysis of the general shift in this region between 1600 and 1100 cm^{-1} (see chapter 4.3.3) Equation 25) was applied.

$$Fingerprint\ Shift = \frac{I_{FPS}}{I_{CH3}} \qquad \text{Equation 25}$$

3.2.1. Analysis of Bitumen Samples

The measurement of bitumen was a very important part of this thesis. Bitumen samples from the time dependent studies, comparison studies of the spectrometers as well as each starting material of the Fast-SARA separations were measured with FTIR. The samples were heated up (max. 150 °C) for 3-5 min and homogenized afterwards by stirring with a spatula. After that, the samples for the time dependency studies were poured in DSR forms (see Figure 23) or poured on pieces of paper in the other cases. For each measurement, four similar samples for reproducibility within the binder were prepared. Furthermore, each sample was measured four times to capture the reproducibility of the spectrometer. The samples measured on the Perkin-Elmer device were additionally pressed against the crystal by applying a constant force using the provided stamp.

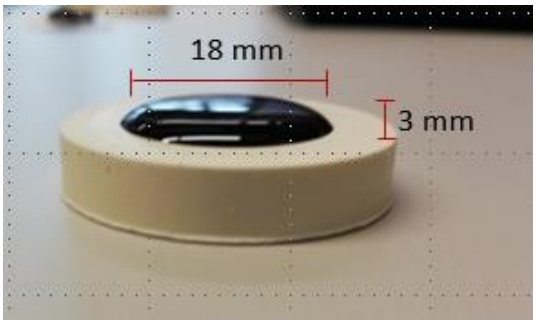

Figure 23: Silicon forms

3.2.2. IR Analysis of the SARA Fractions

To measure the saturates, aromatics, resins and maltenes, a small sample size of each fraction was picked up by the tip of a spatula and directly applied on the crystal. To get representative results, the amount of each fraction on the crystal were increased step by step, while IR measurements were made. This was implemented, until no change in the spectrum upon adding more substance was observable. The asphaltenes, which were collected in the syringe filters, were dissolved in DCM and washed into a vial. Due to the fact, that the asphaltenes are a solid powder complete coverage of the crystal could not be fully achieved. This led to lower intensities and interfering bands from cavities between powder and crystal, which contained air. Therefore, the asphaltenes were applied in solution on the crystal. The solvent was slowly evaporated and measurements of IR spectra with more intensity and less interfering bands were eventually feasible. For each fraction, four samples were applied on the crystal and each sample was measured four times.

3.3. Time Dependency Studies

To gather information on how chemical and mechanical performance of prepared bitumen samples can change with time, several time dependency studies were implemented. The following subchapters outline the different experimental approaches of each study.

3.3.1. Preliminary Tests

In the preliminary test runs all three binders in various ageing states were studied to capture time dependent changes. They were melted and homogenized as described before (chapter 3.2.1) and poured on small pieces of paper. Sixteen samples of every binder were prepared and eight of them were stored directly under the laboratory lamp whereas the other eight were stored in the dark (covered by a wooden box). The measurements were implemented after 0, 3, 5, 10 and 15 days. Table 3 shows the binders and their respective ageing states used in this study.

Table 3: Overview of implemented preliminary test of all three binders

Binder	Unaged	RTFOT	PAV	VBA
B287	✓	✓	✓	✓
B504	✓	✘	✓	✘
B637	✓	✘	✓	✘

3.3.2. Correlation between IR and DSR

In this study two unaged binders from different sources (B287A and B637A) were selected. Thirty-six samples of each were prepared in standardized silicon DSR forms (see Figure 23). Half of them were placed in a box, to prevent light contamination, the other half were stored directly under the light of the laboratory lamp, which is shown in Figure 24. The scheme in Figure 25 summarizes how many samples were stored in light or dark and how many of them were measured with IR and DSR. The measurements were implemented on 6 different days in the time span from zero to eighteen days. For the IR analysis two samples per day and for the DSR analysis one sample per day was prepared.

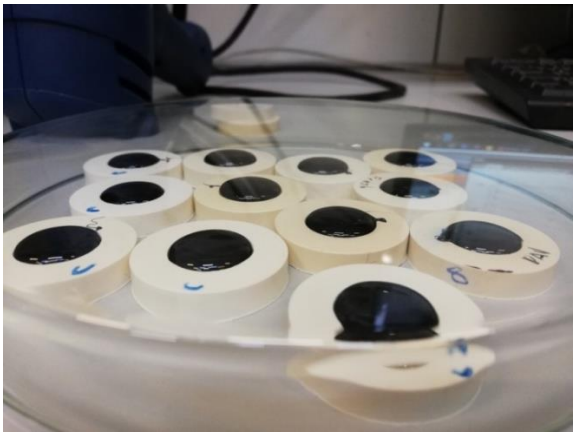

Figure 24: Storage of the samples in light

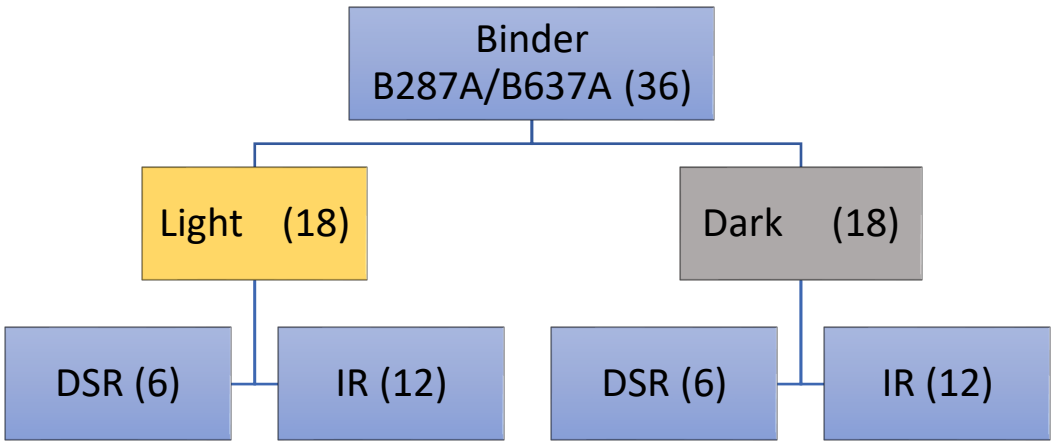

Figure 25: Scheme of sample preparation

The IR spectra of each sample were implemented as described in chapter 3.2.1 and the used spectroscopic instrument was a Perkin-Elmer Spectrum Two in ATR-mode (see Figure 26). The DSR measurements were implemented by mounting the samples on the device and measure them

according to the EN 14770 [41].For the measurements a MCR 302 Anton Paar DSR (see Figure 26) was used and the measurements were implemented on day 0, 1, 3, 7, 11 and 18. Eight different temperatures (40 °C to 82 °C in 6 °C steps) and a frequency sweep from 0.1 – 40 Hz were chosen as parameters. For visualization purposes (to be able to see even small changes in the material), the dynamic modulus and phase angle of 46 °C and 1.6 Hz are plotted as $|G^*|_{Dayi}/|G^*|_{Day1}$ and $\delta_{Dayi} - \delta_{Day1}$ versus time (storage duration in days) which will be called ageing index $AI_{|G^*|}$ and AI_{δ}.

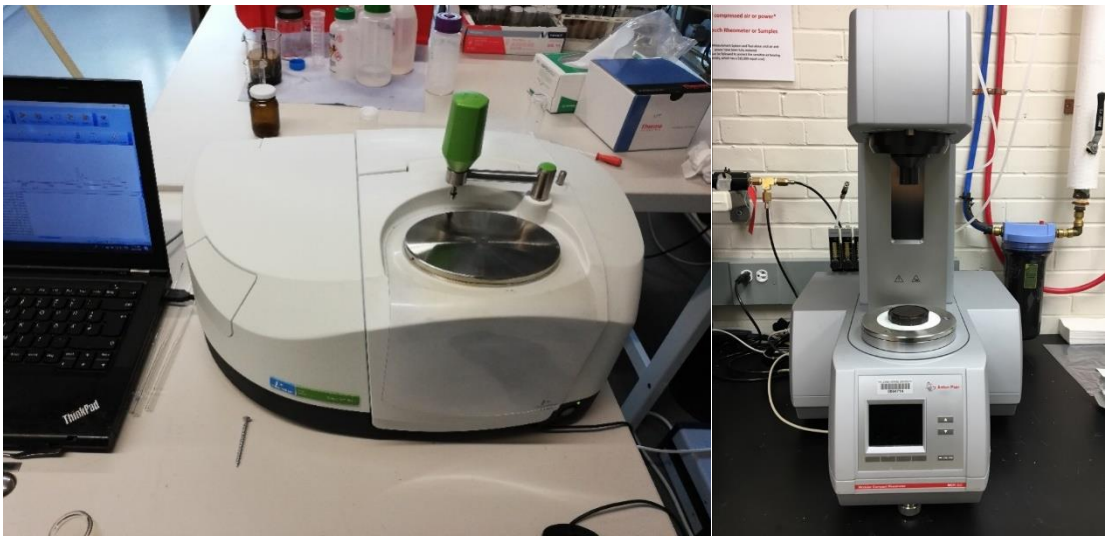

Figure 26: Perkin Elmer Spectrum Two (left) and MCR 302 Anton Paar DSR (right)

3.4. Other Experiments

3.4.1. Comparison of Two Different IR-Devices

For this experiment 8 samples of binder B287 in two different ageing states (unaged and PAV-aged) were prepared. Eight of those samples (4 unaged and 4 aged) were measured with the Perkin-Elmer Spectrum Two spectrometer the remaining eight with the Bruker Vertex v80 device. The results are given in chapter 4.3.4 and a thorough comparison on qualitative and quantitative differences in the spectra but also advantages and disadvantages in handling and the whole measurement procedure of both instruments will be presented.

3.4.2. Variable Asphaltene Content

For this trial, the maltene fraction of binder B637A was dissolved in DCM and purged into three pre-weighed vials. After that, the DCM was evaporated and the remaining maltenes were weighed. 10 wt. % and 20 wt. % of asphaltenes were added to two of those vials, whereas no asphaltenes were added to the third vial. Afterwards, all three samples were dissolved in DCM, stirred thoroughly, dried and finally measured with FTIR spectroscopy. The masses and mass percentages of the samples are given in Table 4.

Table 4: Preparation of binders with different asphaltene content

Vial	$m_{Maltenes}$ (mg)	$m_{Asphaltenes}$ (mg)	wt. % $_{(Maltenes)}$ (%)
1	29.6	0	100
2	28.9	3.2	90
3	30.5	7.6	80

3.4.3. Light-induced ageing of the SAR Fractions

These test runs were expansions of the time dependent studies on bitumen by looking at the time dependency of each fraction. For that, the saturates, aromatics and resins (SAR) fractions of binder B637A were dissolved in DCM, split into six vials each and finally dried. After that, nine of those vials were stored directly under the light of the laboratory lamp whereas the other nine samples were stored in the dark (similar to chapter 3.3). The FTIR measurements were implemented after 1, 7 and 21 days.

3.4.4. Influence of Storage in the Dark on the Aromatic and Maltene Fractions

For this experiment the aromatic and maltene fraction of binder B287A were used. The samples were measured directly after the Fast SARA separation with FTIR and afterwards split into two, respectively. All four samples were stored in the dark and were finally measured again with FTIR after four weeks.

3.4.5. Oxidation of Different Fraction in a Toluene Solution

The saturates, aromatics and resins fractions of binder B287A were selected for this experiment. Each fraction was put on the diamond crystal of the ATR-unit and measured subsequently. After that, they were dissolved directly on the crystal in 50 µl toluene and dried with a stream of air. After the solvent was completely evaporated, another FTIR spectrum was measured. This procedure was repeated a 10 times and the resulting IR spectra are given in chapter 4.3.7 and discussed thoroughly in chapter 5.3.

4. Results and Discussion

4.1. Time Dependent Studies

4.1.1 Preliminary Studies

Preliminary studies were implemented as outlined in chapter 3.3.1 with different binders and at various ageing states. Representative for all studies the IR spectra of the unaged binders B504A and B637A after 0, 3, 5, 10 and 15 days of storage in the light are shown in Figure 27.

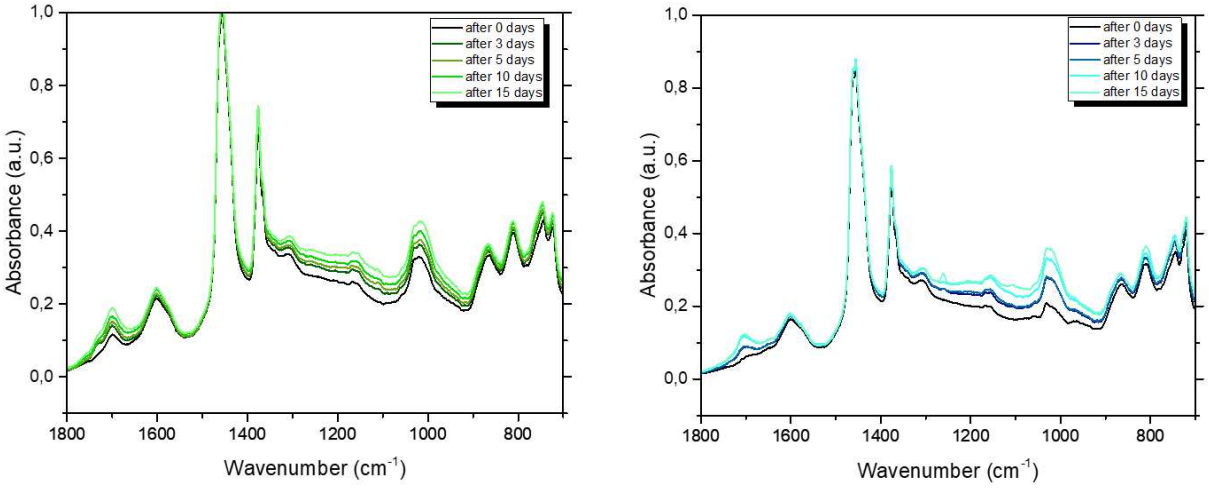

Figure 27: Obtained IR spectra of the unaged binders B504A (left) and B637A (right) after various days stored in the light

The observable trend indicates that a change of storing or handling parameters can have great influence on the desired spectra. After getting the same tendencies for two different binders the next interesting question was, if the laboratory aged samples do change as well in enlightened atmosphere. Figure 28 shows the obtained spectra after a few days in light for long term laboratory aged binders B504C and B637C.

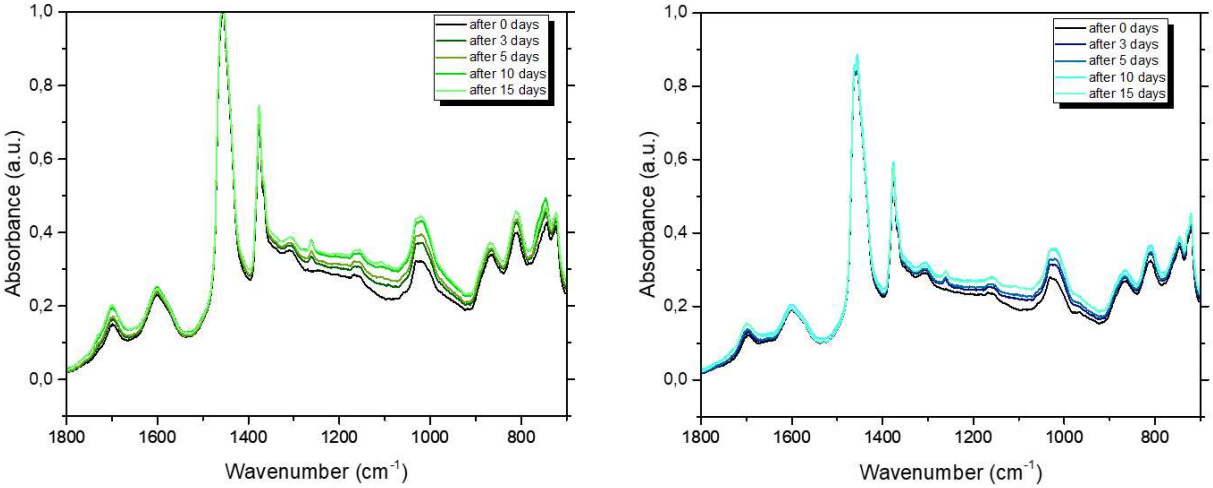

Figure 28: Obtained IR spectra of the PAV aged binders B504C (left) and B637C (right) after various days stored in the light

And again, nevertheless the changes are not as big as in the unaged binders, the aged binder spectra depict also significant alteration during their storage in the light. To obtain more information on where those changes appear in the material (just on the surface or in the whole prepared sample) these studies were further expended by comparing the chemical results obtained with FTIR, to the mechanical behaviour of the binders, measured with DSR in chapter 4.1.2.

4.1.2. FTIR and DSR Analysis

4.1.2.1. FTIR-Analysis

B287A

The IR spectra for this time dependency study of binder B287A are given in Figure 29 and Figure 30. The chosen days of measurement were day 0, 1, 3, 7, 11, 18 and the storage was either in the light (under the laboratory light source) or in the dark. With increasing storage time the bands of the samples stored in light (Figure 29) emerge around 1700 cm^{-1} and as of day 11 a second band at 1735 cm^{-1} arise. Further changes occur from 1340 cm^{-1} to 900 cm^{-1}, where the spectra show higher absorbance the longer they were stored in light. The signals at 1160 and 1030 cm^{-1} grow also and slightly change their shape. For spectra D11L and D18L, a small band emerges at 1110 cm^{-1}.

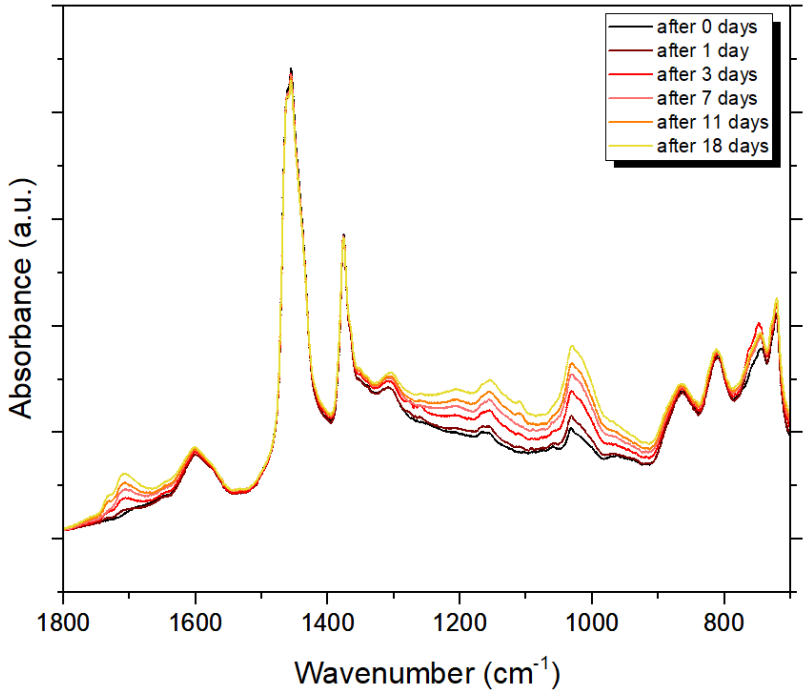

Figure 29: Time dependent changes of binder B287A stored in light

For the samples stored in the dark, hardly anything changes in the spectra. The band at 1030 cm^{-1} increases slightly and two weak signals at 1735 and 1110 cm^{-1} appear.

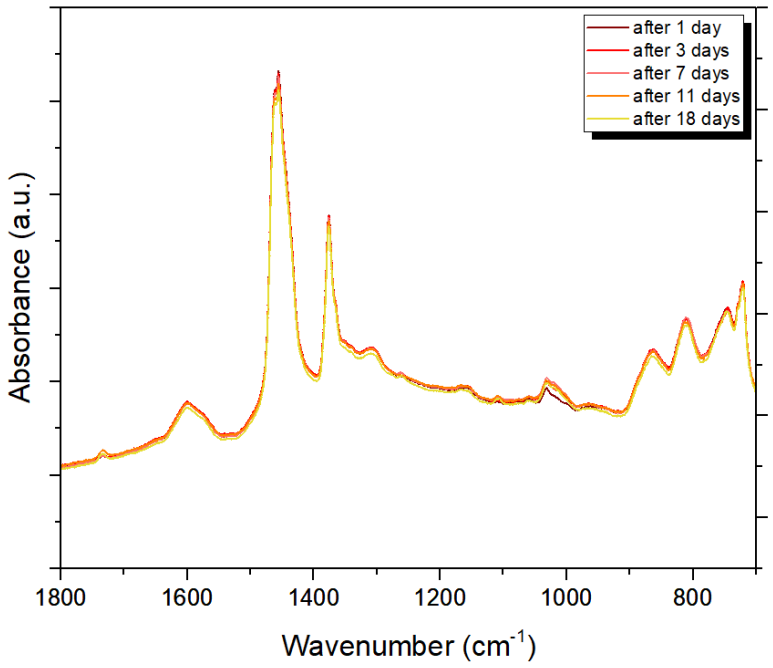

Figure 30: Time dependent changes of binder B287A stored in the dark

By plotting the ageing indices against time, the plots of Figure 31 are obtained. Both ageing indices grow strongly for the samples stored in light, whereas the values for the dark samples just increase slightly.

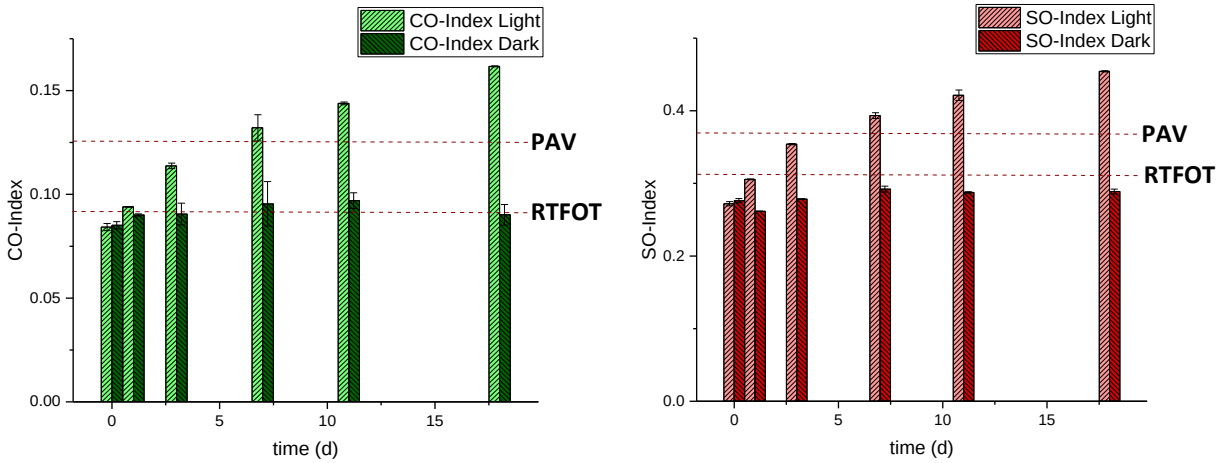

Figure 31: CO-, and SO-Index of the B287A samples stored in the light and in the dark

Another information received from this figure is that the oxidation rate decreases with time. Finally, the ageing values of the RTFOT and PAV aged binders are also indicated as red dashed lines in Figure 31. After one day, the values of RTFOT aged samples and after seven days the values of RTFOT+PAV aged samples were reached in the samples stored in light.

B637A

The measured spectra for the samples of binder B637A are depicted in Figure 32 and Figure 33. The same tendencies are observed for binder B637A with increasing bands at 1700 cm^{-1} and 1030 cm^{-1} and an absorbance shift in the middle region of the spectra (1350-900 cm^{-1}). What is different to binder B287A is that no shoulder at 1735 cm^{-1} and no signal at 1110 cm^{-1} emerges. Another difference regarding the spectral changes is observable after day 3, where the band at 1260 cm^{-1} appears and the bands 810 cm^{-1} increase slightly. Those last mentioned changes are also observable

in the samples stored in the dark with an additional absorbance shift in the region between 1110 and 1070 cm^{-1} (see Figure 33).

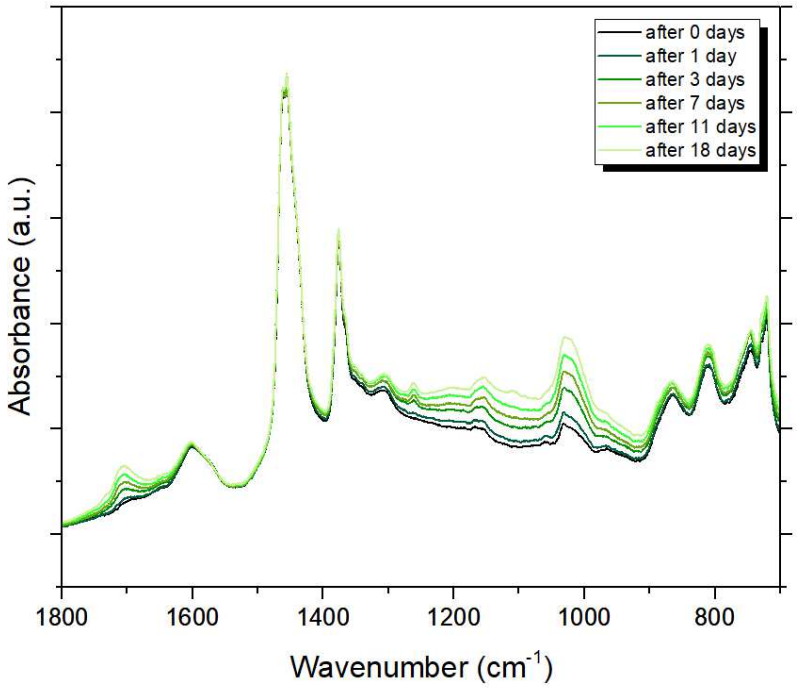

Figure 32: Time dependent changes of binder B637A stored in light

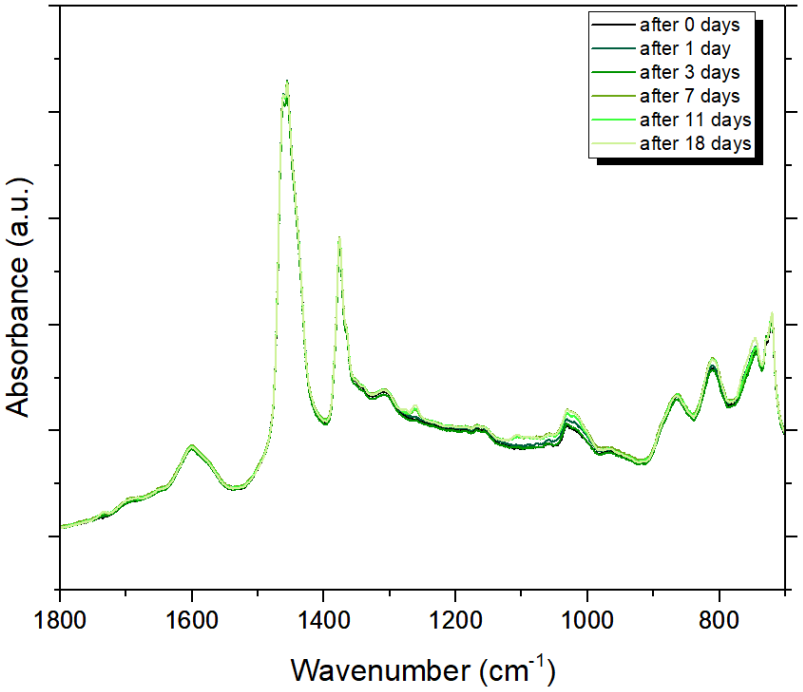

Figure 33: Time dependent changes of binder B637A stored in the dark

As implemented before, the carbonyl- and sulfoxide indices were calculated and are plotted as functions of time in Figure 34.

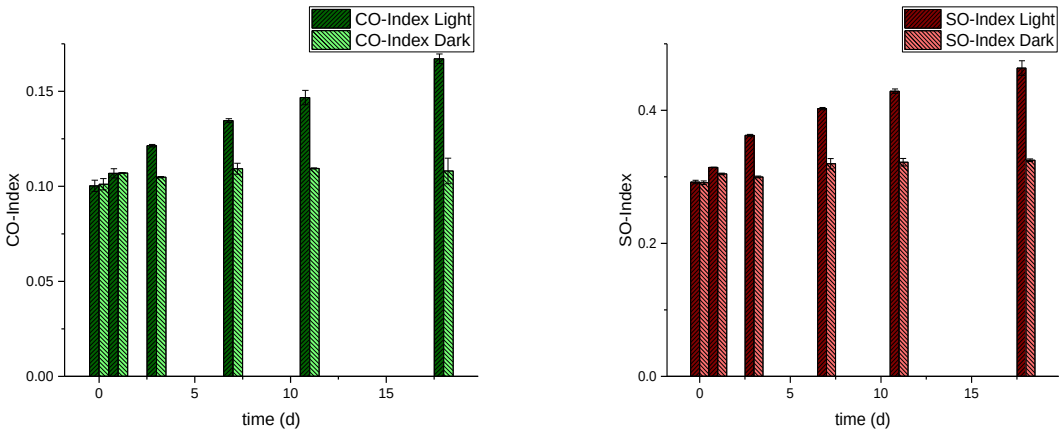

Figure 34: CO-, and SO-Index of the B637A samples stored in the light and in the dark

4.1.2.2. DSR-Analysis

The DSR data obtained for both binders show similar tendencies in the ageing progress as a function of the storage time. Figure 35 shows the dependency of both ageing indices $AI_{|G^*|}$ (left) and AI_{δ} (right) of time (days) for the light- and dark-stored samples of binder B287A (=Binder A) and binder B637A (=Binder B). The ageing index $AI_{|G^*|}$ increases for all measured samples with time, whereas AI_{δ} decreases the longer the samples are stored. The complex modulus of the samples stored in the dark is increasing 11 % (B287A) and 28 % (B637) from day one to day 20. The maximum increases of the samples stored in the light are 24 % (B287A) and 29 % (B637). However, comparing the highest complex modulus values of each binder (in both cases the sample stored in light after 20 days) to the values of laboratory aged (RTFOT) samples they still account for less than one-half of those. The obtained values and the reference values are given in Table 5.

Table 5: Maximum values of $AI_{|G^*|}$ and the relative increase from $AI_{|G^*|,min}$ to $AI_{|G^*|,max}$

Sample		$AI_{\|G^*\|,max}$ (-)	$\Delta(AI_{\|G^*\|,max} - AI_{\|G^*\|,min})/ AI_{\|G^*\|,min}$ (-)
B287A	Light	1.3	0.24
	Dark	1.1	0.11
B287B	RTFOT	3.4	-
B637A	Light	1.4	0.29
	Dark	1.3	0.28
B637B	RTFOT	2.9	-

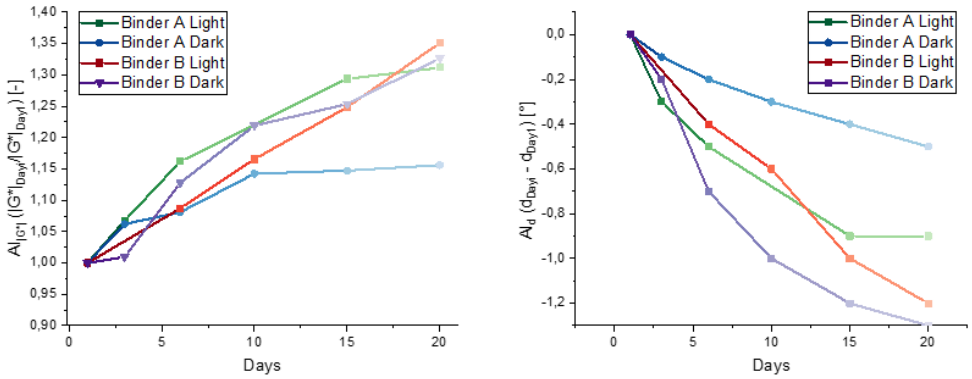

Figure 35: Ageing Indices $AI_{|G^*|}$ (left) and AI_{δ} (right) of both binders stored in light and in the dark at 46 °C and 1.6 Hz

4.2. Gravimetric Analysis

In the beginning of the gravimetric analysis the three unaged binder B287A, B504A and B637A are going to be compared. After that, the results of each binder in all implemented ageing procedures are shown and described in separate chapters.

4.2.1. Comparison of Three Different Unaged Binders

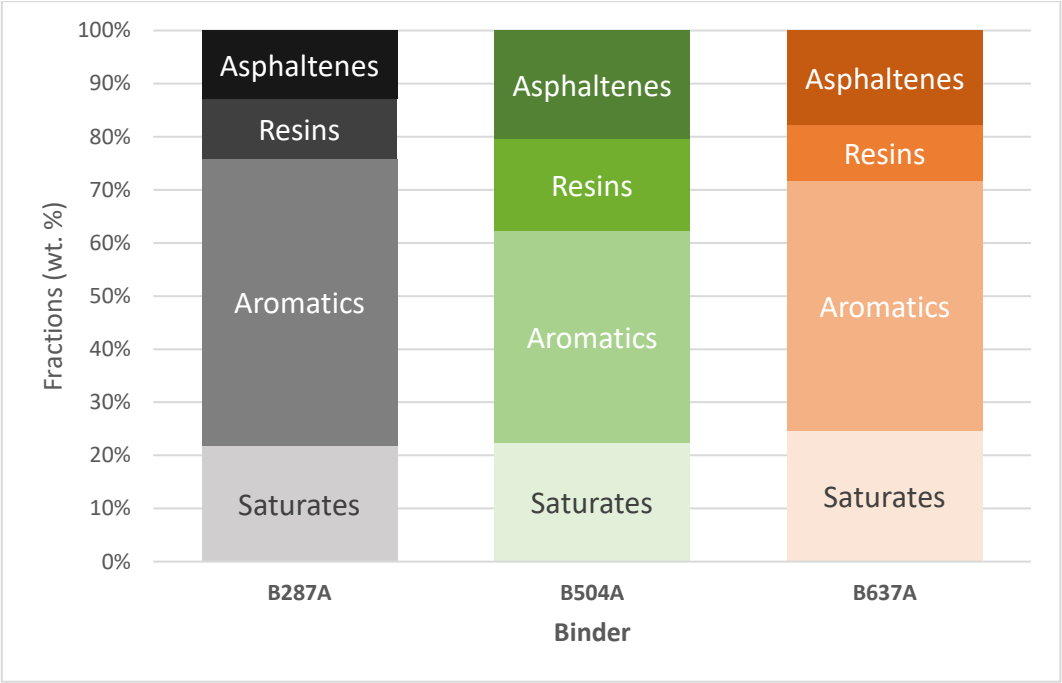

Figure 36: Comparison of the different binders

Figure 36 shows the mass distribution after polarity-based separation of the unaged binders. Besides this graphic another figure containing the average errors is attached in the appendix in Figure 92. Comparison of those binders show that the saturates differ the least from each other, whereas especially binder B504A differentiates strongly in the more polar fractions from the other two binders. As there is a lower content in aromatics measured, the resins and asphaltenes content has to rise. Furthermore, comparing binder B637A to binder B287A, a slightly higher amount of saturates and asphaltenes is measured, while the aromatics are significantly lower (7 wt.%) and the resins are very similar. The obtained mass percentages of the fractions are summarized in Table 6.

Table 6: Mass distribution of the fractions of the three binders

Binder	Saturates [%]	Aromatics [%]	Resins [%]	Asphaltenes [%]
B287A	22	54	11	13
B504A	22	40	17	21
B637A	25	47	10	18

4.2.2. B287

The gravimetric results for binder B287 are shown in Figure 37. The mass percentages of the different fractions are plotted against the ageing state ranging from unaged to field aged. Each fraction got a different color code, which is shown in the legend. As binder B287 was the only binder,

where a field aged binder was available, it was used to validate various ageing methods and is therefore more investigated and discussed.

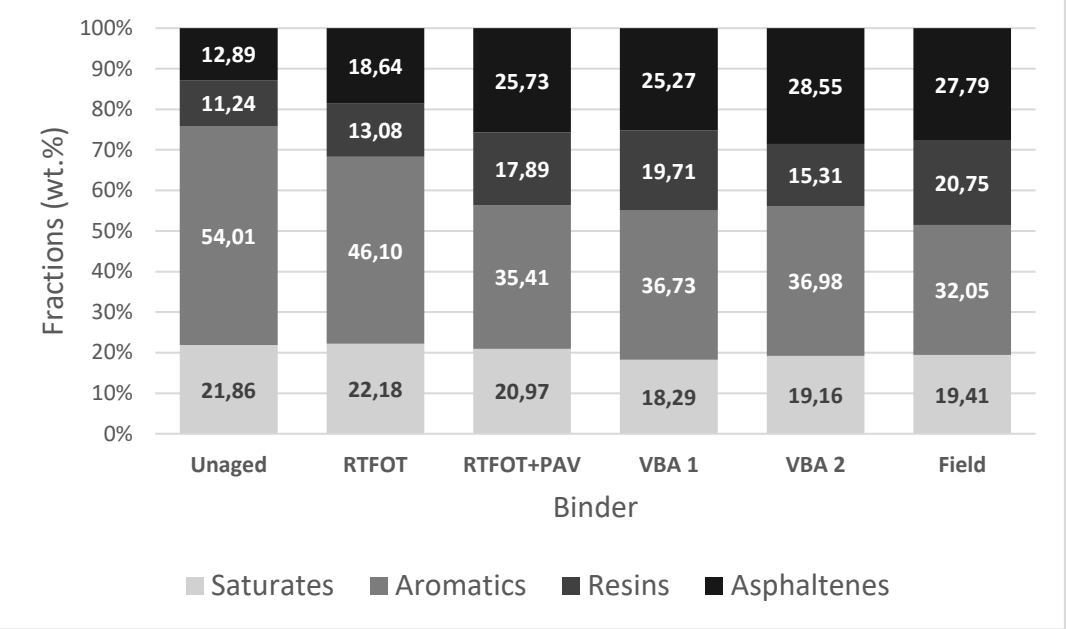

Figure 37: Results from the polarity based chromatographic separation at different levels of lab ageing and field ageing (B287)

By looking at the unaged samples in Figure 37, one can see that the aromatics have the highest mass content of all the fractions. As ageing is applied, this content decreases very strongly and a maximal mass loss of 22 wt.% is obtained for the 5 years field aged sample. The mass losses of the aromatics is are different for all ageing methods and increase in the following order: RTFOT<VBA<PAV<Field. Particularly the comparison of the two laboratory long-term ageing methods (PAV and VBA) is going to be discussed in detail in chapter 5.2. The increase in asphaltenes is significant, reaching its maximum of 15 wt.% for the field aged sample. The resins content increases as well with ageing, reaching a maximum increase of 10 wt.% during field ageing. A discussion of the distribution of masses, especially the resins and asphaltenes, is a topic of great concern and will follow in the later chapters.

Furthermore, the saturates remain unchanged during the common laboratory ageing methods such as RTFOT and PAV, whereas a mass loss under field ageing conditions is measured. The VBA ageing method simulates long term ageing fairly well, considering the saturates solely. A loss of 3-4 wt.% in saturates is observed for the VBA and Field aged sample. To understand this difference between the laboratory ageing simulations one can look at the differences of their general distribution and compare them to the distribution of the field aged sample. Finally, the fractions can be categorized into increasing (resins and asphaltenes) and decreasing (saturates and aromatics) fractions considering their mass percentages. Table 7 gives the sum of mass percentages of those matching pairs for all ageing states.

Table 7: Overall change in mass content of saturates + aromatics and resins + asphaltenes of all separated binders B287

Binder	Saturates + Aromatics [%]	Resins + Asphaltenes [%]
Unaged	76	24
RTFOT+PAV	56	44
VBA 1 (3 days)	55	45

VBA 2 (9 days)	56	44
Field (5 years)	51	49

4.2.3. B504

The implementation of binder B504 involved the unaged and two long term ageing methods, PAV and VBA. The masses obtained after the separation are given in Figure 38.

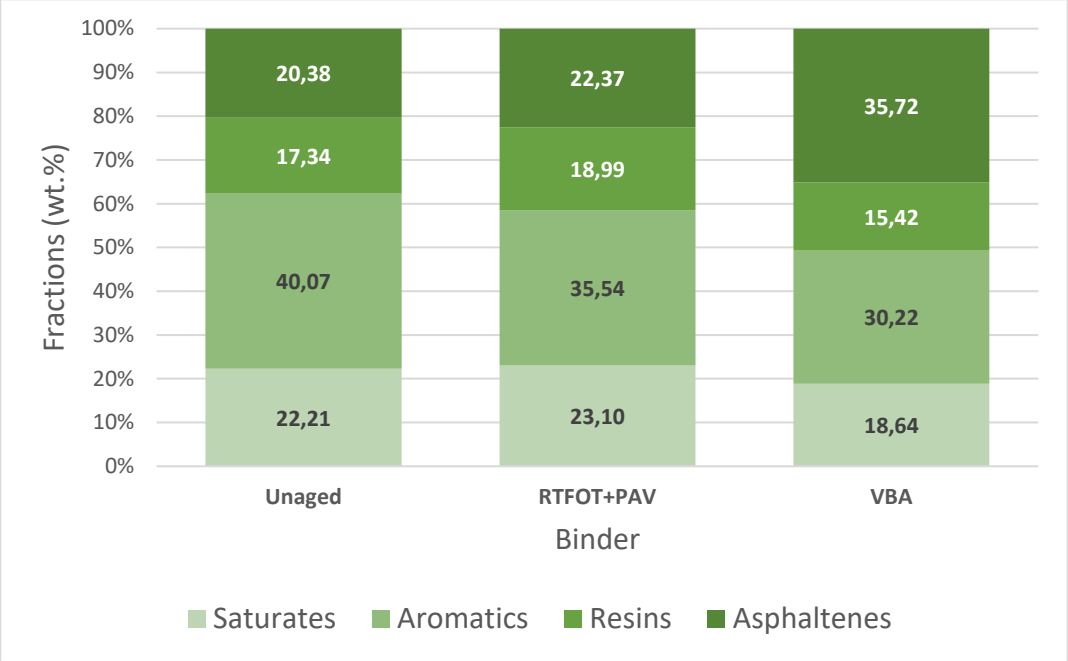

Figure 38: Results from the polarity based chromatographic separation into the SARA fractions for binder B504 and two lab aged samples

As mentioned in the previous chapters, there are significant differences in the mass distribution of binder B504, compared to B287 and B637.The aromatics content of the unaged binder is more than 10 wt.% below the aromatic content of B287A. With ageing, this content decreases even further and a mass loss of roughly 10 wt.% is observed for the VBA aged sample. The saturates do not change during the common long-term ageing, PAV, but decrease significantly during the VBA method, with a mass loss of 4 wt.%. The high mass content in asphaltenes of about 20 wt.% increases further during the applied ageing methods, where a maximum is reached for the VBA aged sample with an increase of 15 wt.%. Finally, the resins are increasing in mass content for the PAV aged sample but do decrease in the VBA aged sample. This rather unintuitive behavior will be a focus in chapter 5.2. The summation of mass percentages of saturates + aromatics and resins + asphaltenes of binder B504 are shown in Table 8:

Table 8: Overall change in mass content of saturates + aromatics and resins + asphaltenes of all separated binders B504

Binder	Saturates + Aromatics [%]	Resins + Asphaltenes [%]
Unaged	62	38
RTFOT+PAV	59	41
VBA (3 days)	49	51

4.2.4. B637

The obtained mass distributions for binder B637 is presented in Figure 39.

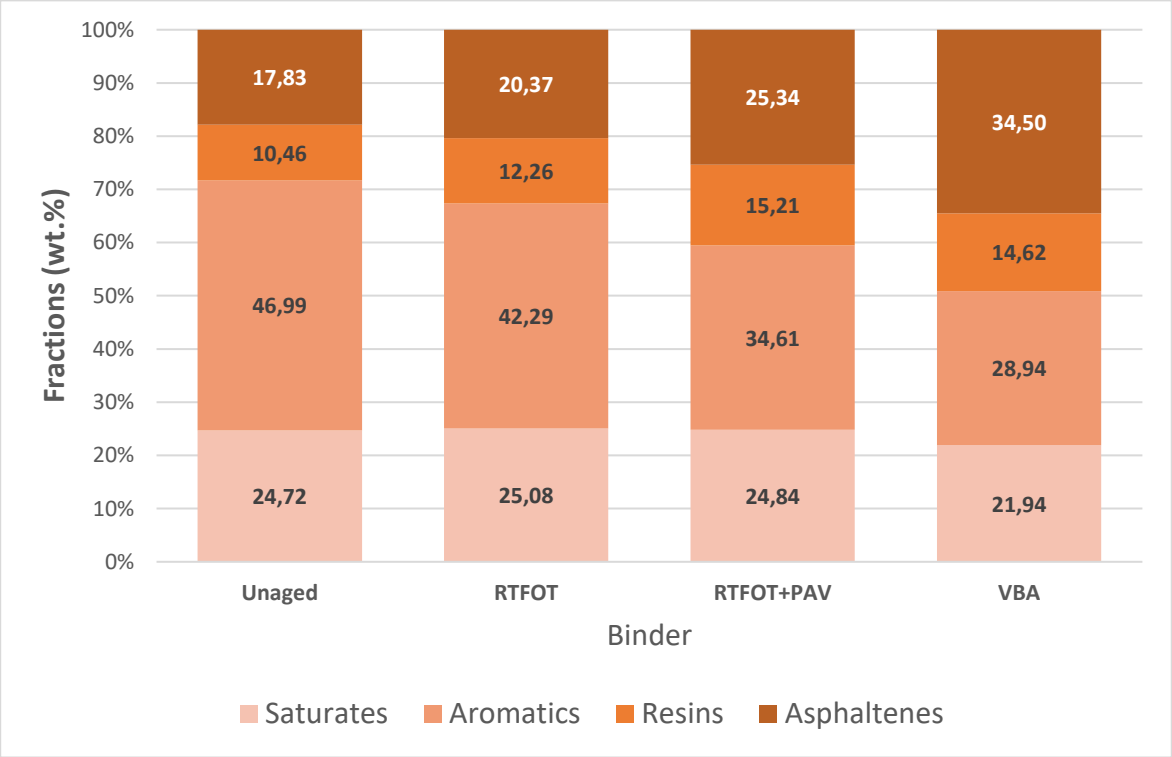

Figure 39: Results from the polarity based chromatographic separation into the SARA fractions for binder B637

The unaged binder contains slightly more saturates and asphaltenes and about 5 wt.% less aromatics compared to binder B287. As the observable trends during the different ageing processes are similar to the binders discussed before, they are not going to be addressed any further in this chapter but is part of the summarizing discussion on gravimetric trends in chapter 5.2. Similar to the other binders the decreasing and increasing fractions are summarized and the results are given in Table 9.

Table 9: Overall change in mass content of saturates + aromatics and resins + asphaltenes of all separated binders B637

Binder	Saturates + Aromatics [%]	Resins + Asphaltenes [%]
Unaged	72	28
RTFOT	67	33
RTFOT+PAV	59	41
VBA (3 days)	51	49

4.3. FTIR Analysis of the SARA Fractions

While the gravimetric results show the shift in polarity within the material, the FTIR spectra of the individual fractions reveal chemical information linked to their changes on the surface upon ageing. The discussion below will regularly reference to functional groups possibly found in bitumen and their assigned bands are listed in Table 10 to Table 13, which were accumulated from various literature sources [33, 34, 43, 44, 45, 46].

Table 10: Table of possible hydrocarbon functional groups found in bitumen and its fractions

Functional Group	Assigned Vibration	Appearing Band (cm^{-1})
Alkyls	ν_{as} CH_2/CH_3	2920
Alkyls	ν_s CH_2/CH_3	2850
Alkyls	δ_{as} CH_2/CH_3	1455
Alkyls	δ_{as} CH_2/CH_3	1380
Alkyls	ρ (CH_{2n})	720
Aromatic	ν C=C	1600
Aromatic	γ CH_{arom}	860
Aromatic	γ CH_{arom}	810
Aromatic	γ CH_{arom}	750
Alkene	δ (CH)	960

Table 11: Table of possible carbonyl functional groups found in bitumen and its fractions

Functional Group	Assigned Vibration	Appearing Band (cm^{-1})
Ketone	ν C=O	1700
2-Quinolone	ν C=O	1655
Carboxylic Acid (free)	ν C=O	1730
Carboxylic Acid (dimer)	ν C=O	1706
Anhydride	ν_s C=O	1870-1845
Anhydride	ν_{as} C=O	1800-1775

Table 12: Table of possible sulfur containing functional groups found in bitumen and its fractions

Functional Group	Assigned Vibration	Appearing Band (cm^{-1})
Sulfoxides	ν S=O	1030
Sulfones	ν SO_2 (out-of-phase)	1310
Sulfones	ν SO_2 (in-phase)	1160
Sulfate Ester	ν_{as} SO_3	1260
Sulfate Ester	ν_s SO_3	1080
Sulfate Ester	ν S-O-C	810

Table 13: Table of possible nitrogen containing functional groups found in bitumen and its fractions

Functional Group	Assigned Vibration	Appearing Band (cm^{-1})
2-Quinolone	ν N-H	3410
Nitroalkanes	ν NO_2 (out-of-phase)	1600-1530

Nitroalkanes	v NO_2 (in-phase)	1380-1310
Nitroaromatics	v NO_2 (out-of-phase)	1555-1480
Nitroaromatics	v NO_2 (in-phase)	1357-1318
Pyridine-N-oxides	v NO	1300-1200

4.3.1. Comparison of the Three Binder

The first topic regarding the FTIR results is going to be the comparison of the investigated binders and their polarity fractions. Figure 40 shows the base binder spectra from each unaged sample with the following colour code, which will be kept for this whole section: black for B287A, green for B504A and orange for B637A. Binder B287A and B637A show many similarities over the whole spectrum with slightly higher signals at 1700 cm^{-1} , 1600 cm^{-1} and between 1350-1300 cm^{-1} for binder B637A. Binder B504A differs strongly from the other two. The intensity at 2951 cm^{-1} and in the whole region between 1750-750 cm^{-1} increases in binder B504A. A new band is observable at 1700 cm^{-1} with a small shoulder at 1730 cm^{-1} and the band at 1030 cm^{-1} is significantly higher as well. Band assignments and discussion on differences in chemistry are going to be a major topic in the discussion section in chapter 5.

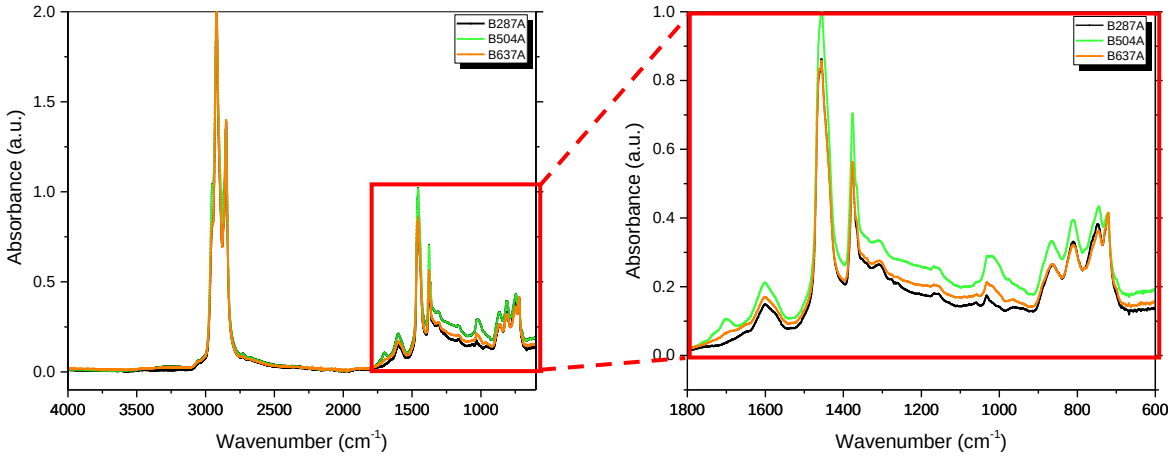

Figure 40: Comparison of the bitumen spectra of the unaged binders

Figure 41 depicts the obtained saturates spectra, which are the starting point of the fraction comparison. There are less bands observable in this fraction. The saturates fractions of all binders contain 6 characteristic bands with high intensities, which are listed in Table 14. Besides those bands, signals at 1310, 1160, 960, 870, 810 and 780 cm^{-1} are found in every fraction but with varying intensities. Especially binder B504A differs from the other two binders (which are indeed very similar), with a higher intensity at 2951 cm^{-1} and an overall intensity shift between 1650 and 750 cm^{-1}.

Table 14: Obtained bands in the saturates spectra and first band assignments

Bands (cm^{-1})	**Assignments**
2951, 2921, 2850	v(-C-H)
1456, 1376	δ(-C-H)
725	ρ((-CH_2-)$_n$)

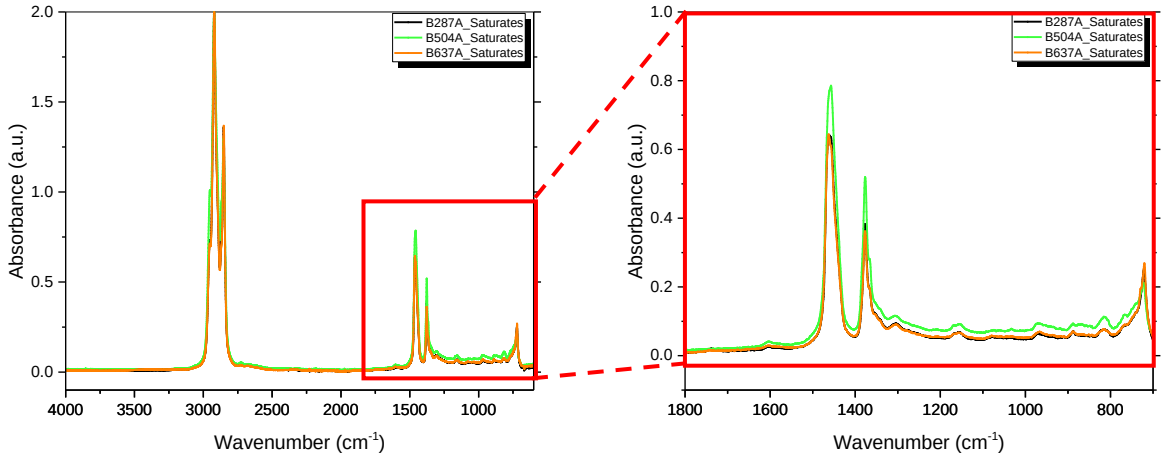

Figure 41: Comparison of the saturates fractions of the unaged binders

Figure 42 shows the aromatics fractions of the unaged bitumen binders. These spectra show signals at 1700cm^{-1} (in Binder B504A and B637A), an intense band at 1600 cm^{-1} and further signals at 1256 and 1030 cm^{-1} in addition to the previously mentioned bands. The overall intensity between 1800 and 800 cm^{-1} increases compared to the saturates fractions and the binder fractions can be ranked: B504A>B637A>B287A regarding the overall intensity in the fingerprint area. Binder B637A differs more from binder B287A as the saturates would have suggested, as an additional signal arises at 1700 cm^{-1}and the intensity between 1350 and 900 cm^{-1} is higher compared to binder B287A.

Table 15: Obtained bands in the aromatics spectra and first band assignments

Bands (cm^{-1})	**Assignments**
1700	ν(C=O)
1600, 860, 810, 780	ν(aromatics), δ(aromatics)
1310, 1100	$\nu_s(SO_2)$, $\nu_{as}(SO_2)$
1256, 1160, 810	ν(sulphate ester), δ(sulphate ester)

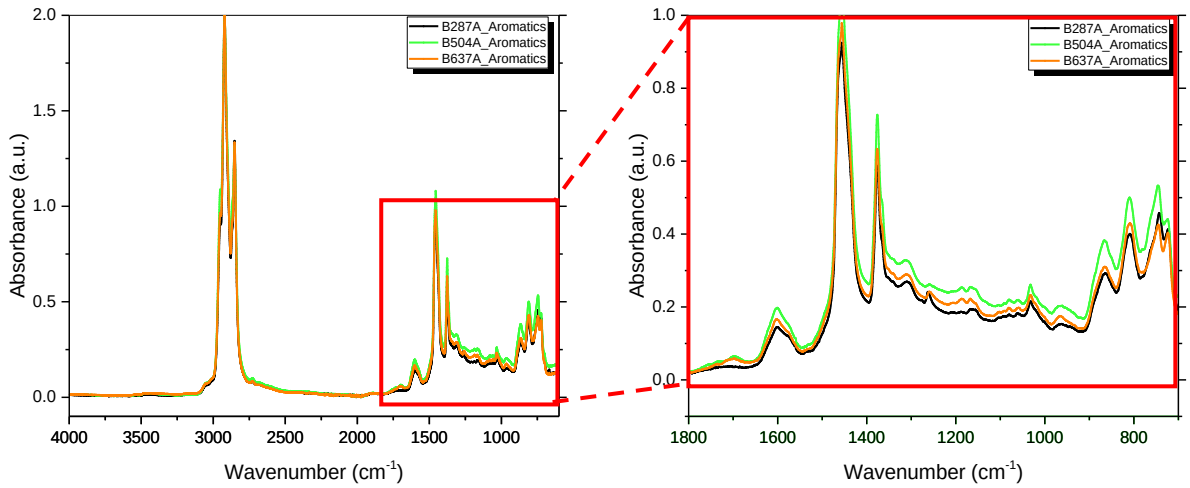

Figure 42: Comparison of the aromatic fractions of the unaged binders

The resin fractions of every bitumen binder are presented in Figure 43. The main differences between the resin spectra and the saturates spectra are observable at 3500-3100 cm^{-1} (a broad band, solely in the resins), signals at 1730 cm^{-1} (B287A and B637A), 1700 cm^{-1} (solely B504A) and 1660 cm^{-1}. A noticeable similarity to the aromatic spectra below 1600 cm^{-1} is observable as bands with very similar wavenumbers appear. However, the intensities of those bands differ strongly from the aromatics and from one binder to the other. Particularly the region between 1800 and 1600 cm^{-1} and the band at 1025 cm^{-1} show major differences to the previous fractions, which will be addressed in chapter 5.3.3 thoroughly. The binders B287A and B637A show again many similarities in regards to the pure number and the positions of the bands but differ in intensities of some bands. Binder B504A differs majorly at the carbonyl region from 1750-1640 cm^{-1}, at 1100 cm^{-1} (where no band is found) and at 1025 cm^{-1} (where the highest intensity of all three binders is found).

Table 16: Obtained bands in the resin spectra and first band assignments

Bands (cm^{-1})	**Assignments**
3500-3100	ν(OH), ν(NH)
1730, 1700, 1660	ν(C=O)
1600, 860, 810, 780	ν(aromatics), δ(aromatics)
1310, 1100	$\nu_s(SO_2)$, $\nu_{as}(SO_2)$
1256, 1160, 810	ν(sulphate ester), δ(sulphate ester)

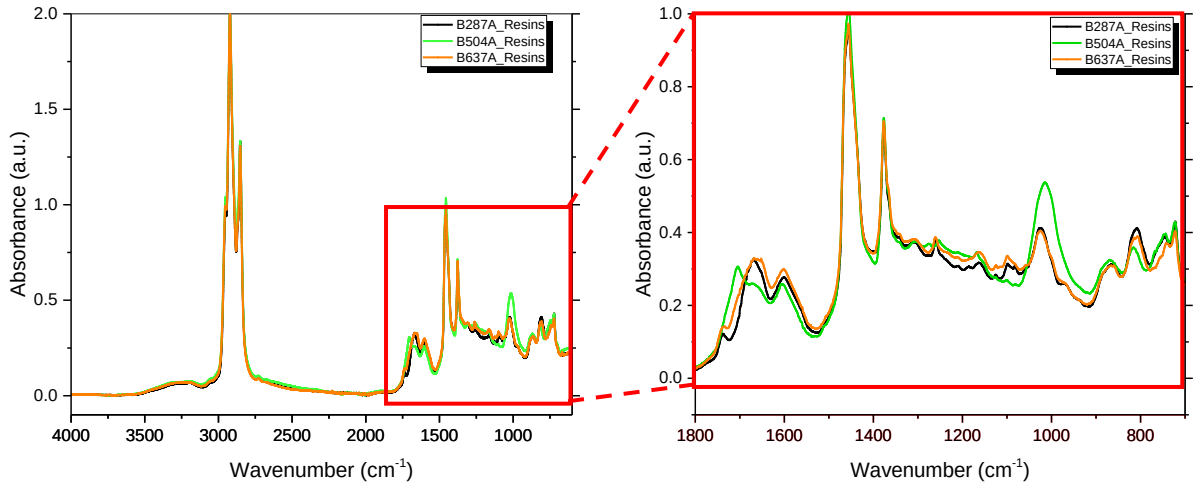

Figure 43: Comparison of the resin fractions of the unaged binders

Finally, the obtained spectra from the asphaltene fractions are shown in Figure 44. The region between 1800 and 700 cm^{-1} is shifting towards higher intensity compared to the previous fractions. However, the overall intensity of the asphaltene-measurements was in fact lower. Due to the fact, that the asphaltenes were obtained as a black powder no complete coverage of the ATR crystal was achievable. This led to air cavities, where IR absorbing gaseous molecules give interfering signals (>3500 cm^{-1} and 2300-2000 cm^{-1}), thus an increasing signal to noise ratio (see chapter 3.2.2). The asphaltene spectra of binder B287A and B637A show small bands (shoulders) at 1730 cm^{-1} and 1660 cm^{-1}, whereas binder B504A has a band at 1700 cm^{-1}. The asphaltenes have high absorption intensities for all samples at 1600 cm^{-1} and many different signals between 1350-700 cm^{-1}. In this region bands at 1310 cm^{-1}, a triple band between 1210 and 1160 cm^{-1} (for binder B287A and B637A)

and bands at 1100, 1030, 960 cm^{-1} (B287A and B637A) appear. And finally, four bands below 900 cm^{-1} are present as well in the asphaltene spectra.

Table 17: Obtained bands in the asphaltene spectra and first band assignments

Bands (cm^{-1})	Assignments
3500-3100	v(OH), v(NH)
1730, 1700	v(C=O)
1600, 860, 810, 780	v(aromatics), δ(aromatics)
1310, 1100	$v_s(SO_2)$, $v_{as}(SO_2)$
1256, 1160, 810	v(sulphate ester), δ(sulphate ester)

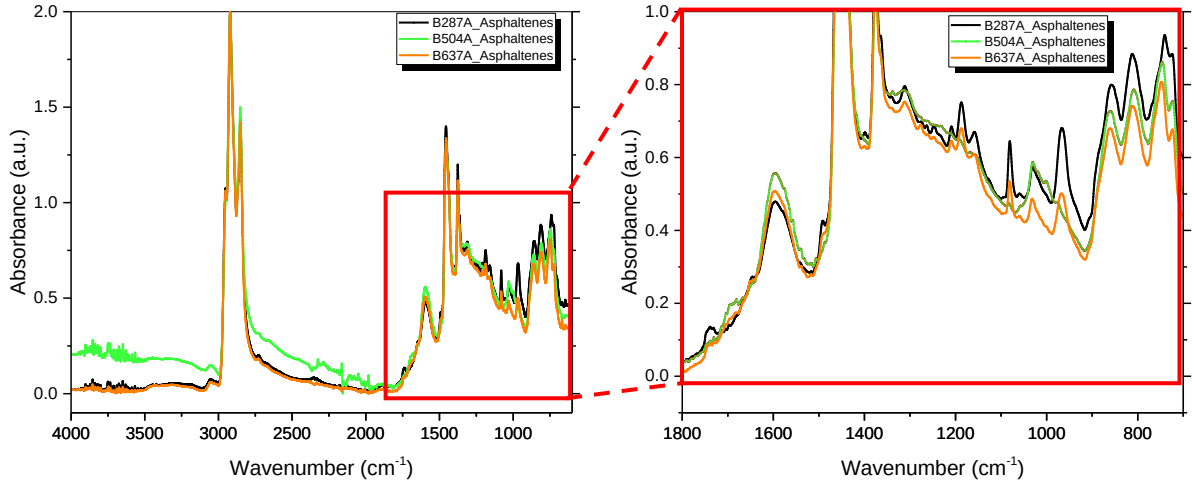

Figure 44: Comparison of the asphaltenes fractions of the unaged binders

4.3.2. Effects of Ageing on the Binders

By looking at the obtained spectra of the polarity fractions from differently aged binder samples, a more detailed ageing behavior and ageing peculiarities are obtainable. This will be the focus of this spectroscopic chapter.

4.3.2.1. B287

Before each separation procedure the base binders were analyzed with FTIR. The results of these measurements are shown in Figure 45. The spectra of the aged bitumen samples have increasing bands at 1700 cm^{-1} and at 1030 cm^{-1}. The overall intensity below 1800 cm^{-1} increases in the following order: B287A<RTFOT<PAV<VBA1<Field≈VBA2.

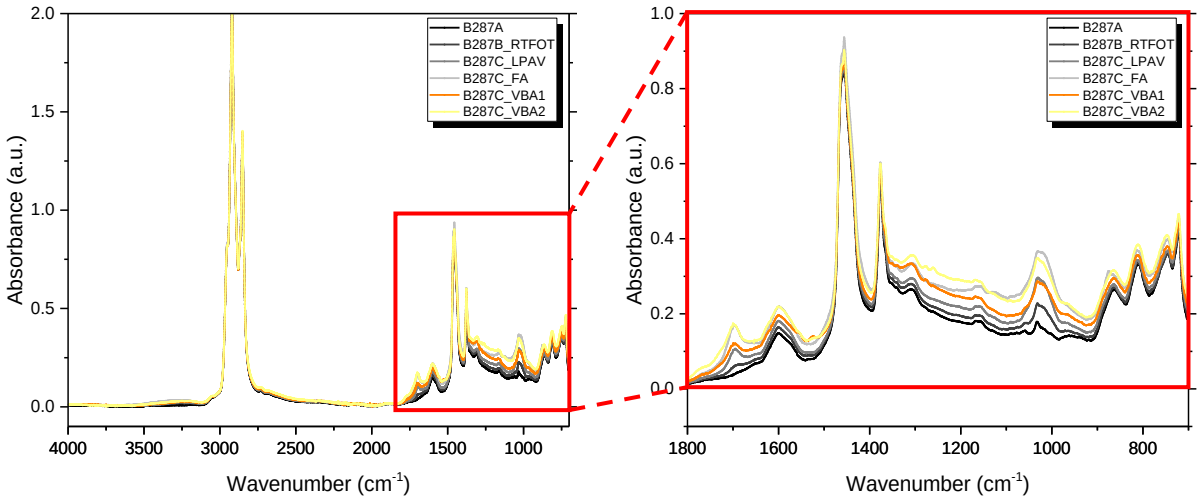

Figure 45: Bitumen spectra of all investigated ageing states of binder B287

The Saturates

The spectra of the saturates fractions of binder B287A are presented in Figure 46. Similar to chapter 4.2.1 six intense bands are observable in these fractions. The exact wavenumbers with possible functional assignments are given in Table 10 and Table 14. Besides those signals, there are signals at 1600, 850 and 810 cm^{-1}, which indicate the presence of small amounts of aromatic functionalities. Further signals are observable at 1310 cm^{-1}, 1160cm^{-1} and 900 cm^{-1} and possible causes for those vibration modes are given in Table 10 and Table 12. Further analysis and explanations on the presence of different chemical functionalities and more precise band assignments are given in the discussion section in chapter 5.3.1.

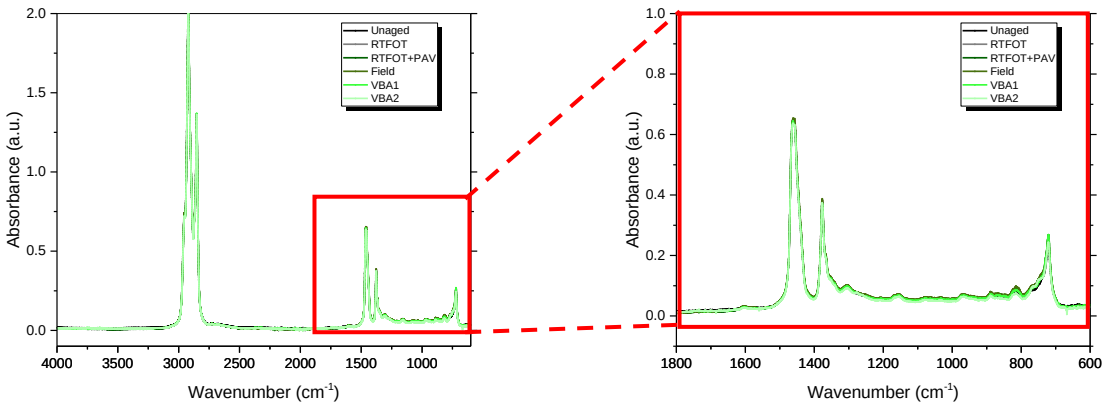

Figure 46: FTIR Spectra (left) and fingerprint cutout (right) of the saturates fractions of binder B287

The Aromatics

Figure 47 shows the FTIR spectra of the aromatic fractions in all ageing states. Most of the appearing bands in these fractions are already defined and described in chapter 4.2.1 as well as given in Table 15. Significant changes are appearing due to ageing. An additional band is appearing at 1700 cm^{-1}, which can be linked to emerging ketones in this fraction. The intensity of this band increases in the following order: Unaged<RTFOT<RTFOT+PAV≈VBA1<VBA2<Field. The intensity gap between the field aged sample and the long-term ageing methods PAV and VBA indicates that the ageing on the field is

still not precisely simulated. By looking farther down the wavenumber scale, a slight increase in intensity at the aromatic signals at 1600 and 810 cm^{-1} and in the whole region between 1310 and 900 cm^{-1} is observable. Furthermore, two additional signals appear solely in the VBA1 aged samples at 1560 and 1525 cm^{-1}. Connections to possible functionalities in those regions will be discussed in chapter 5.3.

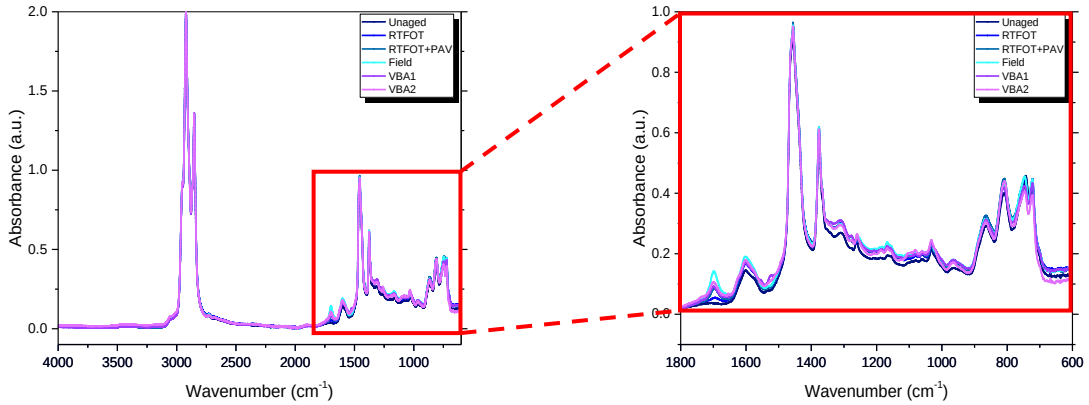

Figure 47: FTIR spectra (left) and fingerprint cutout (right) of the aromatic fractions of binder B287

The Resins

The spectra of the differently aged resin fractions of binder B287 are shown in Figure 48. Two regions of great interest are the carbonyl region, where three signals are found, representing 2-quinolones, carboxylic acids and emerging ketones and the region between 1320 and 1080 cm^{-1}. In this region many bands appear, which can be linked to various functionalities shown in Table 12 and Table 13. Significant changes are also happening at 1025 cm^{-1}, where this intense band increases even further during ageing. The intensity compared to the unaged fraction increases in the following order: RTFOT<VBA1≈Field<RTFOT+PAV<VBA2. Additionally, two bands at 1560 cm^{-1} and 1525 cm^{-1} are observable. But similar to the aromatics fractions they do only appear in the VBA1 aged sample.

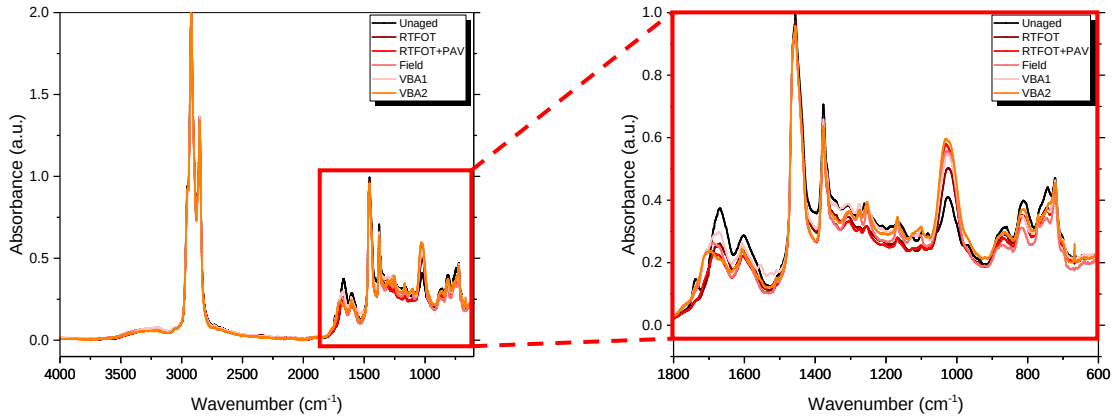

Figure 48: FTIR spectra (left) and fingerprint cutout (right) of the resin fractions of binder B287

The Asphaltenes

Finally, Figure 49 shows the asphaltene spectra in all ageing states of binder B287. Starting from the highest wavenumbers, one can see a slight change upon 3100 cm^{-1} as a very broad band emerges in the asphaltenes of the aged samples. The region below 1800 cm^{-1} has much higher intensity compared to the saturates, aromatics and resins. This fact will be thoroughly discussed in chapters

4.3.3 and 5.3. Going further down the wavenumbers scale, a carbonyl band at 1700 cm^{-1} emerges. The increase in intensity of this band compared to the unaged fraction is indicated by the following order: RTFOT<RTFOT+PAV<VBA2<VBA1≈Field. Furthermore, the intensity of the bands at 1600 cm^{-1} and 1030 cm^{-1} are increasing as well during ageing. In both cases, the field aged sample represents the bands with the highest intensity. Two additional bands that appear solely in the VBA1 aged binders are at 1560 and 1525 cm^{-1}. The region below 1320 cm^{-1} depicts a great variety of different bands and intensity changes due to alteration of the binder. The exact wavenumbers of these bands are given in Table 17 and connections to possible reasons of observable changes are important topics in the discussion in chapter 5.3.4.

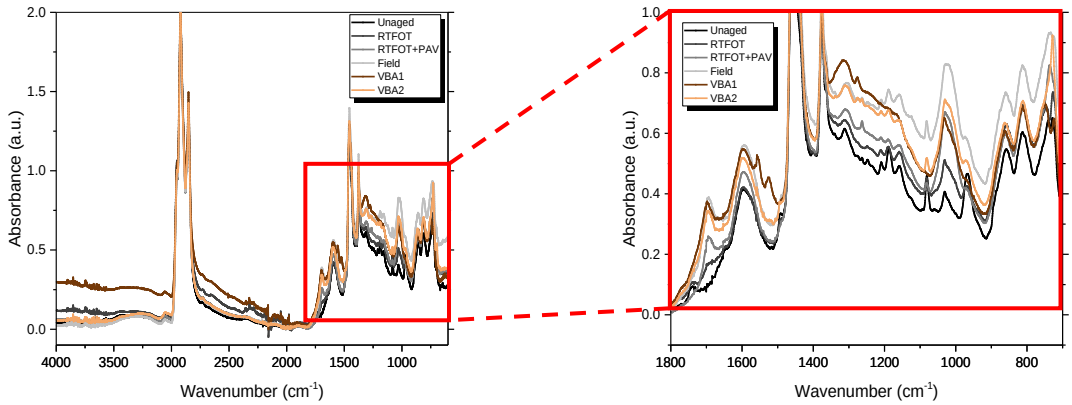

Figure 49: FTIR spectra (left) and fingerprint cutout (right) of the asphaltene fractions of binder B287

Ageing Effects on the Fractions and Binder

In Figure 50 all four fractions in all ageing states are shown in one plot on the left and a cutout of the fingerprint area is highlighted on the right. With increasing polarity, the intensity in the fingerprint area rises consistently but also ageing leads to shifts in the spectral region below 1800 cm^{-1} and especially between 1350 and 1050 cm^{-1}. The shifts due to ageing are observable for the aromatics, resins and asphaltenes but not for the saturates. An important question that comes in mind is whether those shifts happening within one fraction or the molecule migration from lower to higher polarity fractions leads to changes in the resulting polarity fractions. This question and other highly concerning points will be discussed thoroughly in chapter 5.3.

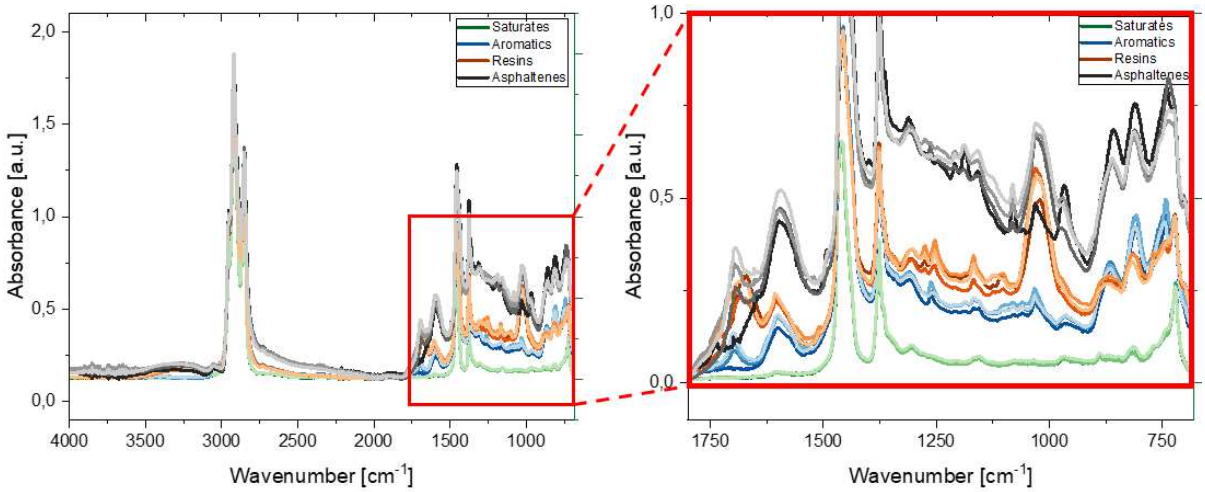

Figure 50: Comparison of all FTIR spectra from the four fractions of binder B287

To track the influence of such changes in specific regions of the spectra they were normalized and the region between 1600 and 1100 cm^{-1} was integrated (see chapter 3.2.2). According to Equation 25) in chapter 3.2.2 representative values are obtained and are given in Table 18.

Table 18: Statistic evaluation of the shift in the fingerprint area between 1600 – 1100 cm^{-1}

Fraction	Fingerprint Shift Area (-)
Unaged Bitumen	17.51 ± 0.14
RTFOT+PAV	19.02 ± 0.10
VBA (9 days)	21.06 ± 0.14
Field (5 years)	21.98 ± 0.34

A more detailed discussion on this table, especially in consideration of the fractional spectra and the gravimetric results is outlined in chapter 5.3.

4.2.2.2. B504

This binder was aged with the laboratory ageing methods RTFOT+PAV and VBA1. The base binder spectra are presented in Figure 51. They show, similar to binder B287A increasing intensity at 1700 cm^{-1} and an intensity shift in the whole region below 1800 cm^{-1}. However, opposed to the results of binder B287A, the band at 1030 cm^{-1} does not change with ageing in these binder spectra.

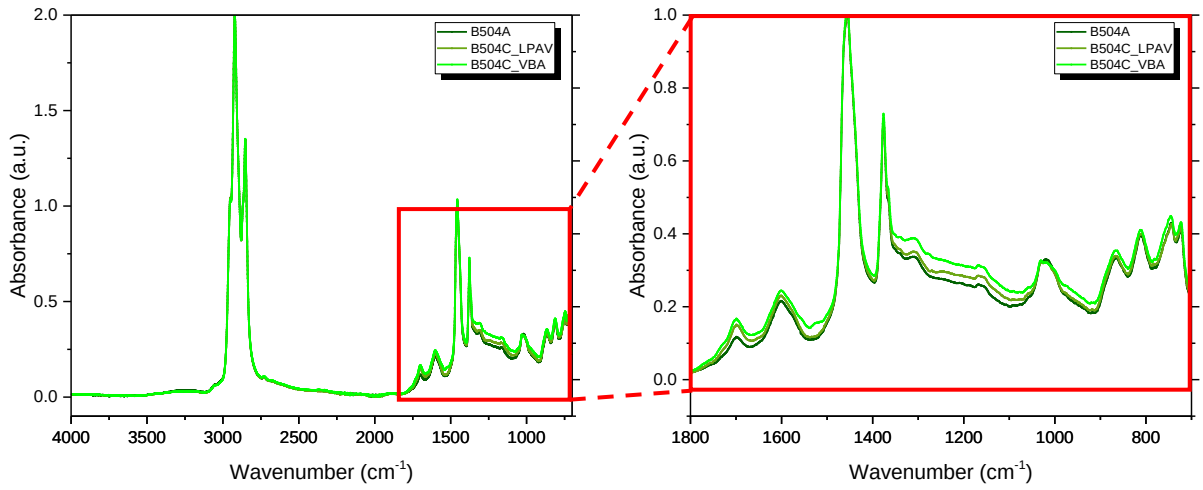

Figure 51: Bitumen spectra of all investigated ageing states of binder B504

The Saturates

The saturates spectra of binder B504 in all ageing states are shown in Figure 52: FTIR spectra (left) and fingerprint cutout (right) of the saturates fractions from all ageing states of binder B504Figure 52. As already mentioned in chapter 4.3.2.1, no changes are observable with ageing in this fraction. The wavenumbers of the appearing bands are also similar to binder B287 and are listed in Table 14.

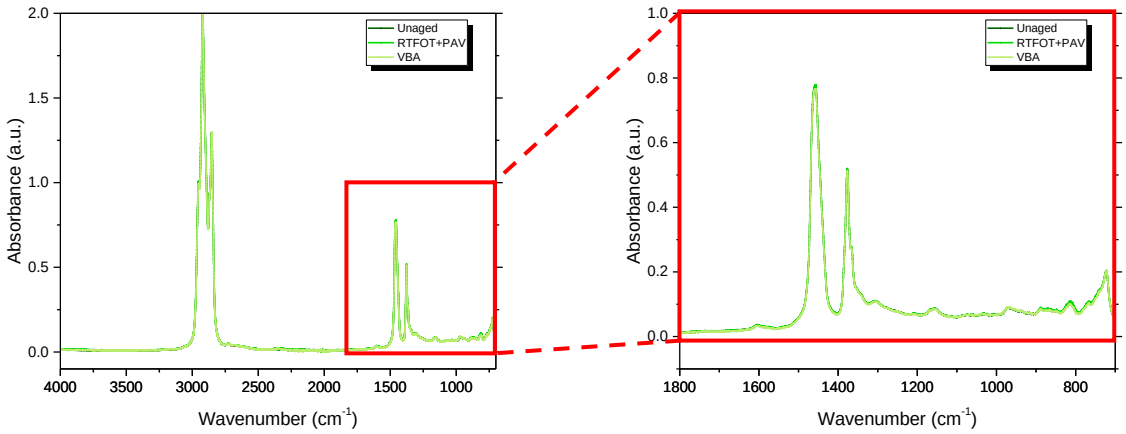

Figure 52: FTIR spectra (left) and fingerprint cutout (right) of the saturates fractions from all ageing states of binder B504

The Aromatics

The aromatic spectra of binder B504 are given in Figure 53. Comparing the bands at 1700 cm^{-1}, both long-term ageing methods show the same intensity increase compared to the unaged aromatics fraction. Differences between those two methods are found at 1600 and 810 cm^{-1} (aromatic signals) as well as two emerging bands at 1560 and 1525 cm^{-1} and a slight growth of the band at 1310 cm^{-1} of the VBA-aged binder.

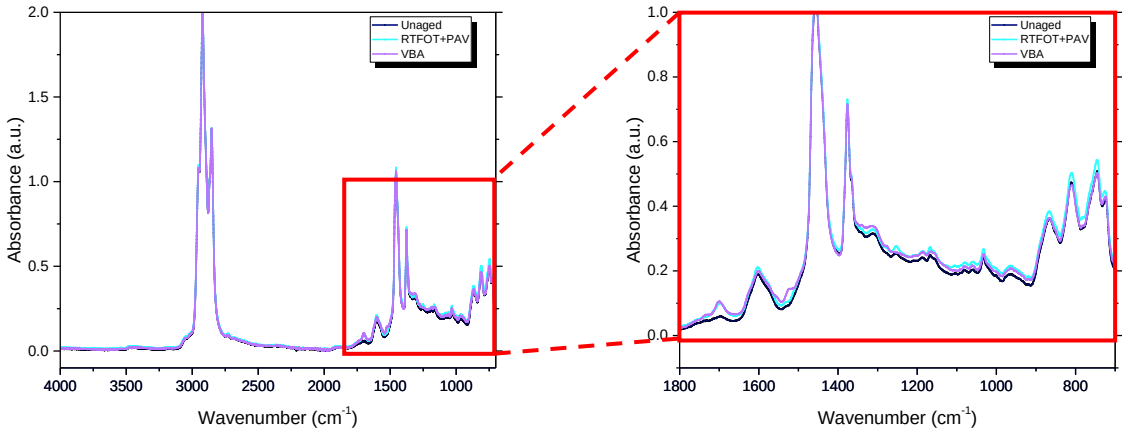

Figure 53: FTIR spectra (left) and fingerprint cutout (right) of the aromatic fractions from all ageing states of binder B504

The Resins

The spectra of the resin fractions are shown in Figure 54. The RTFOT+PAV aged sample gives similar absorbance intensities from 1800 to 1150 cm^{-1} with only slight differences at 1650 and 1260 cm^{-1}. Below those wavenumber regions, the RTFOT+PAV sample intensities are higher at 1100, 1025 and 810 cm^{-1}. In the VBA-aged sample the intensities of the band at 1700 cm^{-1}, between 1600 and 1500 cm^{-1} and the whole region between 1350 and 1080 cm^{-1} increases but remains unchanged at 1030 cm^{-1} compared to the unaged resins.

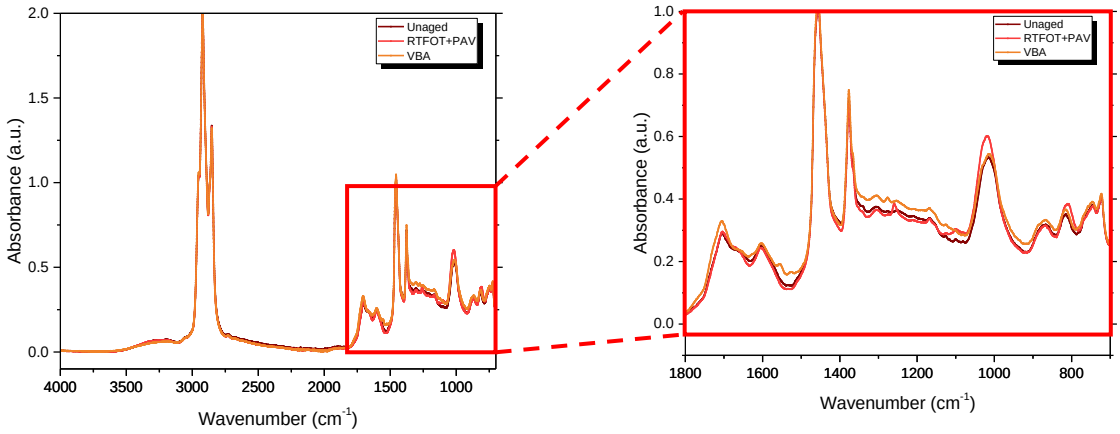

Figure 54: FTIR spectra (left) and fingerprint cutout (right) of the resin fractions from all obtained ageing states (Binder B504)

The Asphaltenes

Finally, Figure 55 depicts the obtained spectra of all asphaltene fractions of binder B504. The standardized laboratory ageing method RTFOT+PAV lead to increases at 1700 cm^{-1} and 1030 cm^{-1}. Besides that, the intensity of the spectrum of this particular ageing state is decreasing at 1310, 830, 810 and 780 cm^{-1}. The VBA aged asphaltene sample spectra contain additional bands at 1560 and 1525 cm^{-1} and an overall shift of intensity between 1350 and 900 cm^{-1} with specific bands at 1310, 1270, 1080 and 1030 cm^{-1}.

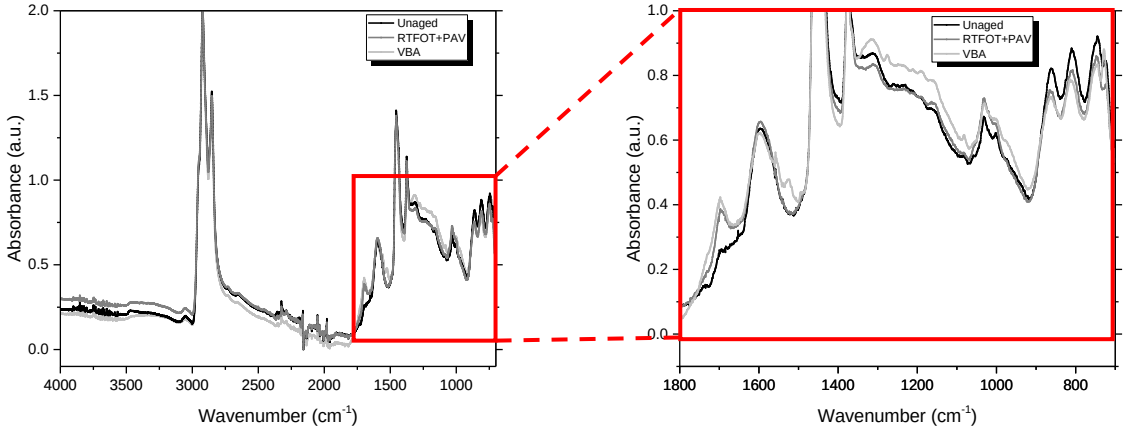

Figure 55: FTIR spectra (left) and fingerprint cutout (right) of the asphaltenes fractions from all ageing states (Binder B504)

4.2.2.3. B637

The FTIR results for binder B637 and its polarity fractions are showing very similar signals and trends upon ageing as binder B287. Figure 56 depicts the bitumen spectra of all different ageing states applied on binder B637. Furthermore, the spectra presented from Figure 57 to Figure 60 show all the obtained fractions of binder B637.

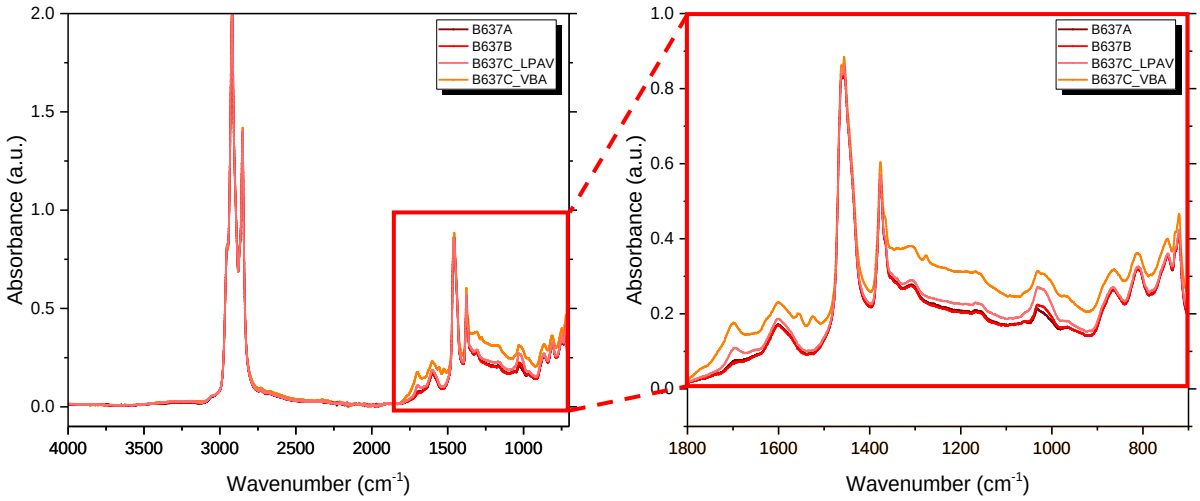

Figure 56: Bitumen spectra of all investigated ageing states of binder B637

The Saturates

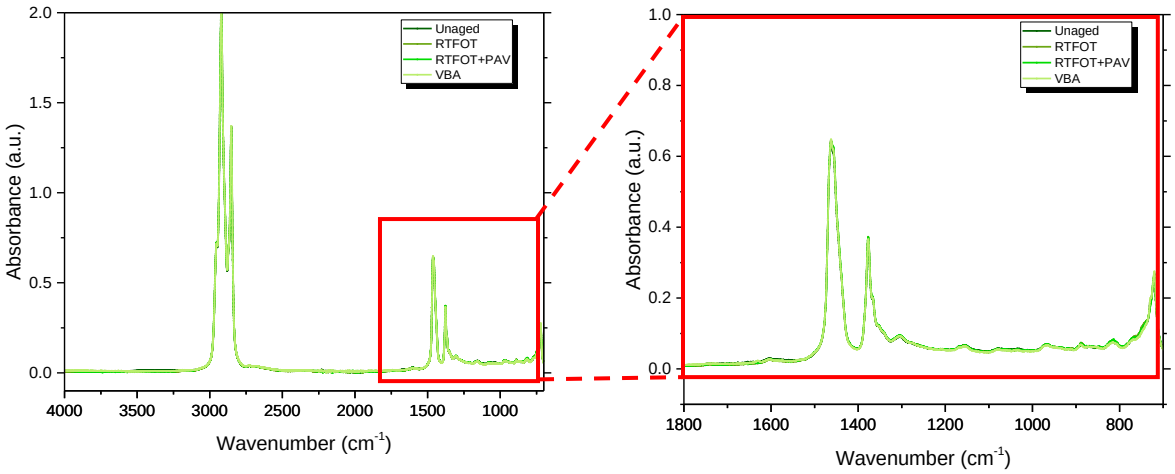

Figure 57: FTIR spectra (left) and fingerprint cutout (right) of the saturates fractions from all ageing states (B637)

The Aromatics

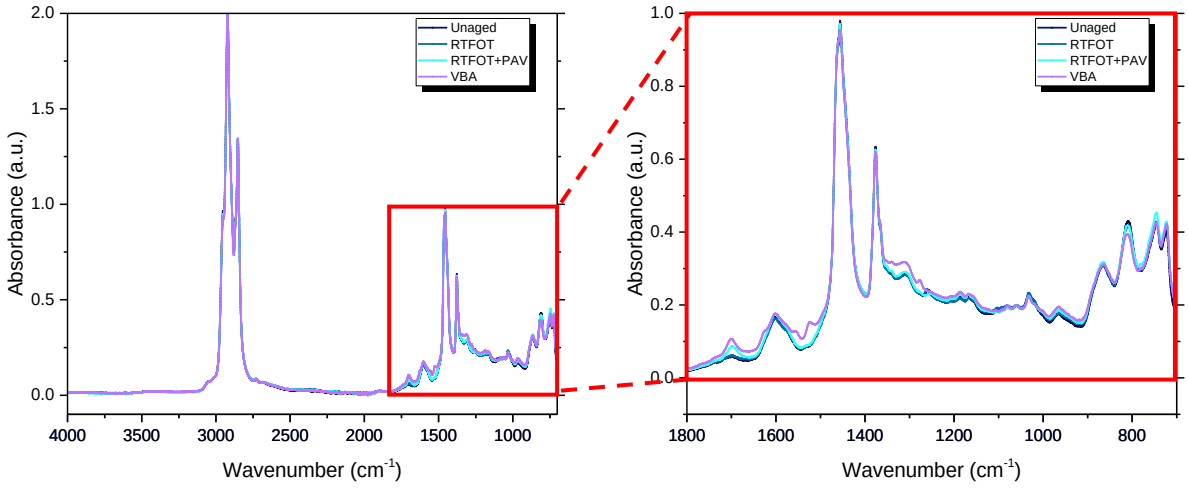

Figure 58: FTIR spectra (left) and fingerprint cutout (right) of the aromatics fractions from all ageing states (B637)

The Resins

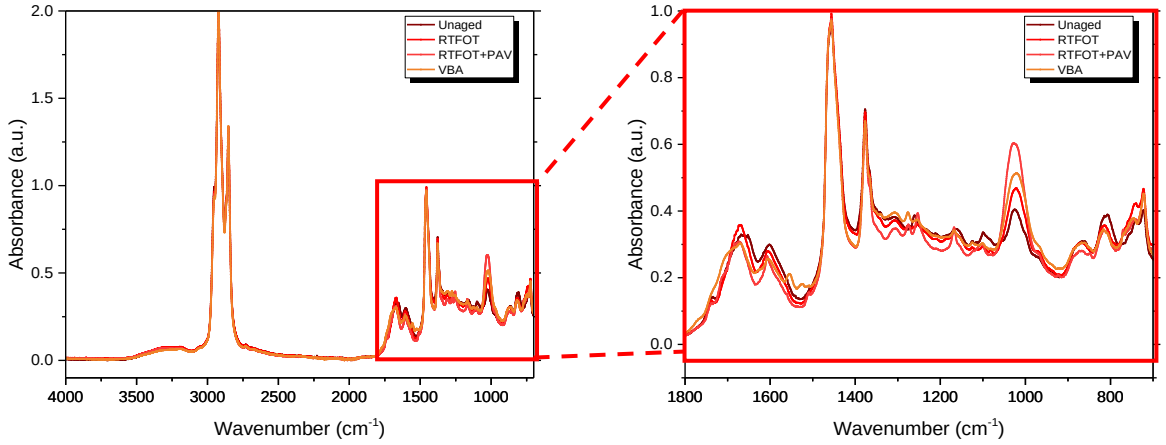

Figure 59: FTIR spectra (left) and fingerprint cutout (right) of the resin fractions from all ageing states (B637)

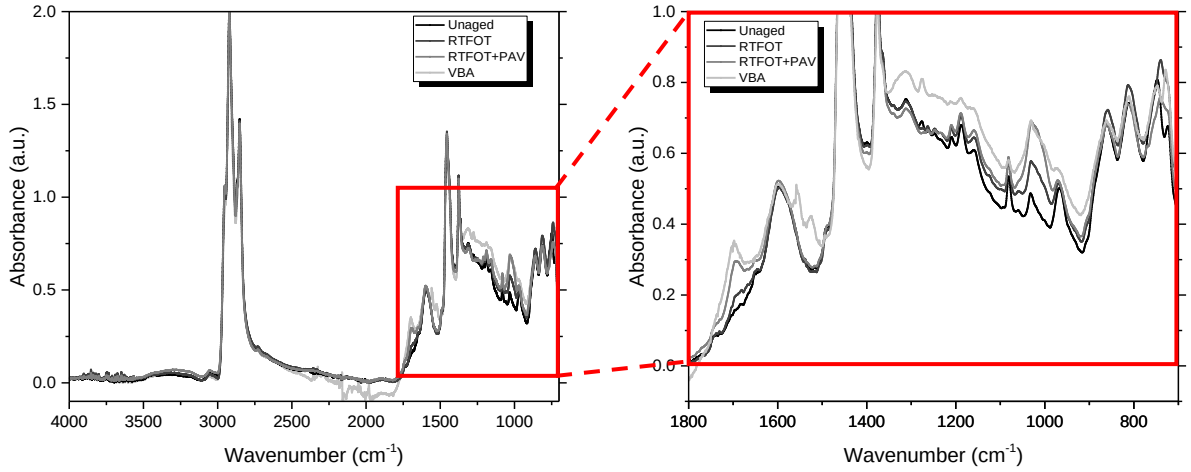

Figure 60: FTIR spectra (left) and fingerprint cutout (right) of the asphaltene fractions from all ageing states (B637)

4.3.3. Influence of Asphaltene Content on the IR Spectrum

The impact on higher asphaltene contents on parts of the spectra below 1700 cm^{-1} are depicted in Figure 61. By adding different amounts of asphaltene to an unaged maltene fraction, the influence of the fraction with the highest polarity on the spectrum, and especially on the infrared region below 1700 cm^{-1}, can be observed. As a result, a general rise in absorbance from 1700 to 680 cm^{-1} with increasing asphaltenes content is observable.

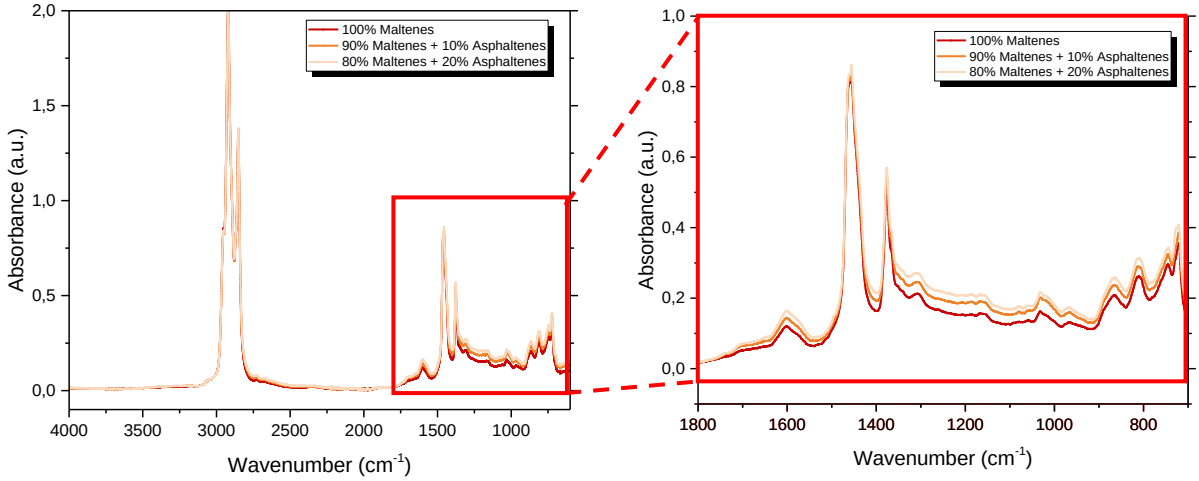

Figure 61: Maltene fraction of B637A with different amounts of added asphaltenes

4.3.4. Comparison of Two Different IR-Spectrometers

To compare the different IR devices unaged and long-term aged bitumen samples of binder B287 were measured and the increase of specific ageing-related bands was monitored. Cut-outs from the obtained spectra are given in Figure 62. The spectra on the left represent the measurements from the Perkin-Elmer Spectrum Two device whereas the spectra on the right in Figure 62 were derived from the Bruker Vertex v80 device. To be able to compare those spectra they were all normalized (Absorbance at 2921 cm^{-1} equals 2.0 a.u.). Significant differences are observable in the region below 1800 cm^{-1}, where the overall intensity of the Bruker device is much lower. To be able to outline the

differences semi-quantitatively, specific regions of the spectra were integrated. Therefore, those integrated regions below 1800 cm^{-1} were related to the signal at 2921 cm^{-1} (the signal with the highest intensity), as commonly done in literature to quantify ageing. The discrepancies of the obtained quantitative values are summarized in Table 19. The significance in regards to the comparability of ageing measurements using different FTIR spectrometer as well as the advantages and disadvantages of each FTIR spectrometer in regards to handling, sampling and overall suitability to bitumen-related tasks are going to be described and thoroughly discussed in chapter 5.4.

Table 19: Comparison of the ageing values of both devices

Aging Index	Bruker B287A	Bruker B287C	PE B287A	PE B287C
I_{CO}	0.0345	0.0443	0.0282	0,0487
I_{SO}	0.0479	0.0637	0.0954	0.1454

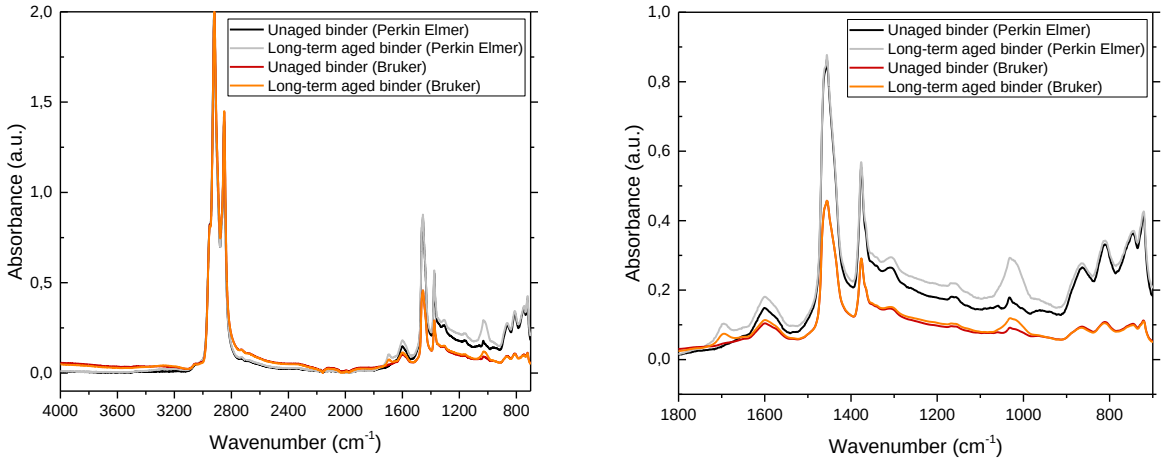

Figure 62: Comparison of Perkin-Elmer (black-gray) and Bruker (red-orange) measurements

4.3.5. Changes in the Spectra due to Insufficient Homogenization

After storing the aromatic and maltene fractions of the unaged binder B287A for several weeks in a dark place (shielded from light), some changes occurred in the FTIR spectra. Figure 63 depicts the obtained spectra of the maltenes fractions where bands at 1260, 1110, 1030 and 810 cm^{-1} emerge and further increase with time. Measurements were implemented after 0, 14 and 28 days.

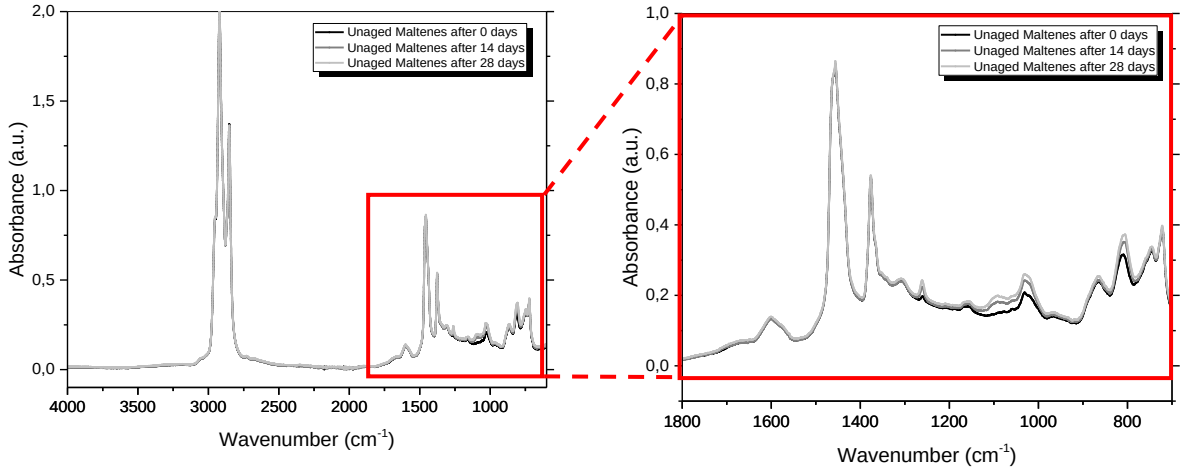

Figure 63: Changes in an exemplary maltenes fraction after 0, 14 and 28 days)

4.3.6. Light-Induced Ageing of the SAR Fractions

The light induced ageing effects were expanded for this study to the SAR fractions. Therefore, the saturates, aromatic and resin fractions of binder B637 were illuminated for three weeks in the laboratory. As mentioned in chapter 3.4.3 the chosen days for measurements were day 1, day 7 and day 21. They are labelled as Dx in the legends of the following plots.

The Saturates

Figure 64 shows the FTIR spectra of the saturates fraction of binder B637A. In this fraction no significant changes are observable. No increase or decrease in intensity or any additional bands are present over the whole wavenumber range.

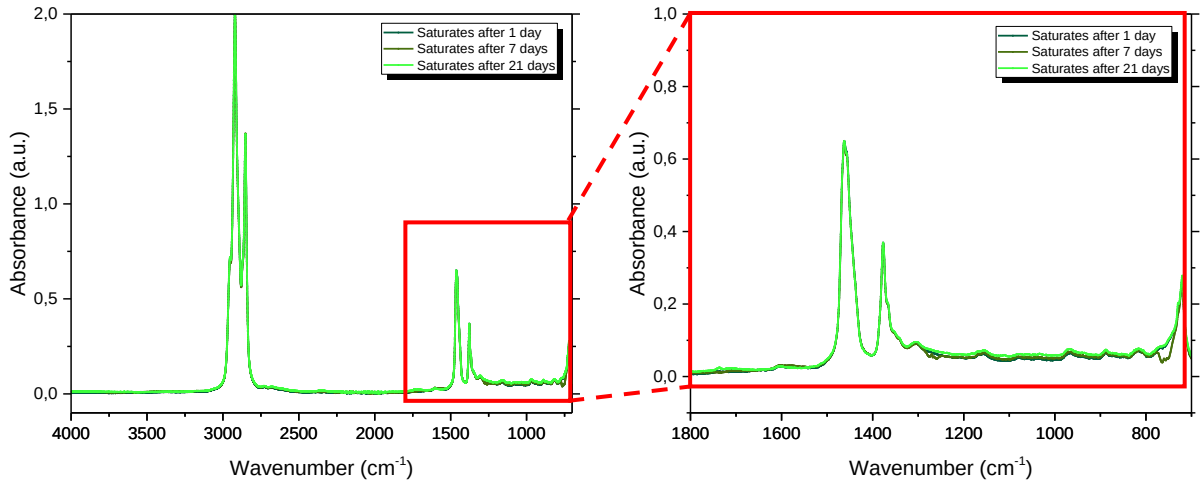

Figure 64: Light-induced changes of the saturates fraction of binder B637A after 1, 7 and 21 days

The Aromatics

Figure 65 shows the spectra of the aromatics with increasing storage time. There are significant increases in intensity at 1700 cm^{-1}, 1025 cm^{-1} and a general intensity shift between 1400 cm^{-1} and 900 cm^{-1}. Besides those changes, small increases in intensity at 1600 cm^{-1}, 1260 cm^{-1}, 870 cm^{-1} and

810 cm^{-1} are observable. The main difference to the commonly aged aromatics spectra (given in Figure 58) is the general increase in absorbance below 1400 cm^{-1} for the samples stored in the light.

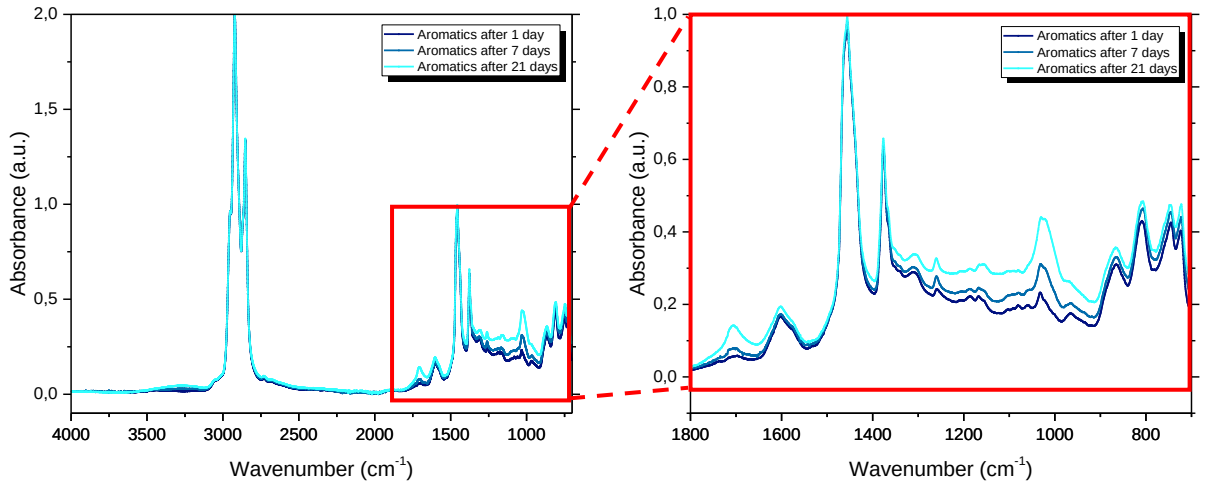

Figure 65: Light-induced changes of the aromatic fraction of binder B637A after 1, 7 and 21 days

The Resins

Figure 66 highlights the appearing changes in the resin fraction of binder B637A as a function of time. The intensity of the band at 1655 cm^{-1} increases as well as the bands at 1600 cm^{-1} and 1025 cm^{-1}. Besides that, the absorbance of the whole region below 1800 cm^{-1} shifts towards higher absorbance.

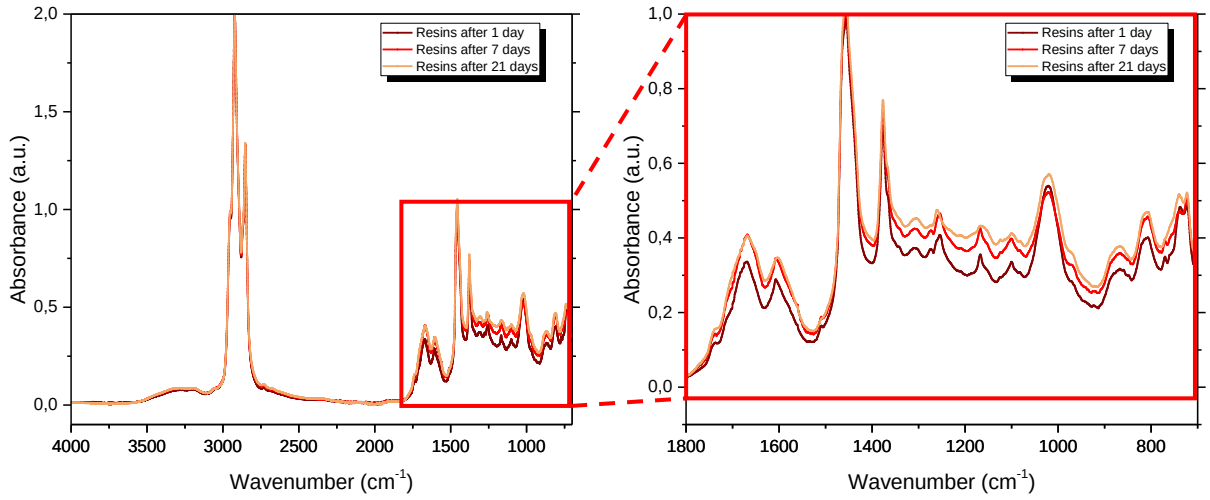

Figure 66: Light-induced changes of the resins fraction of binder B637A after 1, 7 and 21 days

4.3.7. Effects of Oxidation in Solution on the FTIR Spectra of the Fractions

By oxidizing the binders or the fractions in solution, other oxidizing pathways might be possible; hence, other evolving functionalities are measurable with FTIR. Figure 67 depicts three steps of this oxidation by plotting three spectra at different oxidation states ranging from Resin 1, no oxidation, to Resin 3, the harshest oxidation of the resin fractions in solutions. The band at 1730 cm^{-1} increases as well as the bands at 1260, 1180, 1110 and 980 cm^{-1}.

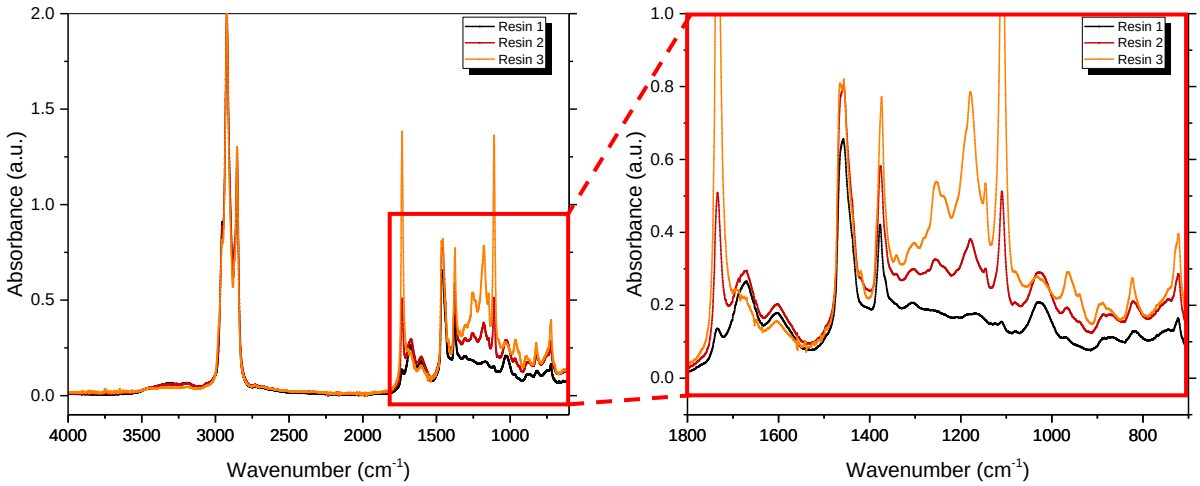

Figure 67: Three different oxidation states of a resin fraction of binder B287A dissolved in toluene

5. Fundamental Discussion

5.1. Time Dependent Studies

The preliminary tests had shown that the surface is changing by storing the binder at ambient temperatures and pressures in the laboratory. Significant changes do not only appear for unaged and slightly aged but do occur for every binder in every ageing state as the findings of chapter 4.1.1 suggest. Therefore, one has to consider different sorts of reactions that do occur during the laboratory ageing simulations at high temperatures and pressures compared to the rather soft conditions that are given in the laboratory. The next step was to look at the effect of visible light on the samples, which was the reason for storing samples in light and in the dark. As one can see in Figure 29 and Figure 32 for the binders B287A and B637A, light has great impact on the examined binder as signals at 1700, 1260, 1030 and 810 cm^{-1} arise and the absorption intensity of the whole region between 1350 and 900 cm^{-1} goes up. Compared to that, only slight changes appear in the spectra of the samples stored in the dark. (Figure 30 and Figure 33)

The first part of this discussion is going to focus on the spectral alterations and its correlated changes within the material. The emergence of bands at 1700 and 1735 cm^{-1} in binder B287A (see Figure 69) can be assigned to two different carbonyl stretching vibrations. The first one, which is observable from day one, can be linked to the vibration mode of ketones, whereas the shoulder that emerges after a few days corresponds to carboxylic acids. The shift between those signals (which are caused by similar stretching vibrations (C=O)) can be explained by taking a look at differences in chemical and electronic surrounding of the carbonyl bond. On the one hand, the direct neighbours of the carbonyl bond of the ketone group are alkyl groups. These groups have just small influence on the carbonyl band. This influence derives majorly due to the small electron-releasing character of alkyl groups, also called positive inductive effect (+I-effect), which leads to strengthening of the carbonyl bond. As a consequence, the respective IR band gets shifted towards higher wavenumbers when compared to aldehydes or formaldehyde. In the system of carboxylic acids two counteracting effects play important roles. On the one hand, the oxygen from the OH-bond strongly withdraws the binding electrons of the carbonyl band due to the high difference in electronegativity. On the other hand, the free electron pairs of the same oxygen can shift within the structure, which leads to different possible and stable resonance structures. By bringing lone pairs into the system, nearby the carbonyl band the system is stabilized. This effect is called +M effect or a positive mesomeric effect. The latter effect overwhelms the inductive effect in this case, which explains the shift towards higher wavenumbers for the carboxylic acid vibration.

The ketone band appears due to oxidation of a small layer on top the stored sample. Evidence for this claim can be found in [13, 14]. An affirmation of the statement of appearing carboxylic groups can be found in [14]. But one has to consider that these bands are also observable in the sample stored in the dark. With that said, this group is already inherent in bitumen (see [13]). Therefore, dynamic changes, such as interchange from different bitumen fractions and/or formation of surface structures of specific fractions could induce these changes in the spectra. As one can see in the resins sample in Figure 48 there are signals corresponding to carboxylic acids at the exact same wavelengths found in this fraction. Besides that, the band at 1100 cm^{-1} appears only if the 1735 cm^{-1} signal is present as well. The connections between both of those bands are found in the light, dark and in the resins fraction. It is most likely another vibration mode of the carboxylic acids as not just the carbonyl vibration produces infrared observable signals. The molecular structure of carboxylic acids and other possible vibrations are shown in Figure 68:

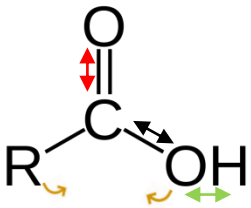

Figure 68: Different vibration modes of carboxylic acids

Four different vibrations are indicated with arrows. Other possible stretching vibrations besides the previously discussed carbonyl vibrations are the v (C-O(H)) (black arrow) and the v(O-H) (green arrow) observable in the wavenumber regions 1300-750 cm^{-1} and 3700-3200 cm^{-1}. The fourth vibration is bending vibration δ(R-C-O(H)), which is also present in IR spectra of carboxylic acids. Cutouts of the carbonyl region are given in Figure 69

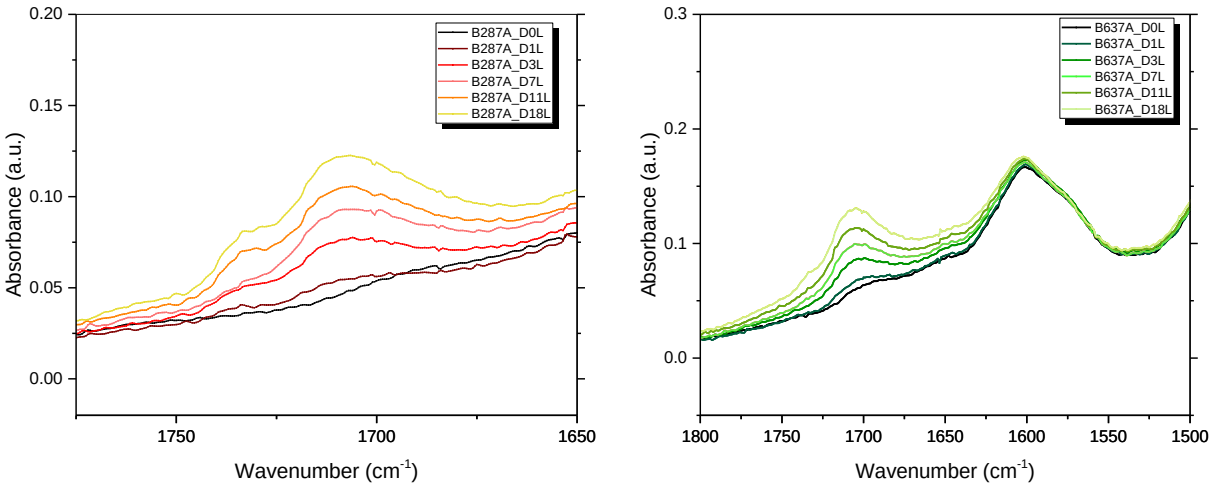

Figure 69: Cutout of the region between 1800 and 1500 cm^{-1} in binder B287A (right) and B637A (left) (light-stored)

The next change in the spectra appears in the middle region between 1350 and 900 cm^{-1} (see Figure 71). The reason for this general shift to higher absorption is the emergence of asphaltenes in the bitumen with ageing. As shown in Figure 37, Figure 38 and Figure 39 the asphaltene content increases for all three binders the higher the binder is oxidized. Keeping that in mind Figure 61 (different asphaltene contents) depicts the changes of the spectra for different asphaltene contents. With that shown, one can interpret that a rise in this region is connected to an increase in average asphaltene content at least in the observable area where the infrared light penetrates in.

Another oxidation band that grows is the sulfoxide band at 1030 cm^{-1}. The intensity increase of this functional group is just small in the samples stored in the dark but rises pretty strong for the light samples. Two other remarkable changes of the spectra are at 1308 and 1156 cm^{-1}. Possible explanations for these bands are emerging sulfones, which have not been addressed in literature yet. Figure 70 shows the oxidation pathway for sulfides, where the sulfoxides are the first oxidation product and the sulfones are the oxidation product of the sulfoxides.

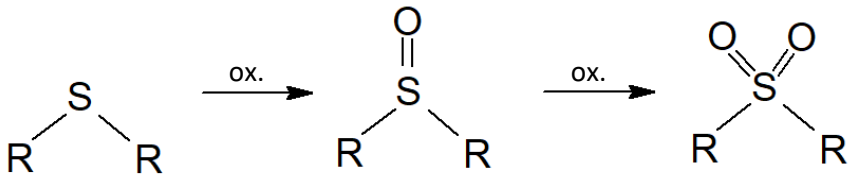

Figure 70: Oxidation pathway of sulfides

These sulfones give strong bands from 1350 to 1300 cm^{-1} and from 1160 to 1100 cm^{-1} corresponding to symmetric and asymmetric stretching vibrations ($v_s(SO_2)$ and $v_{as}(SO_2)$)in the molecule. [33]

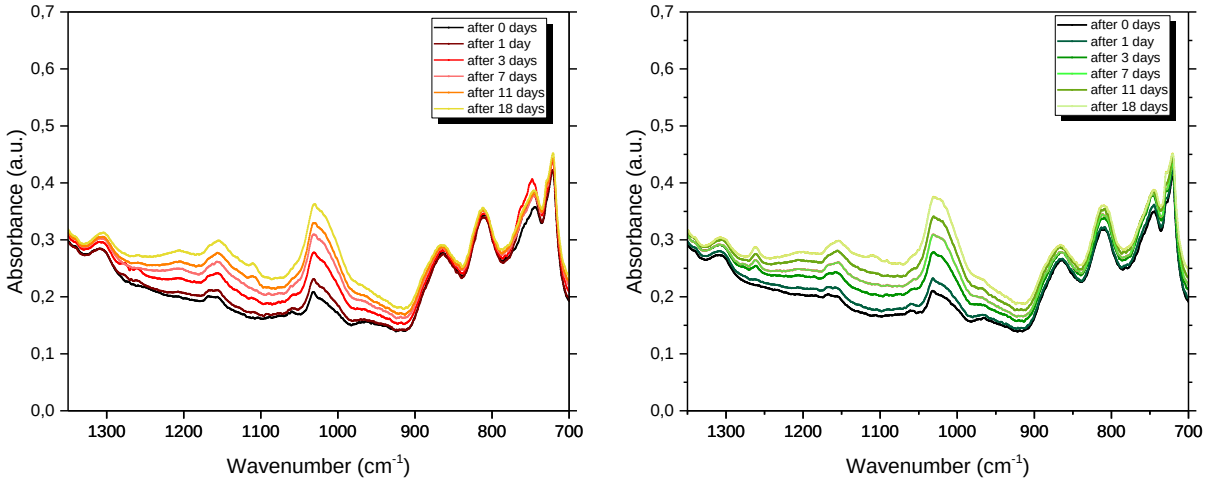

Figure 71: Cutout of the region between 1350 and 700 cm^{-1} in binder B287A (left) and B637A (right) (stored in the light)

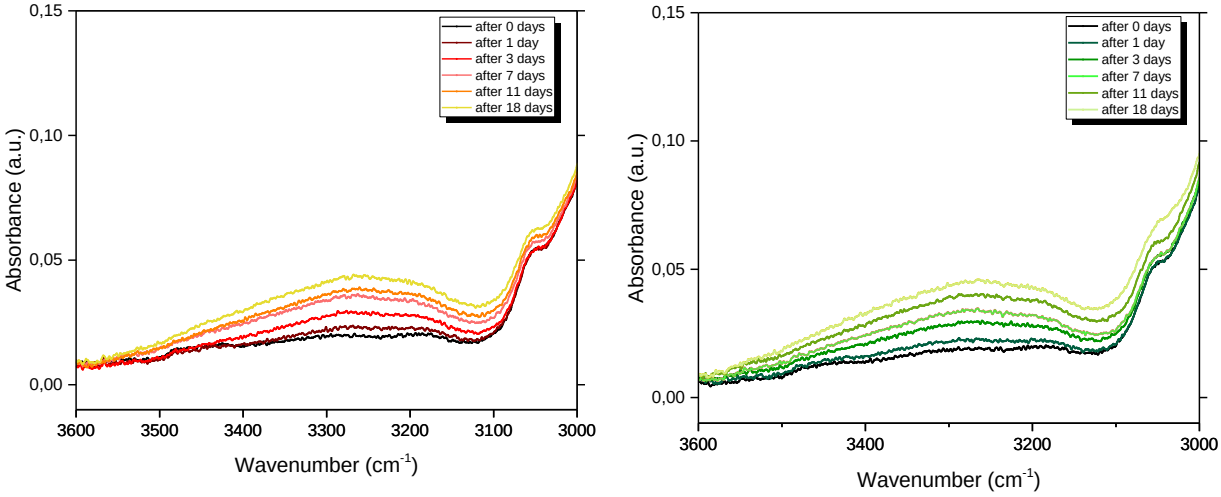

Figure 72: Cutout of the region between 3800 and 3000 cm^{-1} in binder B287A (left) and B637A (right) (stored in the light)

For binder B637A same tendencies are found. There are the bands at 1700 (ketones), 1030 (sulfoxides) and the shift in the region between 1350 and 900 cm^{-1} (increasing asphaltene content). The main difference is that no shoulder at 1735 cm^{-1} and with that no signal at 1110 cm^{-1} emerges. Another difference starts at day 3 where a signal at 1256 cm^{-1} emerges and with that a band at

1100 m^{-1} appears and the previously present band at 810 cm^{-1} also increases significantly. An interpretation of those changes, appearing for both modes of storage, would be sulfate esters. These compounds give rise to bands from 1268-1244 cm^{-1} ($\nu_{as}(SO_3)$), 1081-1041 ($\nu_s(SO_3)$) and 838-757 cm^{-1} (ν(S-O-C)) according to Larkin [33] . The molecular structure is depicted in Figure 73:

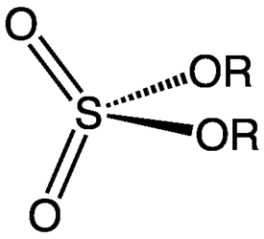

Figure 73: Organosulfate/Sulfate ester

Other possible explanations for these bands are esters or emerging alcohol groups but neither of them can correspond to all three bands at once. [33]

By taking a look at the ageing indices given for both binders and both storage places in Figure 31 and Figure 34 some trends are observable which are highlighted for the CO-index of binder B287A in Figure 74:

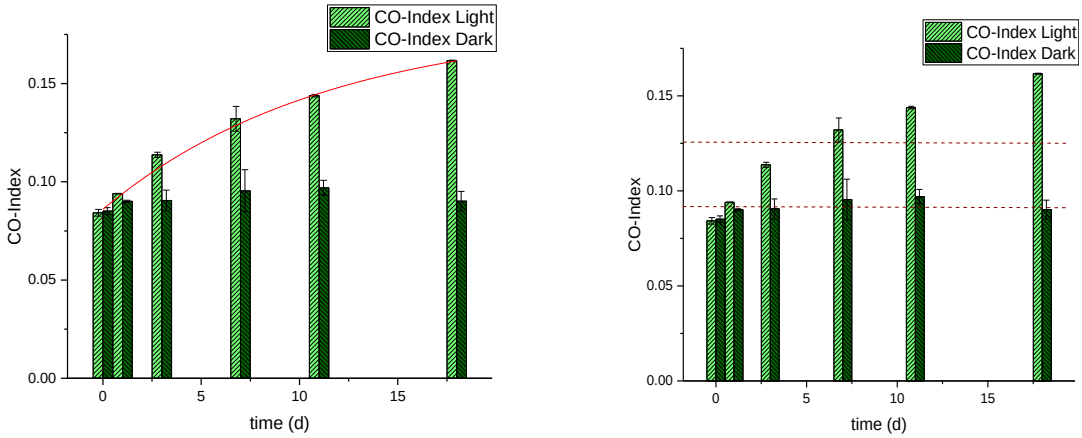

Figure 74: Approximated growth function (red in the left plot) and marked values for STA and LTA (right plot dashed lines)

Figure 74 depicts the change of the CO-Index with time for binder B287A. The continuous red line on the left of Figure 74 shows an asymptotic exponential function as approximation function to describe the increase of carbonyls in the binder. This approximation function was obtained with the computational program Origin and the mathematical formulation of this function is given in the attachments. The interesting information of this is that the oxidation rate, regarding carbonyls and sulfoxides, decreases with time which fit well to the suggested mechanisms of Petersen, described in chapter 2.2, where a fast oxidation process is followed by a rather slow second step of oxidation. A possible explanation for this behaviour is that the amounts of reactive compounds, which are responsible for oxidation, are decreasing on the surface. The decrease of initiators inhibits further fast oxidation and a passivation layer is formed. Reactive molecules from the air have to diffuse through this layer or the material has to rearrange itself in order that further oxidation in the material can happen. Hence, this diffusion process or rearrangement process are the most time demanding steps of this mechanism. And such processes are rather slow, where a decrease in reaction rate can be expected.

In the right graph of Figure 74 two dashed red lines are added. These lines correlate to the ageing values of short-term- (RTFOT) and long-term (PAV) aged samples of this binder. Thus, the value for short-term ageing is reached after just one day of storing in the light, whereas the value for long-term ageing is reached after 7 days. However, after a thorough homogenization of the samples stored in light, the values of unaged samples are reached again. With that in mind, one has to consider that the observed changes are just alterations on the surface.

Therefore, dynamic shear rheometer test runs were implemented as methods to measure the bulk behaviour of bitumen. The DSR results presented in chapter 4.1.2 and summarized in Figure 35 give great insights in the bulk behaviour of the bitumen samples based on how they were stored. There is a significant difference between the samples stored in the light and the sample stored in the dark, as the complex modulus increase much more for the samples stored in light. But, by comparing the obtained results to the values of short-term aged samples (Table 5), even the changes in the light samples are much lower compared to the common laboratory ageing method. This contradicts the results gained from IR spectroscopy, where after just seven days all common laboratory ageing values were exceeded. These results are leading towards two plausible interpretation of the appearing phenomenon: The first possibility is that the light-induced ageing is an effect that appears only on the surface/or surface near regions and with that, the bulk behaviour is affected far less. Another way to interpret this observation would be that light does not oxidize molecules on the surface but rather catalyses molecular self-assembly on the surface. In the course of this process specific molecules that are evenly dispersed in the bitumen matrix might accumulate on the surface. The concentration shifts at the surface, caused by diffusion processes within the material, lead to enhanced signals of particular molecular groups in the “surface-sensitive” FTIR spectra.

5.2. Fast SARA: Gravimetry

The interpretation and discussion of the gravimetric analysis is going to cover the fractions one by one starting with the saturates fraction in chapter 5.2.1.

5.2.1. Saturates

As mentioned in the results chapter, there was not much change in mass observable in the saturates fractions during the ageing procedures. The charts of Figure 37, Figure 38 and Figure 39 are showing that the amount of saturates in all three unaged binders made up for a fifth to a fourth of the mass of the whole binder. For the common laboratory ageing methods, RTFOT and PAV, the mass share does not change at all. A possible explanation for such behavior could be that the molecules of the saturates fraction are inert under these conditions. This means that even the high pressures and temperatures applied in PAV do not promote oxidation in this polarity fraction. This correlates with the picture that is drawn for molecules in the saturates in common literature. In these excerpt saturates are widely seen as rather elongated saturated structures, with very few and small aromatic compounds attached, generally speaking, a mixture of unreactive species. (LITERATUR) But especially in the results of binder B287 interesting findings are observable, as the field ageing actually effects the saturates content. A mass loss of approximate 2 % (from roughly 22 % to 20%) was measured. Those results indicate that the common laboratory ageing methods do not properly simulate the ageing processes in bitumen in use on the field. As a next step, one has to find the differences between PAV and the field by taking a look on the given parameters. The temperature (60 °C at max, depending on the region) and pressure (1 bar) are lower for the field aged sample. Furthermore, the oxidative species inherent in the atmosphere (NO_x, OH· or O_3; see chapter 2.2.3), but also the radiation from the sun are major differences.

Hence, the newly developed ageing procedure (VBA) should emulate such conditions more properly, as no additional pressure is applied and O_3 and NO_x are introduced into the system. And Figure 37-

Figure 39 confirm those assessments, as the mass content of saturates has decreased 2-3.5 % in the VBA aged samples. The mass loss even exceeded the mass loss of Field ageing for binder B287 which indicates that either less ageing duration or a lower ozone concentration should be chosen for further ageing runs. The chemical changes in the saturates, which were observed via FTIR spectroscopy, are going to be discussed in chapter 5.3.1.

5.2.2. Aromatics

The next polarity fractions for this discussion are the highly reactive aromatics. The mass percentages given in Figure 37-Figure 39 were 53 % (B287A), 47 % (B637A) and 40 % (B504A). A massive difference in mass content dependent on the source is observable (13 % difference between binder B287A and B504A), which confirms the high dependency of fractional mass content on the bitumen source shown e.g. in literature [6]. The mass losses during ageing correlate with the content of the unaged samples, where the binder with the highest aromatics content (B287A) decreases the most during ageing and the binder with the lowest starting aromatics content decreases the least. (B504A) The values for these losses during the VBA aging procedures are ranging from 21-11 % (from unaged to VBA aged for the different binders). By taking a look at the different ageing procedures, the losses do increase in the following order: RTFOT<PAV≈VBA1≈VBA2<Field in the B287A sample and RTFOT<PAV<VBA1 in the other samples. The mechanistic reason for these mass losses is the presence of highly reactive molecules in the aromatic fractions. These molecules are getting oxidized leads to an increase in polarity of the same molecule. Due to these polarity enhancements, many of the former aromatic molecules are eluted with the fractions with higher polarity (resins or asphaltenes). (see [14])

5.2.3. Resins + Asphaltenes

The mass percentages of resins in binder B287A and B637A are comparable (Table 6; 10-11 %) whereas the content derived from binder B504A nearly doubles those contents with approximately 18 %. The measured asphaltene contents do differentiate for all binders and are ranging from 13 to 21 %. For the changes during the ageing processes both fractions will be analyzed at once, because the asphaltene content is strongly linked to the resins content.

The asphaltenes are the highest polarity of this complex mixture. This means that all molecules that exceed a certain polarity threshold that are not dissolved in n-heptane finally end up in this fraction. Not just the most reactive molecules of the aromatics but also reacting molecules from the resins fraction can end up as asphaltenes. Two pathways are plausible for the formation of asphaltenes from resins. Either there are reactive molecules inherent in the resins which get oxidized directly from the beginning, or a first oxidation of aromatics lead to the development of resins from aromatic structures at first (for the short term ageing procedures), which then are further oxidized, do agglomerate or rearrange themselves with resulting molecules, that are higher in polarity. A possible explanation for the higher asphaltene and lower resin content in the RTFOT+PAV aged binder could be that the ageing conditions are very harsh, increasing the polarity of such molecules faster, accelerating their polarity shift towards the asphaltene fraction. The balance between resins and asphaltenes content is an important factor and presumably can give insights in the ageing mechanism of bitumen. At what rate the polarity in bitumen shifts can provide valuable information in regards to understand field ageing and ageing susceptibility. Therefore, a comparison of the different long-term ageing methods applied on binder B287 is highlighted in Figure 75 :

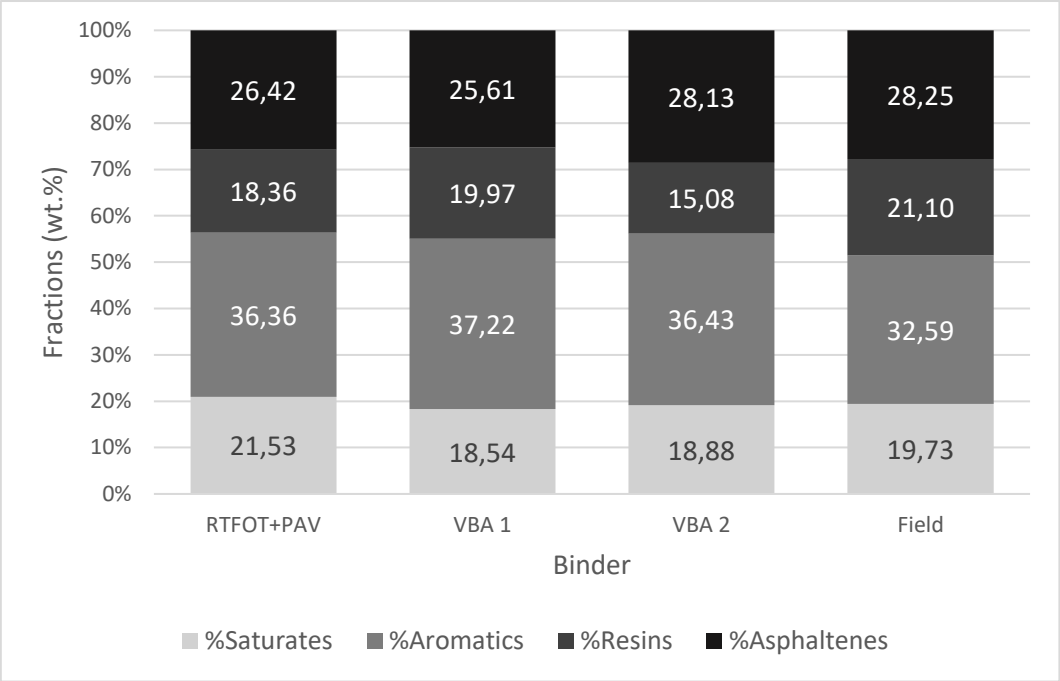

Figure 75: Comparison of the LTA methods

The field aged sample has shown the highest loss in aromatics (over 20 %) and neither the common laboratory ageing methods (PAV) nor the two VBA trials with different parameters came close to emulate this trend with losses of 16-17 %. VBA 1 was implemented with low O_3 concentration over 12 days whereas the parameters for VBA 2 were set at high O_3 concentrations but a rather short time of 3 days. Comparing those two, the mass loss in aromatics are very similar. What is really interesting about this, are the mass contents of resins and asphaltenes. In Table 7 the summation of both fractions is shown, which does indicate that overall the same amount of higher polar fractions is produced. However, the mass distribution between those fractions varies massively, as the resins contents are 20 % and 15 % and the asphaltene contents are 26 % and 28 % for the ageing methods VBA1 and VBA 2, respectively. This confirms the assumption that a higher ozone content leads to an aggressive and oxidative ageing atmosphere, where more molecules can be oxidized. As described before there are several ways in describing the lower content in resins in the VBA 2 procedure: A first explanation could be that the molecules from the aromatics fraction are oxidized multiple times and/or agglomeration is enhanced significantly in the process. The molecules from the aromatics are shifted directly in to the asphaltenes fraction, resulting in a lower resins content compared to the softer ageing method VBA1 and Field ageing. Another plausible explanation would be that besides the aromatics also structures from the resins fraction are oxidized in this environment. This pathway would include an increase of resins due to aromatics oxidation, but also a component of decrease, due to the loss of former resins to the asphaltenes. An additional way could include both reaction pathways where structures from the aromatics can either end up in the resins or in the asphaltenes. The resins from the virgin binder and the newly added “resins” derived from the aromatics are reacting as well, which leads to the shift of those structures to the asphaltenes.

5.3. Fast SARA: Spectroscopy

This subchapter will not just cover the systematic discussion of the spectral analysis of the fractions of each binder, but will also include the discussion of the various, additional experiments (chapters 3.4.2, 3.4.3, 3.4.4 and 3.4.5). The intention for this was to present a more extensive and sounder look at the interpretations that are made, regarding functional groups and their connection to certain bands in the spectra. As implemented throughout this work the discussion is going to start again with the saturates.

5.3.1. Saturates

All of the measured spectra show similar bands and the exact wavenumbers are summarized in Table 14. Those signals can be linked to different bending and stretching vibration modes of alkyl functional groups (see Table 10 and Figure 14), which confirms the presence of great amounts of saturated hydrocarbons in the mixture. Besides those signals also aromatic bands (at 1600 cm^{-1} and below 900 cm^{-1}) and two bands (presumably) from sulfone containing molecules (at 1310 cm^{-1} and 1160 cm^{-1}) are observable in the spectra. The presence of low amounts of aromatic compounds in the saturates fraction is well documented in literature. [6, 14] Further evidence found in literature is derived through mass spectroscopy measurements from Handle et al. [47] where the obtained fragmentation pattern did show the presence of aromatic functionalities in this fraction. Sulfur containing fragments (CHOS) were also observed via mass spectroscopy [47] which strengthens the suggestion of stable sulfur containing groups (e.g. sulfones), inherent in this polarity fraction.

By taking a look at the ageing behavior of the saturates one can see in Figure 46, Figure 52 and Figure 57 that no changes do appear during all applied ageing procedures. This is in parts consistent with the results obtained from chapter 4.2, especially for the common ageing methods, RTFOT and PAV. However, the results of the gravimetric analysis of the field aged and VBA aged samples suggest other results, as the saturates decrease in mass content, and with that, some changes were estimated. A plausible explanation on why those changes are not observable with FTIR is that ageing enhances the polarity of the reacting molecules. With that, those molecules are gathered with the fractions with higher polarity. Therefore, VBA ageing of the already separated saturates fraction would be an experiment of great interest, as the results obtainable with such a set-up might give insights in the oxidation mechanisms appearing in molecules of this fraction. The reacting molecular classes in this fraction are most probably the small aromatic structures. This would again correlate very well with the mass spectrometric measurements [47] that provided results in regards to the mass loss of small aromatic structures in the saturates fraction during ageing (from 17 wt.% to 4 wt.%) . As mentioned in the opening paragraph of this chapter, also the side experiments are going to be part of this discussion. Such a side experiment was the light-induced ageing of the SARA fractions over a time span of three weeks (chapter 4.3.6). This is a soft ageing method, where visible light from the laboratory lamps is directed towards the samples at ambient pressures and temperatures. Same as for the time-dependent studies (chapter 4.1) of the base binder, also the spectra of the fractions might change with time. However, Figure 64 depicts that the measured spectra after one and after three weeks of light-induced ageing show no changes at all. To conclude, in regards to saturates ageing, those conditions were not sufficient to change the resulting FTIR spectra. Therefore, mechanistic changes in the saturates through ageing are still a research topic that needs to be analyzed.

5.3.2. Aromatics

The next fractions that are going to be discussed are the aromatics. The FTIR spectra of the aromatics fraction are given in Figure 47, Figure 53 and Figure 58. Compared to the saturates more bands and intensity changes are observable in this fraction, which correlates with the assumption of very

reactive compounds in this fraction. As defined in the previous chapter the alkyl signals are obtained again and do show the highest intensities of all appearing bands. Besides those bands, also the sulfone (1310 and 1160 cm^{-1}) and alkene (960 cm^{-1}) bands are present again but with different intensities. What differentiates this fraction from the saturates are bands with high intensities at 1600, 870, 810 and 780 cm^{-1}, which do represent the vibrations of aromatic and heteroaromatic groups in the fraction. Another difference is the shift in intensity below 1600 cm^{-1} compared to the saturates and additional signals at 1030 cm^{-1} (sulfoxides) and 1260 cm^{-1} (sulfate esters). The differences between the unaged fractions of all binders are depicted in Figure 42. Not much difference is observable over the whole spectrum. The aromatics fractions of B504A and B637A are showing slightly higher bands at 1700 cm^{-1}, 1200 cm^{-1} and 980 cm^{-1}. The higher intensity at 1700 cm^{-1} indicates the presence of ketones, which either are formed in ageing processes or are present in the system from the start. The higher absorbance at 980 cm^{-1} suggest higher contents of alkene structures and the band at 1200 cm^{-1} could be linked to a variety of different functional groups (e.g. alcohols, sulfate ester, ester). Furthermore, the bands at 1600, 870, 810 and 780 cm^{-1} show the highest intensities for binder B504A. As these bands are all assumed to be aromatic/heteroaromatic (pyridine) signals (see Table 10), a higher intensity can be explained by a higher share of aromatic structures in this binder.

Furthermore, the ageing tendencies and consequences on the aromatics spectra are depicted in Figure 47, Figure 53 and Figure 58. It is observable that ageing induces changes especially at 1700 cm^{-1}, where the intensity grows during the different ageing processes. (Increases from RTFOT to Field in B287 and to VBA for the other binders) This increase can be linked to the formation of ketones, which are generated during oxidative processes (see chapter 2.2). Also an increase in aromaticity (sum of all aromatic signals) in all long-term aged aromatic fractions is measured which confirms a further observation made by Petersen [14] and discussed in chapter 2.2. A possible explanation for the remaining signals (emerging or growing) with lower intensities in the aged samples at 1260, 1080 and 810 cm^{-1} are organic sulfate ester ($ROSO_3$) vibrations. Besides those changes no further change is observable, which could lead to the assumption that mainly ketones and aromatic structures are formed in the aromatics fraction during ageing. To ensure such statements a soft ageing method was applied on the fractions themselves (see chapter 3.4.3). A cutout of the obtained spectra of this ageing process compared to the obtained spectra of common ageing processes is given in Figure 76.

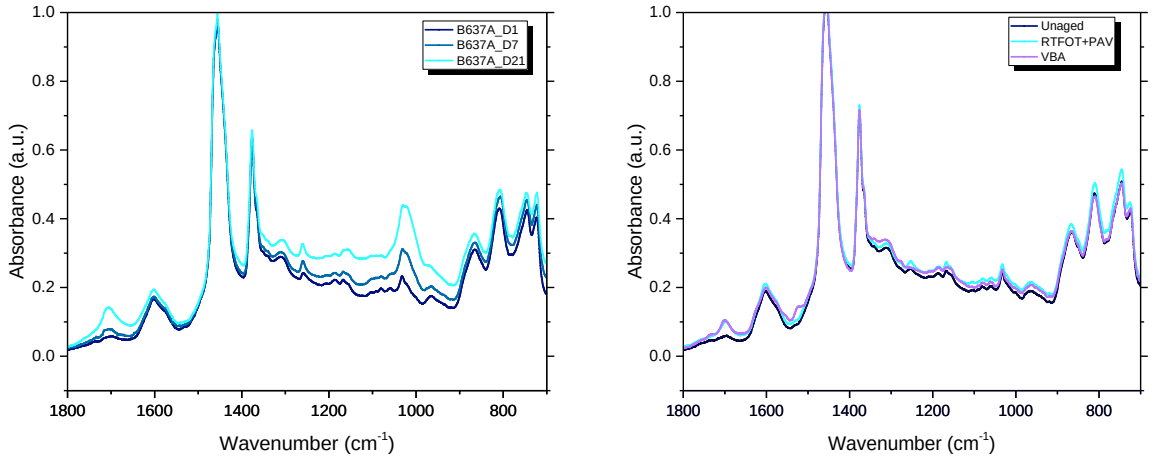

Figure 76: Cutout (1800-700cm^{-1}) of the light induced ageing (left) and the common ageing (right) experiment of the aromatics fraction of binder B637

In this experiment not just the ketone band do increase massively but also the sulfoxide band at 1030 cm^{-1} and the whole region between 1350 and 900 cm^{-1} is increasing significantly. With that result, the previous assumption has to be denied. Not just ketones are formed during the applied ageing processes but also a great amount of sulfoxides and other compounds that contain hetero atoms (e.g. alcohols, esters, sulfones). Furthermore, the reason for the missing increase of sulfoxide intensity in the common ageing procedures has to be linked to a shift in polarity for most of the emerging sulfoxides. Hence, the sulfoxide containing molecules are mostly found in the resins and asphaltenes fraction. Finally, the increase of intensity in the bands connected to sulfate ester has to be looked upon with great attention. These bands do not increase according to the previously mentioned order: Unaged<RTFOT<PAV<VBA1<VBA2<Field (for binder B287). They rather appear sometimes and sometimes they do not, but with greater probability in aged samples than in unaged samples. This is comprehensible by taking a look at the result from the time dependency studies of the whole binder B637A in the light and in the dark (chapter 4.1) and the study containing maltenes and aromatics which were stored for some time in the dark (chapter 4.3.5). In all of these studies signals of sulfate esters do appear as well. These observations lead to the following suggestion: As the intensity of the bands is not affected by any of the implemented ageing methods but is strongly dependent on the length of storage time one can assume that those structures were in the aromatics fraction from the start. As a consequence, the share of molecules that do contain such groups has to increases on the surface and on surface near areas with time. By dismissing external sources (mainly oxidation) a possible way to describe those changes are dynamic processes within the material where those structures tend to occupy the surface region. An explanation for this tendency can be derived by looking at possible energy minimizing effects. One way to reduce the energy of the whole system would be a reduction of the surface tension. In such scenarios amphiphilic molecules like sulfate esters might arrange themselves that the polar head groups (sulfate part) is directly on the surface and the apolar rest looks into the system. They basically behave like micelles, which would explain that as time goes by many of these molecules arrange on the surface and the IR-signal, connected to these groups, grows.

All VBA aged samples show two bands between at 1600 and 1500 cm^{-1}, which were also found in the base binder spectra of the VBA aged samples. Cutouts of this particular region are given for binder B287 and B637 in Figure 78. However, in the aromatics the first band is more intense than the second, whereas the intensities in the base binder spectra are almost equal (Figure 45). The reason for the appearance of these bands solely in the VBA samples is probably linked to the much higher concentrations of ROS in the altering atmosphere. Especially NO_x might interact with the binder to form nitro aromatics or nitro alkanes, where the emerging nitro groups give rise to bands in that particular region. But nitro groups do not just give rise to the asymmetric stretching vibrations $\nu_{as}(NO_2)$, but also to the symmetric stretching vibrations $\nu_s(NO_2)$ of this functionality. Table 13 shows that the second band is expected between 1357 and 1318 cm^{-1}. And the cutout in Figure 79 shows that as a matter of fact the intensity increases and a band emerges in this region between 1350 and 1310 cm^{-1}.

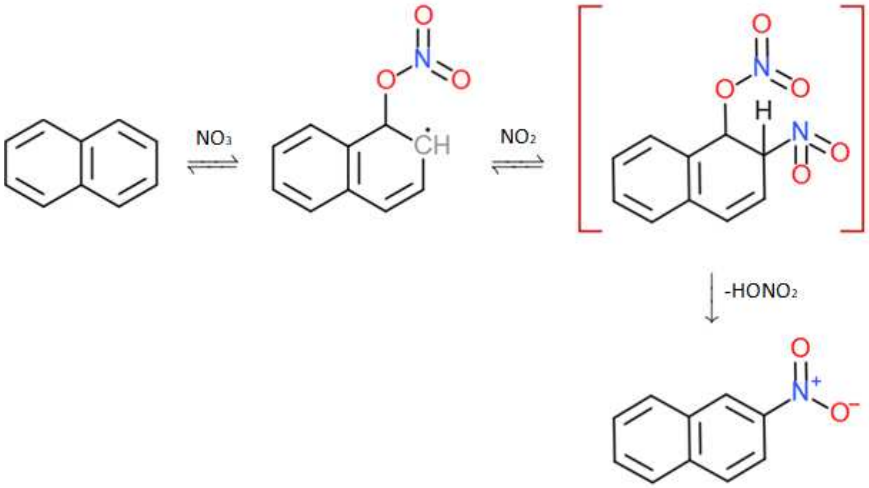

Figure 77: Possible oxidation mechanism of aromatic compounds with NO_x [49, 50]

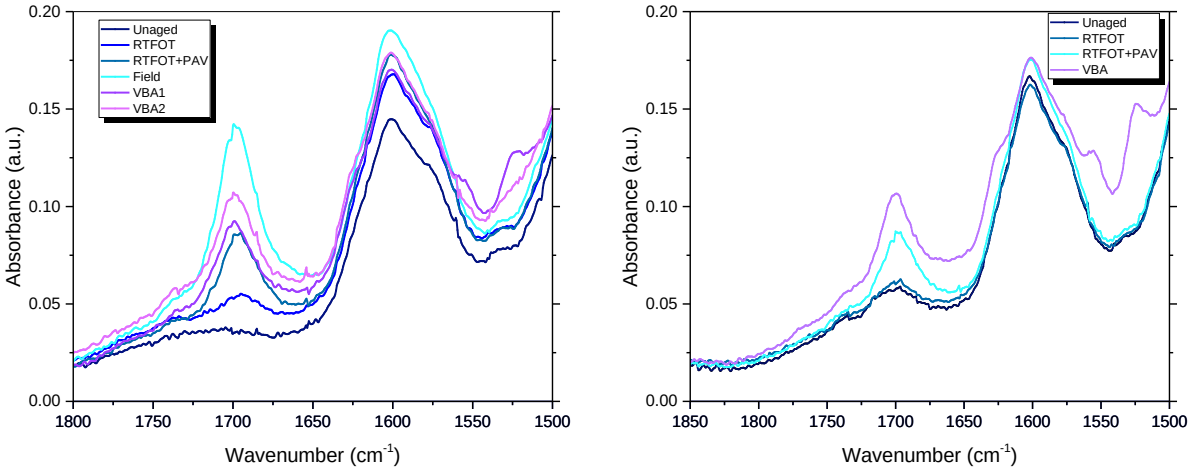

Figure 78: Cutout (1800-1500) of the aromatics spectra of binder B287 (left) and binder B637 (right)

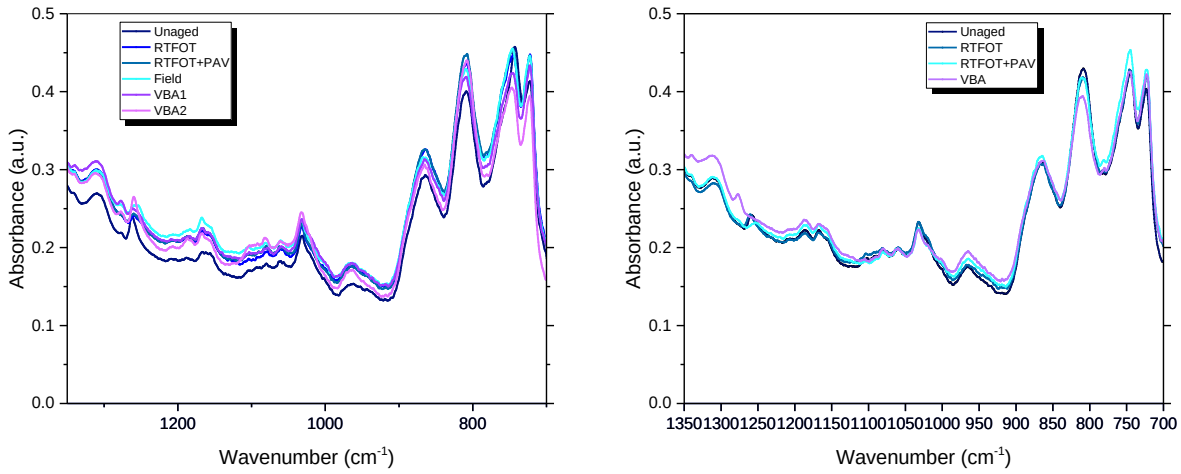

Figure 79: Cutout (1350-700 cm^{-1}) of the aromatics spectra of binder B287 and B637

5.3.3. Resins

The obtained spectra of the resins are given in Figure 43 (comparison of all binders), Figure 48 (B287), Figure 54 (B504) and Figure 59 (B637). The resins spectra show for all binder very intensive alkyl bands, aromatic signals as well as sulfone bands and very intense sulfoxide bands at 1025 cm^{-1}, which contain a shoulder around 980 cm^{-1} (the alkenes). Furthermore, the overall intensity in the region below 1800 cm^{-1} in relation to the signal at 2921 cm^{-1} rises again significantly. The main difference to the fractions discussed previously is the carbonyl region of the spectrum (from 1800-1640 cm^{-1}). In this region, a very big band appears at 1655 cm^{-1} in all three binders. This signal is connected in literature to the presence of 2-quinolones in the resins fraction. [43]

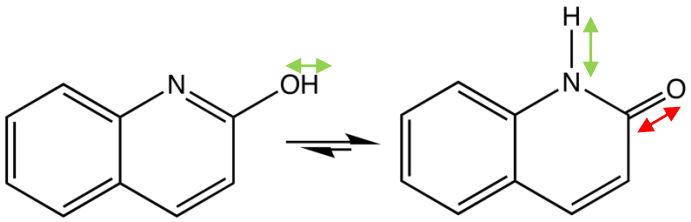

Figure 80: The equilibrium between 2-quinolone (right) and its tautomere 2-hydroxylquinolone (left)

The vibrations that are responsible for these bands are again the carbonyl vibrations of such molecules. The shift to lower wavenumbers in comparison to ketones and carboxylic acids is a direct consequence of the surroundings of the C-Atom of the carbonyl group. The nitrogen atom as well as the aromatic system withdraws electron density from the carbonyl bond (negative inductive and negative mesomeric effect), which leads to a weaker carbonyl bond and a lower observable wavenumber in the FTIR spectrum.

The presence of great amounts of 2-quinolones can additionally explain the increase of the main aromatic signal at 1600 cm^{-1} in comparison to the signal of the aromatics fraction. Furthermore, 2-quinolones contain a N-H-group (from the amid) which give rise to the band at 3470-3200 cm^{-1} (stretching vibration of this group; Table 13), but not to other conceivable vibrations (e.g. v(C-N-H)) due to steric hindrances in cyclic rings [33]. Another signal present in binder B287 and B637 in this wavenumber region is the signal at 1735 cm^{-1}, which can be linked to the carbonyl vibrations of carboxylic acids in the resins fraction. Binder B504 might contain these molecules as well but in the obtained spectrum it is overlapped by a third signal at 1700 cm^{-1}, that only appears in this binder. This signal can be linked to the carbonyl vibrations of ketone containing molecules. The other bands that differ in binder B504 compared to the other two binders is the enormous difference in the intensity of the sulfoxide bands the lower intensity of 2-quinolones and aromatics as well as the absence of the signal around 1100 cm^{-1}. The much higher intensity in both oxidation defining bands (ketones and sulfoxides) in binder B504 but also the results obtained in the aromatics FTIR spectra and in the gravimetric part do suggest that this binder is more oxidized (by this definition) from the start than the other two.

B287

Due to the complex ageing behavior of the resin fractions, each binder will be discussed in detail. Figure 48 depicts the obtained spectra of all aging states of binder B287. The sulfoxide band at 1030 cm^{-1} increases very strongly and the trend is following the order: unaged<VBA<Field≈RTFOT+PAV. This differentiates strongly from the "ageing-orders" in the aromatics and the pure bitumen sample. A plausible explanation for this would be that the molecules aged with VBA and on the field sometimes undergo multiple oxidations, due to the rapidly harsher

conditions. With that the polarity would increase more and faster, which would result in a postponed elution and slightly lower sulfoxide contents.

PAV-ageing leads to decreasing intensities in the region between 1800 and 1625 cm^{-1}. The carboxylic-, quinolone- and the main aromatic band are decreasing in this process from unaged to PAV aged binder. The carboxylic acid signal is completely gone for the PAV aged sample. Besides that, the intensity between 1300 and 1100 cm^{-1} is lower and the sulfoxide band has shown the highest increase in intensity. One explanation for this phenomenon could be oxidation or cleavage reactions of the 2-quinolones in which their polarity increases. That increase in polarity might lead to insolubility in n-heptane and with that those molecules would finally appear in the asphaltenes fraction. The intensity loss between 1330 and 1100 cm^{-1} is most likely a combination of increasing amounts of molecules from the aromatics, which reduce the intensity in this region, and the loss of former resins structures due to oxidation.

The VBA and Field aged samples do not decrease between 1350 and 1100 cm^{-1} but do show increasing intensities of specific bands. (1310, 1270, 1260 and 1110 cm^{-1}) Besides those changes, the 2-quinolone signal decreases as well and is shifted towards higher wavenumbers (1675 cm^{-1} for the field and 1685 cm^{-1} for the VBA2 aged sample). These shifts can be explained by an emergence of ketones during the ageing process. The bands of ketones, which would normally appear at 1700 cm^{-1}, overlap with the 2-quinolone band to form one big band. Especially the spectrum of the VBA 1 aged sample suggests two bands for that matter. In this spectrum the 2-quinolone band decreases the most and appears as a shoulder of the appearing ketone band. The higher intensity and the lower shift in the field aged samples may originate from the fact that fewer molecules are shifted to the asphaltenes fraction compared to the VBA ageing method.

Other potential reasons for the decreasing intensity of the quinolone signal are: 1) gain in overall polarity during the ageing processes in such molecules, which afterwards leads to the elution with the asphaltene fraction. 2) Esterification or emergence of imides take place 3) Changes in the monomer-dimer equilibrium of 2-quinolone (potential mechanisms depicted in Figure 81).

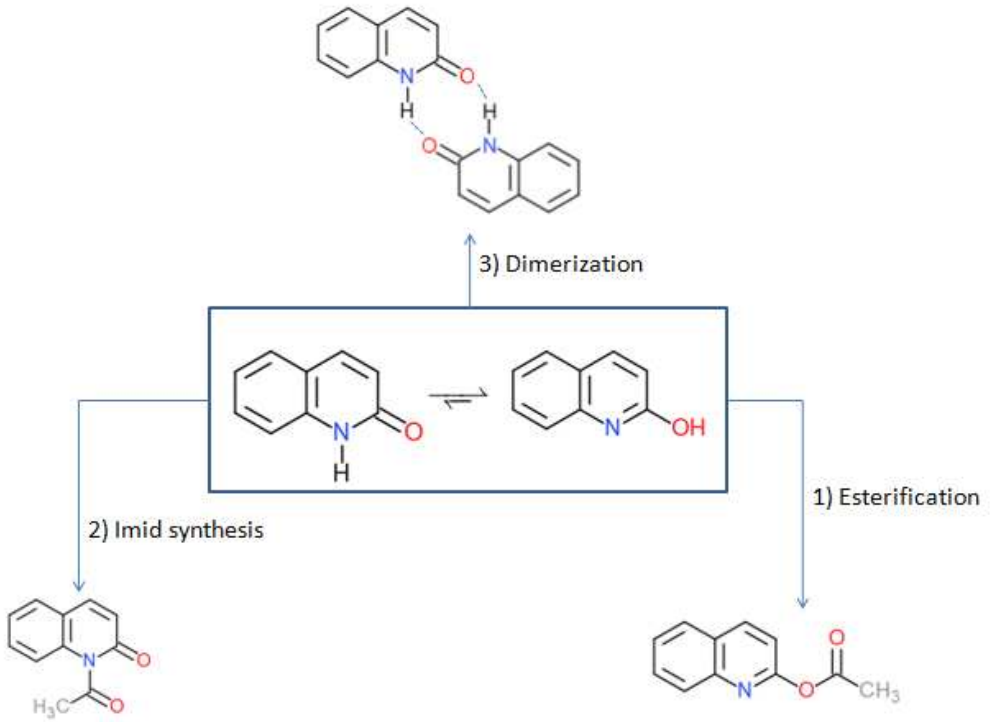

Figure 81: Possible pathways of 2-quinolones

Discussing now pathway 3 where according to [43] 2-quinolones are not just present as free molecules but also form dimers with other 2-quinolones or carboxylic acids. The intermolecular forces responsible for this dimerization are hydrogen bonds. The carbonyl band of the 2-quinolone dimer is at 1664 cm^{-1} whereas the carbonyl band for free 2-quinolones is at 1680 cm^{-1} according to [43]. By applying this information to the obtained results of this thesis, the 2-quinolones in the unaged resins fractions might be primarily present in their dimerized form. And with ageing the quinolone-quinolone bonds are broken and more and more monomers are formed.

A next step is to include the wavenumber region above 3100 cm^{-1} to the further discussion of 2-quinolones. In this region a very broad band ranging from 3550-3100 cm^{-1} and a further band on top of this band at 3200 cm^{-1} are observable. The broad band (3550-3100 cm^{-1}) originates from OH-stretching vibrations of different alcohols, phenols but also from water molecules. The second one is due to inherent amides (2-quinolones), more specific, due to the N-H-stretching vibrations of such molecules. To analyze the changes a cutout of this region is presented in Figure 82.

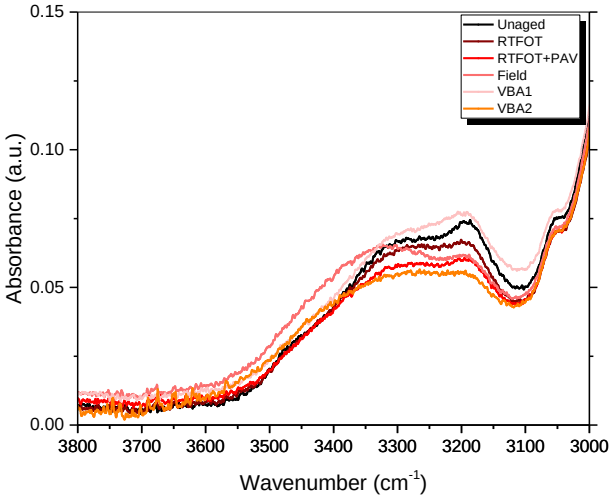

Figure 82: Cutout (3800-3000cm^{-1}) of the resins fractions of binder B287

In this figure a loss in intensity at 3200 cm^{-1} from unaged to VBA2-aged sample (intensity order: unaged≈VBA1>RTFOT>PAV≈Field>VBA2) is observable. The VBA 1 ageing method shows the highest intensity, but the form of the band would suggest that the increase of water or OH-containing structures is the main reason for the higher overall intensity. The mentioned intensity (without VBA1) order correlates also with the intensity order of the other 2-quinolone band at 1670 cm^{-1}. This observation strengthens the dimer-monomer theory where a lower dimerization grade has to lead also to a wavenumber shift of the N-H vibration (dimerization weakens the N-H bond) and with that to a decreasing band at 3200 cm^{-1}. But the esterification theory is also still a possible pathway; where due to the formation of esters the N-H signals disappear the more esters emerge. In conclusion, more research in this field and the use of other analysis techniques might be necessary to resolve this open question.

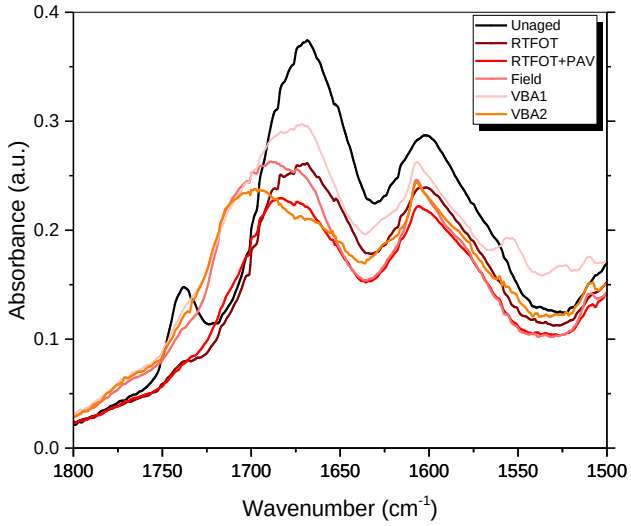

Figure 83: Cutout (1800-1500cm^{-1}) of the resins fractions of binder B287

Additionally, two bands between 1600 and 1500 cm^{-1} do appear in the VBA 1 aged sample. As previously described (in the aromatics subchapter), those bands arise due to the emergence of nitro groups. In contrast to the aromatics, the first band, appearing at 1560 cm^{-1}, is higher in intensity than the second one at 1525 cm^{-1}. A possible interpretation of those differences in intensity might be that the nitro groups can attach to two different classes of molecules (e.g. small aromatic structures and polycyclic structures). The intensity of the bands further depends on which molecular class has higher mass percentages within a particular fraction. Thus, the resins fraction would have a band with higher intensity that correlates to bigger, polycyclic aromatic structures whereas the aromatics fractions would have higher intensities at the band which correlates to smaller aromatic compounds. With that said the bonded might lead to indirect information about the distribution of aromatic structures within a fraction.

B504

Cutouts of the resins fractions of binder B504 are shown in Figure 84 (1850-1500cm^{-1}) and Figure 85 (1380-700 cm^{-1}). As mentioned before this binder shows a strong carbonyl vibration band at 1700 cm^{-1}, corresponding to inherent ketones, which does not increase with PAV ageing but do slightly increase during the VBA ageing process. Furthermore, the PAV aged sample differs from the unaged sample with bands at 1260, 1100 and 810 cm^{-1} which can be linked to emerging sulfate esters. Also the intensity of the sulfoxide band at 1025 cm^{-1} increases in the PAV sample compared to the unaged and the VBA aged samples. The VBA aged fraction do not show the three sulfate ester bands but the general intensity between 1330 and 1100 cm^{-1} increases compared to the unaged and the PAV aged resins fraction. This can partly be explained by the growth of sulfone content in this fraction, which would also explain the “constant” sulfoxide content during the ageing process. It is more likely that sulfoxide are the first products during the ageing process (observable in the PAV spectrum) followed by a second oxidation step, where sulfones are the products of the sulfoxide oxidation. The VBA aged fraction shows again two bands at 1560 and 1525 cm^{-1} (nitro signals) where the first band is again higher in this fraction. Finally, a notable shoulder appears in the VBA aged sample above 1750 cm^{-1}. Due to the harsh oxidation conditions the formation of anhydrides or imides can take place and with them, bands between 1800-1750 cm^{-1}(symmetric and asymmetric stretching vibration of both carbonyl groups) can appear.

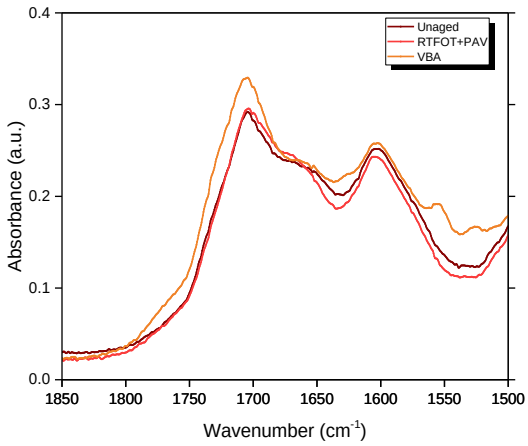

Figure 84: Cutout (1850-1500cm^{-1}) of the resin fractions of binder B504

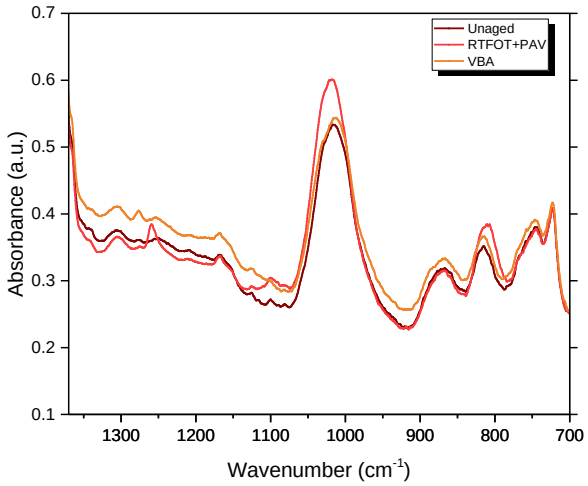

Figure 85: Cutout (1380-700cm^{-1}) of the resin fractions of binder B504

B637

Cutouts of this fraction of binder B637 are given in Figure 86 and Figure 87. Figure 86 depicts the region between 1850 and 1500 cm^{-1} and again the black spectrum of the unaged resins shows the same specific band for carboxylic acids, 2-quinolones and the main aromatic band. The spectra of the common ageing methods RTFOT and PAV are showing decreasing aromatic and carboxylic acid signal intensities in the following order: Unaged>RTFOT>PAV. In the carbonyl region the RTFOT signal shifts slightly to higher wavenumbers and increases in intensity whereas the PAV-aged sample decreases compared to the unaged signal but shifts as well to higher wavenumbers. Possible explanations for that behavior are given in the previous subchapters. The very harsh ageing method of VBA show the same tendencies as the PAV aged fraction for the aromatics and the 2-quinolone bands. The emerging shoulder seen in the PAV sample at 1700 cm^{-1} increases further during the ageing procedure, which can be explained by the emergence of higher amounts of ketones at this ageing state. This profound increase in intensity leads to the overlap of further bands at higher wavenumbers which appear as small shoulders at 1735 cm^{-1} and around 1770 cm^{-1}. The first signal can again be linked to the carbonyl vibration of carboxylic acids, while the second one can be

described as the vibration of an anhydride containing molecule referring to [14]. Furthermore, two signals appear at 1560 cm^{-1} and 1525 cm^{-1} that were not present in the previously mentioned spectra. Those signals might be connected to emerging nitro groups.

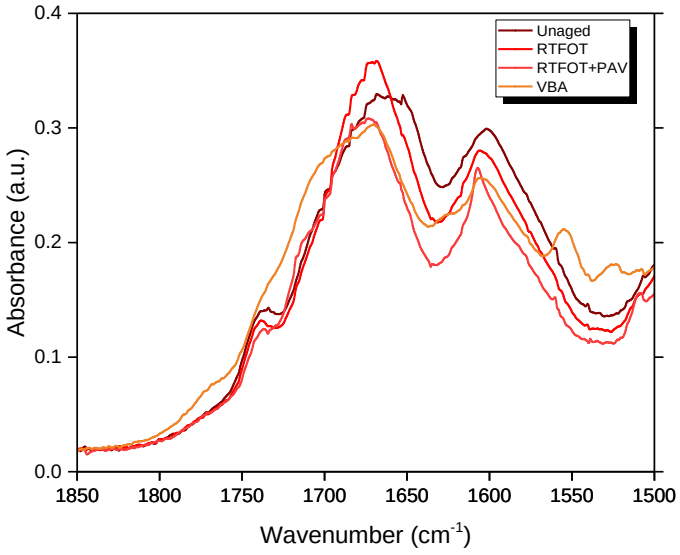

Figure 86: Cutout of the carbonyl and aromatic region of the resin fractions of binder B637

Finally, going deeper down to wavenumber regions between 1350 cm^{-1} and 700 cm^{-1} the next focus are the appearing and changing bands in this region. The band where the most change in intensity happens is the sulfoxide band. This band increases in intensity in the following order: unaged<RTFOT<PAV, but decreases in the next step between PAV and VBA-aged sample. The latter still gave the band with the second highest intensity in this region. As thoroughly discussed in the previous binders the increase in the common ageing methods comes from the oxidation of reactive sulfur containing compounds, mainly from the aromatics but also from the resins fraction itself. Due to the even further oxidized compound in the VBA ageing method, some of the sulfoxide containing molecules are either further oxidized on the sulfur side, which would lead to sulfones, or at any non-sulfur position in the molecule producing a higher overall polarity and a postponed elution.

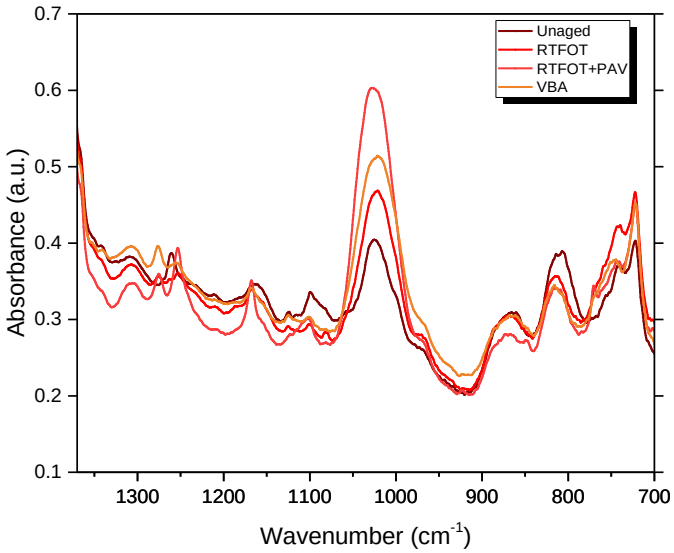

Figure 87: Cutout (1380-700cm^{-1}) of the resins fraction of binder B637

The light-induced ageing experiment of the resins fraction (see Figure 66) shows that ageing in the resins fraction, leads to an increase in intensity in the region between 1750 and 1500 cm^{-1} as well as between 1340 and 700 cm^{-1}, including increasing bands such as the 2-quinolone band (1655 cm^{-1}), the aromatic bands and the sulfoxide band. The general intensity shifts in the whole region below 1800 cm^{-1} can be explained with the emergence of asphaltene-like structures (condensations of smaller molecules, overall polarity increase) during this soft ageing process.

5.3.4. Asphaltenes

The results of the spectral measurements of the asphaltenes are given in Figure 44 (Comparison), Figure 49 (B287), Figure 55 (B504) and Figure 60 (B637). Reproducibility was very hard to achieve for these fractions, due to their solid nature. A small quantity of black powder was obtained, which was difficult to apply completely on the diamond crystal. With that, water vapor and carbon dioxide signals appearing in the spectra, because of the presence of pores filled with air in the samples. All unaged asphaltenes show by far the highest increase in the fingerprint area. The previously defined and discussed bands of alkyl, aromatic, sulfone, sulfoxide and alkene groups are appearing again at their expected values.

B287

Cutouts of important areas of the asphaltenes fraction of binder B287 are shown in Figure 88 and Figure 89. The spectrum of the unaged fraction shows signals of high intensity at 960 cm^{-1}, 1080 cm^{-1} and a triple band between 1250-1170 cm^{-1} which are suggesting high contents of alkenes and polar functionalities (e.g. carboxylic acids, sulfate ester, sulfones). The carbonyl stretching vibration of the carboxylic acids is also observable in this fraction and appears at 1735 cm^{-1}. With ageing this band disappears in the spectra of the aged samples. An additional band at 1700 cm^{-1} might overlap the carboxylic signal in those fractions. This signal corresponds to the emergence of ketone groups and the order of intensity is as follows: unaged<RTFOT<RTFOT+PAV<VBA2<VBA1≈Field. However, the presence of the other bands, that can be linked to carboxylic acids, suggest that these compounds are stable but only present in small amounts. The main aromatic band increases in intensity in the same order as mentioned before. The sulfoxide band at 1030 cm^{-1} show strong increases during the various ageing methods. The intensity of this band is in the PAV aged and VBA aged sample almost

the same whereas the field aged sample has a slightly higher intensity. The changes that are appearing in the wavenumber region between 1350 and 900 cm^{-1} are lower than in the aromatics and resins fraction and no general shift in intensity is observable.

Furthermore, the two bands between 1600 cm^{-1} and 1500 cm^{-1} are appearing again at similar wavenumbers as in the aromatics and resins fractions. The intensities for both bands are higher than in the other fractions and the first signal (at higher wavenumbers) has higher intensity than the second. Similar to the resins fraction, this would suggest a higher share of big, polycyclic molecules compared to few, small aromatic units within the fraction.

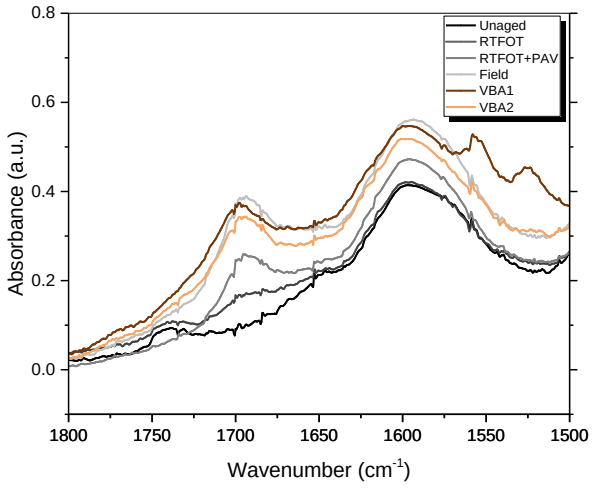

Figure 88: Cutout (1800-1500cm^{-1}) of the asphaltene fractions of binder B287

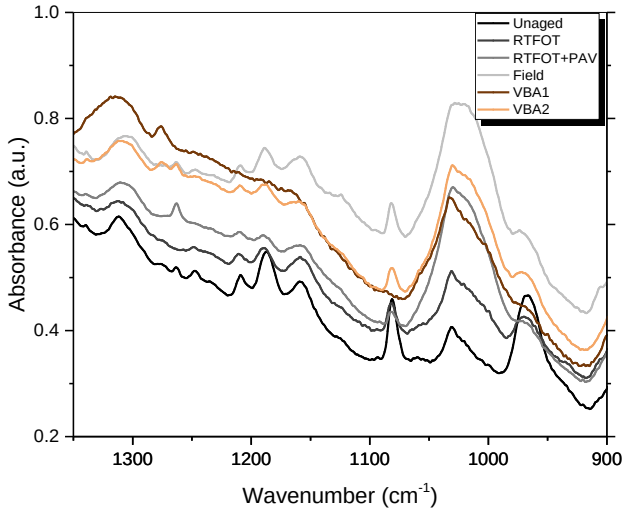

Figure 89: Cutout (1350-900 cm^{-1}) of the asphaltene fractions of binder B287

B504

A cutout of an important area of the asphaltenes fraction of binder B504 is shown in Figure 90. The unaged fraction of this binder shows fewer signals as binder B287. A very small carboxylic acid signal at 1735 cm^{-1}, a shoulder suggesting ketone groups around 1700 cm^{-1} and a sulfoxide band with rather high intensity at 1030 cm^{-1}, which is accompanied by a small signal at 1000 cm^{-1}. Further bands in the

spectra of this fraction are an intense signal at 1310 cm^{-1}, corresponding to sulfones and a broad shoulder ranging from 1290 to 1090 cm^{-1}. During the ageing process, a ketone band emerges with maximum at 1700 cm^{-1}. Also the sulfoxide band increases in both ageing methods. Despite the fact, that the main aromatic band at 1600 cm^{-1} just increases slightly during the ageing process, the three aromatic bands below 900 cm^{-1} show opposed tendencies, as they are decreasing with ageing. An explanation for that is that the overall content of aromatic rings is slightly increasing with ageing, but these rings do form bigger systems, of polyaromatic structures. Hence, the C=C stretch vibration, which is responsible for the signal at 1600 cm^{-1}, does not change at all with the size of the molecules. But the intensity of different bending vibrations from molecules and atoms (mostly hydrogen) attached to aromatic rings is strongly dependent on the size of these rings as overall lower bending vibrations appear. Furthermore, the VBA aged fraction shows two signals at 1560 and 1525 cm^{-1}, which can be linked to nitro groups. Between 1320 and 1100 cm^{-1} the general intensity in the VBA spectra has increased, where bands at 1310 cm^{-1} (Sulfones), 1290 cm^{-1} and 1100 cm^{-1} are appearing.

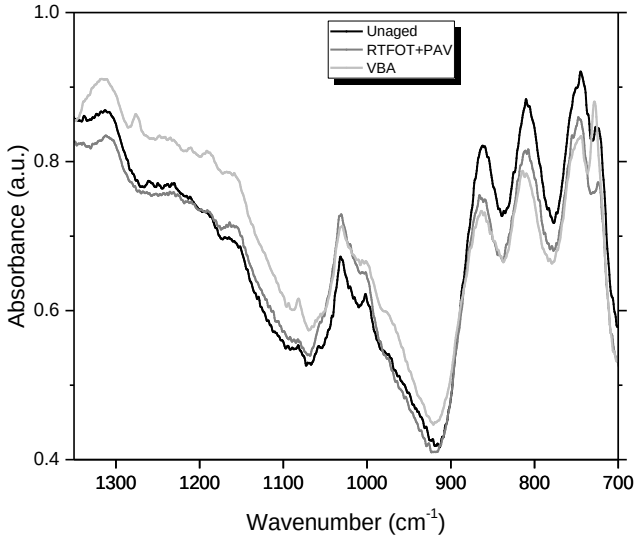

Figure 90: Cutout (1350-700cm^{-1}) of the asphaltene fractions of binder B504

B637

A cutout magnification of the asphaltenes spectra of binder B637 is shown in Figure 91 In the unaged fraction of this sample the same band as previously discussed in binder B287 are observable. The common laboratory ageing methods lead once again to an increase of ketones (1700 cm^{-1}) and sulfoxides (1030 cm^{-1}) in the binder, whereas the general intensity between 1650 and 1220 cm^{-1} for all of the commonly aged samples are very similar. Below this region there are differences in intensity around 1200 cm^{-+} and 1100 cm^{-1}, where the bands are slightly increasing. The aromatic bands below 900 cm^{-1} are decreasing again because of the same reasons discussed for binder B504. The VBA aged asphaltene spectra shows a much higher intensity over the whole spectral region between 1800 and 700 cm^{-1}. Furthermore, two new bands at 1560 and 1525 cm^{-1} emerge that can be linked to attached nitro groups in this fraction. A possible reason for the higher intensity of the aromatic signals below 900 $^{-1}$ might be the much higher oxidation susceptibility in this binder, where not just condensation reactions of aromatic compounds appear, but also greater amounts of small aromatic compounds emerge during the ageing process. This is observable in the spectra, as the main aromatic band increases more rapidly than in the previously discussed binders. Besides that,

the triple band at around 1220 cm^{-1} is not resolved anymore and the alkene band at 960 cm^{-1} only appears as a shoulder of the sulfoxide signal in the VBA aged sample.

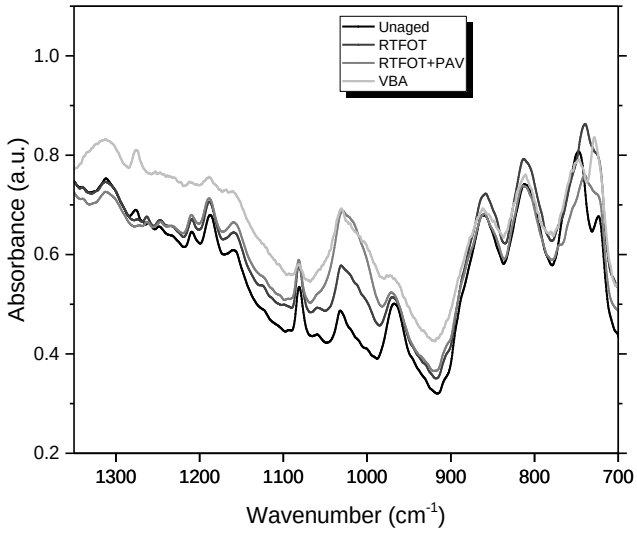

Figure 91: Cutout (1350-700cm^{-1}) of the asphaltenes fraction of binder B637

5.4. Comparison of the FTIR Spectrometer

The used spectrometers, Perkin-Elmer Spectrum Two and Bruker Vertex v80, are going to be compared in this part of the discussion section. The presented results in chapter 4.3.4 show that the ratio of intensities below 1800 cm^{-1} in relation to the intensity at 2921 cm^{-1} differs strongly from one to the other spectrometer (see Figure 62). But especially the bands at 2921 cm^{-1} and 1456 cm^{-1} are related to each other as they are two different vibrations modes of the same molecular class (hydrocarbons). Due to this relationship, the intensity ratio should be constant. Possible reasons for the lower intensity ratio of the bands obtained with the Bruker device may arise from lower detector sensitivity in the wavenumber region below 1800 cm^{-1} or due to a bigger difference in sensitivity of both regions. Another possibility is that the intensities of both bands are depending on the penetration depth. That if other functionalities (e.g. alcohols, …) are contributing to the band at 1456 cm^{-1} and are predominantly concentrated on surface-near regions, the spectrometer with the higher vertical penetration depth (which is a function of the chosen angle of incidence; see chapter 2.4.2.2) would have a lower intensity for this particular band.

A second point that is going to be addressed here is the practicability of both devices, especially in bitumen-related tasks. Noteworthy benefits of the Perkin Elmer device are:

- No cooling of the detector is required
- Compactness of the device
- Incorporated pistil for sample fixation
- High accuracy with few scans

The cooling factor and especially the compactness of the device lead to substantial time-savings for each measurement and with that to an increase in possible measurements per day. The incorporated pistil is very useful due to the monitoring of the applied force on the samples. With that, the pressure can be uniformly adjusted, which results in better reproducibility. Compared to this device the advantages of the Bruker device are as follows:

- More scans per time period
- Evacuated beam-path of the interferometer
- Nitrogen atmosphere in the sample chamber

With increasing number of scans n the signal to noise ratio increases by the square root of n. Also, the vacuum atmosphere has great influence on the resulting spectrum as interfering signals from $H_2O(g)$ and $CO_2(g)$ can be excluded. Finally, the nitrogen atmosphere of the sample chamber minimizes the possibility of oxidation reactions during the measurements and enhances the evaporation process of remains of solvent in the sample.

Overall, the advantages of the Bruker device should lead to better spectra regarding resolution and exclusion of interfering peaks. Furthermore, the measurements of samples with remaining solvents are accelerated, due to the nitrogen purge of the sample. However, for the application on bitumen-related tasks the resolution of the Perkin-Elmer device is more than enough. With that said, the advantages regarding practicability and time-saving were far more important in this thesis to obtain enough results with high quality. Even the low scan number and nonexistent vacuum in the Perkin-Elmer device has not had great impact on the results. To analyze the first parameter the scan numbers were stepwise enhanced (4->8->16 scans) and the resulting spectra were compared. No changes in the spectra appeared but an enormous increase in time was the consequence. The other drawback of the Perkin-Elmer device (as mentioned in chapter 3.4.1) is also minimized due to the capability of the instrument to reduce interfering signals mathematically.

6. Conclusion and Recommendations for Further Study and Practice

Profound insights on sample behaviour has been found, which should optimize the handling and preparation of bitumen samples especially before FTIR measurements. Even one day of storage in the light enhance the bands that are correlated to ageing in the FTIR spectrum. With that said insufficient preparation of bitumen samples before FTIR measurements can lead to results of seemingly over-oxidized bitumen, although just the upper layer of the sample is oxidized. This information was received by comparing the FTIR results to the DSR results, where the DSR measurements showed that the ageing rate is much slower than observed with FTIR. Therefore, sufficient preparation methods are needed to minimize such faults. These methods include heating in nitrogen atmosphere and thorough homogenization before every FTIR measurement. A further aspect that seemingly changes the spectrum is the choice of spectrometer. Different spectrometers give different ageing values. With that a proper integration and normalization method still needs research to eventually get ageing values fully independent of the FTIR device. The conclusions of the time-dependent studies and the spectrometer comparison are summarized in the following points:

- Storing and handling have great influence on the bitumen samples
- Especially light contamination can lead to oxidation
- Even the spectra of long-term aged samples change when samples are stored in light
- According to the FTIR-DSR test runs mainly the upper layer of the material changes
- Proper homogenization and uniform sample preparation before FTIR measurements is required to obtain sufficient reproducibility
- The obtained ageing values are not independent from the geometry of the ATR cell and the FTIR spectrometer

The combination of Fast SARA and FTIR turned out to be a very practicable tool, where a broad amount of valuable information could be obtained within a time frame of just two days. Determinations of the ageing behaviour of the fractions, predominant oxidation products as well as polarity shifts and possible consequences of such changes are obtainable. Furthermore, a first application of chemical analysis of VBA aged samples was implemented. The following points provide a summary of the findings obtained from the combination of Fast SARA and FTIR spectroscopy:

- Saturates amount decreases in the VBA ageing and Field ageing procedures
- Predominantly aromatic structures in the saturates get oxidized
- Aromatics are the most reactive fraction
- The sulfoxide formation in aromatics lead to polarity shifts of those molecules
- 2-Quinolone dimerization plays a key role during the ageing process
- Multiphase reactions of NO_x and O_3 with aromatic structures occur during the VBA ageing process
- Characteristic NO_2-bands in the FTIR spectra might correlate to present molecular classes
- The asphaltene content increases throughout all applied ageing procedures
- This increase influences the general absorbance in the spectral region below 1800 cm^{-1}

In the end, a recommendation for further study would be to age the fractions separately and measure the FTIR spectra of those oxidized fractions afterwards. This would complement the investigations implemented in this work and provide a new perspective on bitumen ageing. Furthermore, the investigation of more field aged samples might be useful to adjust the VBA ageing procedure (especially the ozone concentration, temperature and duration) even better to the simulation of real ageing behaviour. And finally, the presence of functional groups such as e.g. sulfones, sulphate esters and 2-quinolones should be determined more accurately. Possible

procedures might include selective separations of the fractions (eventually by using more advanced techniques such as multidimensional LC-techniques) coupled with mass spectrometry. Those techniques would complement the spectroscopic approach by expanding and confirming band assignments and eventually lead to a broader understanding of functionalities within the bitumen fractions.

7. List ofTables

8. List of Figures

References

[1] N. Sakib and A. Bhasin, "Measuring polarity-based distributions (SARA) of bitumen using simplified chromatographic techniques," *International Journal of Pavement Engineering,* vol. 20, no. 12, pp. 1-14, 9 February 2018.

[2] KINETIC ENERGY, "kineticpetro," KINETIC ENERGY, 30 Dezember 2018. [Online]. Available: https://www.kineticpetro.com/crude-oil-separation-processes/. [Accessed 17 März 2020].

[3] U. Musanke, R. Rühl, D. Höber and R. Mansfeld, "Einsatz von Bitumen im Straßenbau," *Gefahrstoffe - Reinhaltung der Luft,* pp. 285-287, July/August 2010.

[4] T. McDonald, "For Construction Pros," AC Business Media, 20 November 2019. [Online]. Available: https://www.forconstructionpros.com/asphalt/article/10297263/why-tracking-temperatures-is-key-to-successful-asphalt-paving. [Accessed 17 July 2020].

[5] B. A. Williams, A. Copeland and T. C. Ross, "Asphalt Pavement Industry Survey on Recycled Materials and Warm-Mix Asphalt," 2018.

[6] D. Lesueur, "The colloidal structure of bitumen: consequences on the rheology and on the mechanisms of bitumen modification," *Advances in Colloid and Interface Science,* vol. 145, no. 1-2, pp. 42-82, 30 Januar 2009.

[7] Y. Yildirim, "Polymer modified asphalt binders," *Construction and Building Materials,* vol. 21, no. 1, pp. 66-72, January 2007.

[8] European Asphalt Pavement Association, "Asphalt the 100% recyclable construction product," Brussels, Belgium, 2014.

[9] costapaving, "COSTAPAVING.COM," 10 Oktober 2019. [Online]. Available: https://costapaving.com/how-to-protect-asphalt-pavement/. [Accessed 17 März 2020].

[10] CEN, *Bitumen and bituminous binders - Determination of the resistance to hardening under the influence of heat and air - Part 1: RTFOT method,* Brussels, 2007.

[11] CEN, *Bitumen and bituminous binders - Accelerated long-term ageing conditioning by a Pressure Ageing Vessel (PAV),* Brussels, 2012.

[12] J. Mirwald, D. Maschauer, B. Hofko and H. Grothe, "Impact of Reactive Oxygen Species on Bitumen Ageing - The Viennese Binder Ageing Method," *Construction and Building Materials,* vol. 257, 10 October 2020.

[13] J. C. Petersen, "Chemical Composition of Asphalt as Related to Asphalt Durability: State of the Art," *Transportation Research Record,* pp. 13-30, 1984.

[14] J. C. Petersen, "A Review of the Fundamentals of Asphalt Oxidation," *Transportation Research Cricular E-C140,* October 2009.

[15] S. Slomkowski, J. V. Aleman, R. G. Gilbert, M. Hess, K. Horie, R. G. Jones, P. Kubisa, I. Meisel, W. Mormann, S. Penczek and R. F. T. Stepto, "Terminology of polymers and polymerization processes in dispersed systems(IUPAC Recommendations 2011)," *Pure and Applied Chemistry,* vol. 83, no. 12, p. 2229–2259, 10 September 2011.

[16] F. Handle, J. Füssl, S. Neudl, D. Grossegger, L. Eberhardsteiner, B. Hofko, M. Hospodka, R. Blab and H. Grothe, "The bitumen microstructure: a fluorescent approach," *Materials and Structures,* vol. 49, p. 167–180, 07 December 2014.

[17] L. Champion-Lapalu, A. Wilson, G. Fuchs, D. Martin and J. Planche, "Cryo-scanning electron microscopy: a new tool for interpretation of fracture studies in bitumen/polymer blends," *Energy Fuels,* p. 143–147, 2002.

[18] L. Loeber, O. Sutton, J. Morel, J.-M. Valleton and G. Muller, "New direct observations of asphalts and asphalt binders by scanning electron microscopy and atomic force microscopy," *Journal of Microscopy,* vol. 182, no. 1, pp. 32-39, April 1996.

[19] L. W. Corbett, "Composition of asphalt based on generic fractionation, using solvent deasphaltening, elution-adsorption chromatography, and densimetric characterization," *Analytical Chemistry,* vol. 41, no. 4, pp. 576-579, 1 April 1969.

[20] ASTM, "ASTM D4124-01: Standard Test Methods for Separation of Asphalt into Four Fractions," ASTM International, Philadelphia, 2001.

[21] J. C. Petersen, "A Dual Sequential Mechanism for the Oxidation of Asphalts," *Petroleum Science and Technology,* vol. 16, no. 9-10, p. 1023–1059, 1998.

[22] J. Knotnerus, "Bitumen Durability: Measurement by Oxygen Absorption," *Industrial and Engineering Chemistry Process Design and Development,* vol. 11, p. 411–422, 1 December 1972.

[23] R. Atkinson, "Atmospheric chemistry of VOCs and NOx," *Atmospheric Environment,* vol. 34, no. 12-14, pp. 2063-2101, 2000.

[24] M. Beychok, "NOX emission from fuel combustion controlled," *Oil & Gas Journal,* pp. 53-56, March 1973.

[25] E. Fitzer and D. Siegel, "Stickoxid-Emissionen industrieller Feuerungsanlagen in Abhängigkeit von den Betriebsbedingungen," *Chemie Ingenieur Technik,* vol. 47(13), 1975.

[26] L. T. Murray, "Lightning NOx and Impacts on Air Quality," *Current Pollution Reports,* vol. 2, pp. 115-133, 25 April 2016.

[27] W. Spangl and C. Nagl, "JAHRESBERICHT DER LUFTGÜTEMESSUNGEN IN ÖSTERREICH 2018," Wien, 2019.

[28] I. S. A. Isaksen and S. B. Dalsøren, "Getting a Better Estimate of an Atmospheric Radical," *Science,* vol. 331, no. 6013, pp. 38-39, 07 January 2011.

[29] B. Hofko, M. Hospodka, R. Blab, L. Eberhardsteiner, J. Füssl, H. Grothe and F. Handle, "Impact of field ageing on low-temperature performance of binder and hot mix asphalt.," *Asphalt Pavements,* vol. 1 and 2, pp. 381-395, 2014.

[30] C. T. Bowman, "Investigation of Nitric Oxide Formation Kinetics in Combustion Processes: The Hydrogen-Oxygen-Nitrogen Reaction," *Combustion Science and Technology,* vol. 3(1), pp. 37-45, 1971.

[31] K. Robards, P. R. Haddad and J. P. E., Principles and practice of modern chromatographic methods, London: Academic Press, 1994.

[32] F. Salvato, A. De Lima Leite and M. Costa da Cruz Gallo de Carvalho, "Strategies for Protein Separation," in *Integrative Proteomics*, 1 ed., Intech, 2012, p. 13.

[33] P. Larkin, Infrared and Raman Spectroscopy. Principles and Spectral Interpretation, 225 Wyman Street, Waltham, MA 02451, USA: Elsevier, 2011.

[34] B. Schrader, Infrared and Raman Spectroscopy: Methods and Applications, Wiley-VCH Verlag, 1995.

[35] Somoza, "Wikimedia Commons," 26 March 2006. [Online]. Available: https://commons.wikimedia.org/wiki/File:Morse-potential.png. [Accessed 22 July 2020].

[36] M. Mutsaers, *Zika vector control: Near infrared spectroscopy predicting Wolbachia infection in post-mortem Aedes aegypti,* 2018.

[37] P. Griffith and J. A. Haseth, Fourier Transform Infrared Spectrometry, 2 ed., John Wiley & Sons, 2006.

[38] K. Kauppinen and M. Hollberg, "Infrared Spectrometers," *Encyclopedia of Applied Physics,* vol. 19, pp. 265-287, 1997.

[39] PerkinElmer, Inc., "Dynascan Interferometer".

[40] Bruker Corporation, "Bruker Corporation," 2018. [Online]. Available: https://www.bruker.com/fileadmin/user_upload/8-PDF-Docs/OpticalSpectrospcopy/FT-IR/VERTEX/Brochures/VERTEXseries_Brochure_EN.pdf. [Accessed 22 July 2020].

[41] AASHTO, *AASHTO T 315-12, Standard Method of Test for Determining the Rheological Properties of Asphalt Binder Using a Dynamic Shear Rheometer (DSR),* Washington, D.C.: American Association of State Highway and Transportation Officials, 2016.

[42] E. Yener and S. Hınıslıoğlu, "Effects of exposure time and temperature in aging test on asphalt binder properties," *International Journal for Computational Civil and Structural Engineering,* vol. 5, no. 2, pp. 112-124, November 2014.

[43] J. C. Petersen, R. V. Barbour, S. M. Dorrence, F. A. Barbour and R. V. Helm, "Molecular interactions of asphalt. Tentative identification of 2-quinolones in asphalt and their interaction with carboxylic acids present," *Analytical Chemistry,* vol. 43, no. 11, pp. 1491-1496, 1 September 1971.

[44] S. Weigel and D. Stephan, "Differentiation of bitumen according to the refinery and ageing state based on FTIR spectroscopy and multivariate analysis methods," *Materials and Structures,* vol.

51, no. 130, 25 September 2018.

[45] J. Lamontagne, P. Dumas, V. Mouillet and J. Kister, "Comparison by Fourier transform infrared (FTIR) spectroscopy of different ageing techniques: application to road bitumens," *Fuel,* vol. 80(4), pp. 483-488, March 2001.

[46] M. R. Nivitha, E. Prasad and J. M. Krishnan, "Transitions in unmodified and modified bitumen using FTIR spectroscopy," *Materials and Structures,* vol. 52(7), 9 January 2019.

[47] F. Handle, M. Harir, J. Füssl, A. N. Koyun, D. Grossegger, N. Hertkorn, L. Eberhardsteiner, B. Hofko, M. Hospodka, R. Blab, P. Schmitt-Kopplin and H. Grothe, "Tracking Aging of Bitumen and Its Saturate, Aromatic, Resin, and Asphaltene Fractions Using High-Field Fourier Transform Ion Cyclotron Resonance Mass Spectrometry," *Energy&Fuels,* vol. 31(5), pp. 4771-4779, 2017.

[48] R. Atkinson and J. Arey, "Atmospheric Chemistry of Gas-phase Polycyclic Aromatic Hydrocarbons: Formation of Atmospheric Mutagens," *Environmental Health Perspectives,* vol. 102 (4), pp. 117-124, 1994.

[49] M. Nayebzadeh and M. Vahedpour, "A review on reactions of polycyclic aromatic hydrocarbons with the most abundant atmospheric chemical fragments: theoretical and experimental data," *Progress in Reaction Kinetics and Mechanism,* vol. 42 (3), pp. 201-220, 1 September 2017.

Attachments

- **Gravimetry**

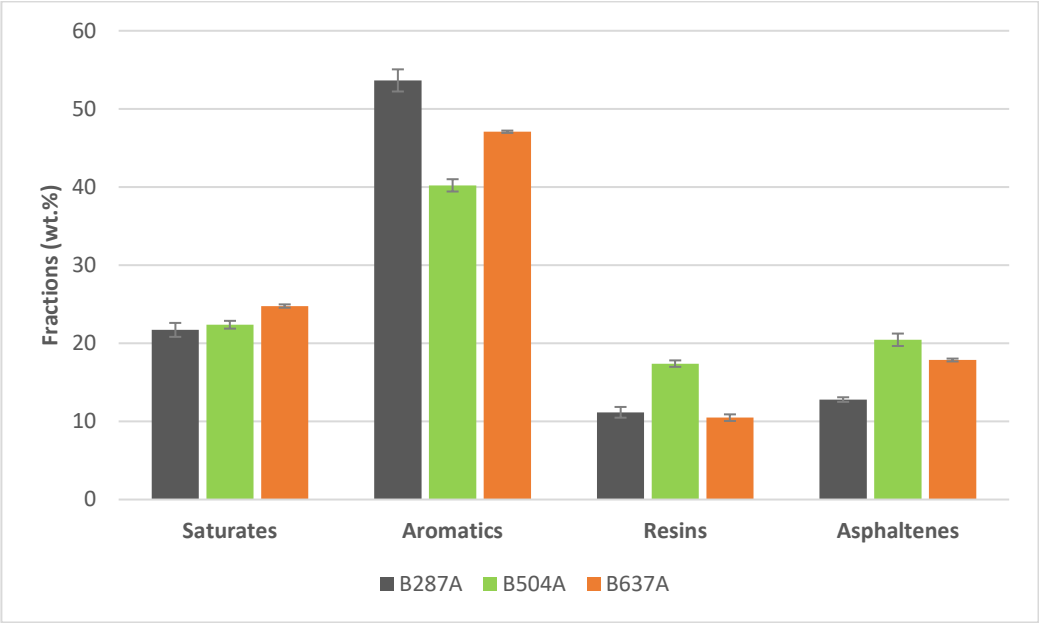

Figure 92: Polarity fractions of all three binders with added standard deviations

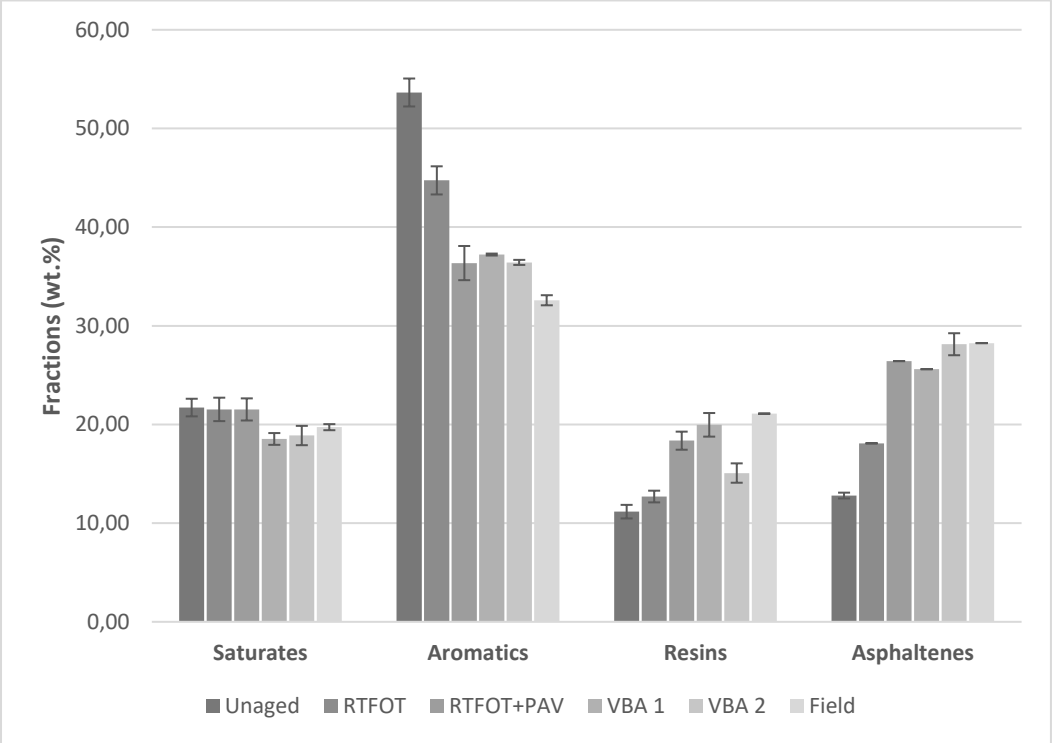

Figure 93: Comparison of field aged to VBA 2 aged binder B287 with added standard deviations

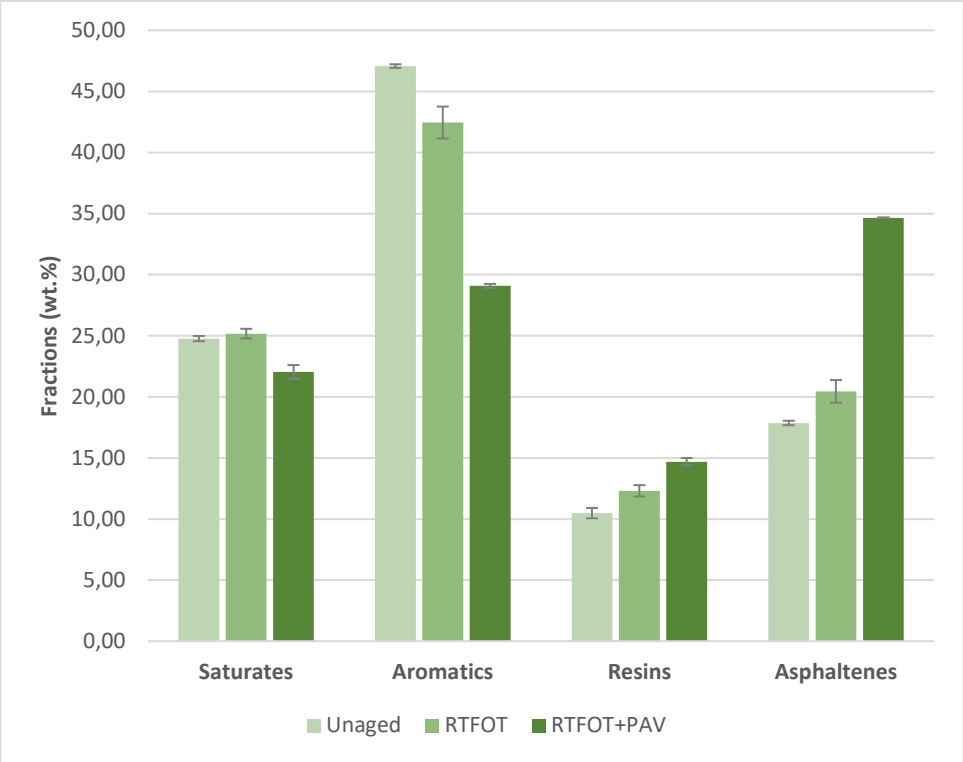

Figure 94: Mass percentages of all fractions of binder B504 with added standard deviations

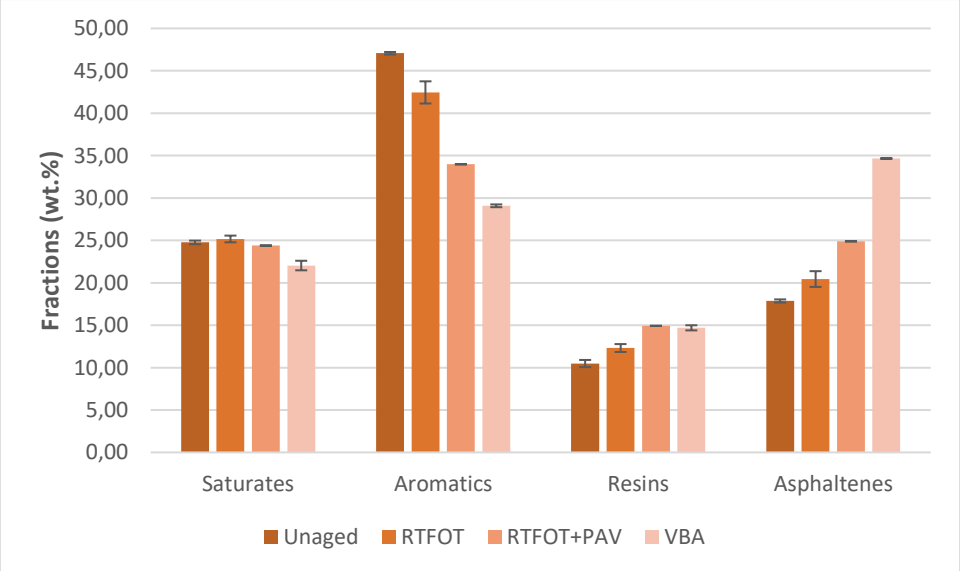

Figure 95: Mass percentages of all fractions of binder B637 with added standard deviations

- **FTIR spectroscopy**

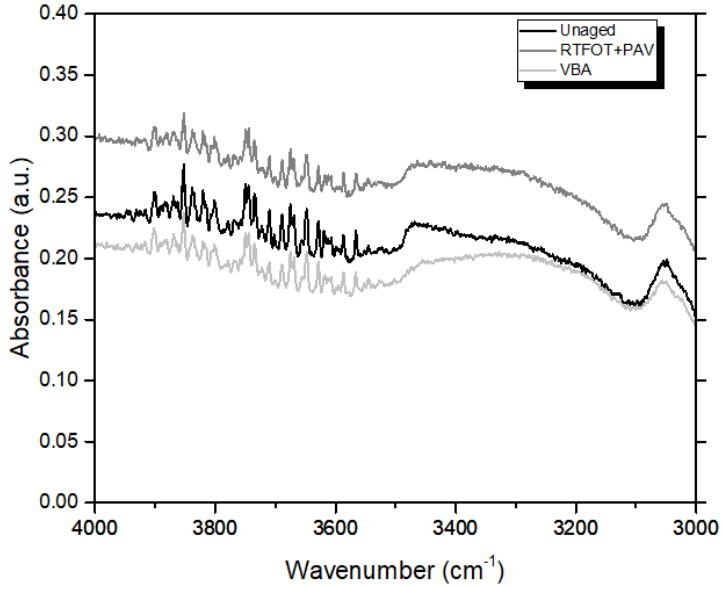

Figure 96: Cutout (4000-3000cm^{-1}) of the asphaltenes fraction of binder B504

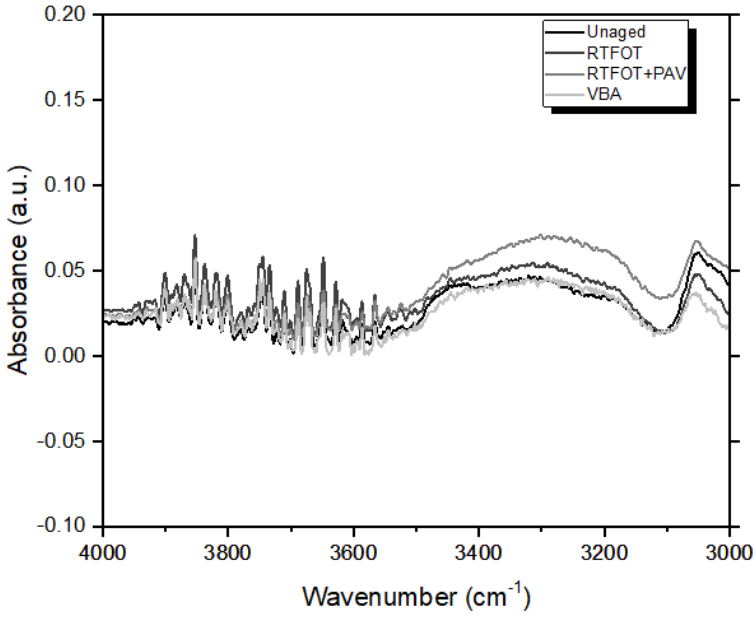

Figure 97: Cutout (4000-3000cm^{-1}) of the asphaltenes fraction of binder B637